Multiferroic bismuth ferrates: Synthesis, structure-property relationships and phase transformations

Dissertation

Zur Erlangung des Doktorgrades der Naturwissenschaften

- Dr. rer. nat. -

Fachbereich 02 (Biologie/Chemie)

Der Universität Bremen

Vorgelegt von

M. Sc. Andrea Kirsch

Bremen 2018

Diese Arbeit wurde in der Arbeitsgruppe „Chemische Kristallographie fester Stoffe“ von Herrn Prof. Dr. Thorsten M. Gesing an der Universität Bremen im Zeitraum von Oktober 2014 bis August 2018 angefertigt.

Begutachtung des schriftlichen Teils: Abgabe 10.08.2018

1. **Gutachter:** Prof. Dr. Reinhard X. Fischer, Fachbereich 05 Geowissenschaften, Kristallographie, Universität Bremen
2. **Gutachter:** Prof. Dr. Götz Eckold, Physikalische Chemie fester Körper, Georg-August-Universität Göttingen
3. **Gutachter:** Dr. Isaac Abrahams, School of Biological and Chemical Sciences, Queen Mary University of London

Tag der mündlichen Prüfung: 28.09.2018

Mitglieder des Prüfungsausschusses:

1. Prof. Dr. Jens Beckmann, Fachbereich 02 Biologie/Chemie, Institut für Anorganische Chemie und Kristallographie, Metallorganische Chemie der Hauptgruppenelemente, Universität Bremen
2. Prof. Dr. Anne Staubitz, Fachbereich 02 Biologie/Chemie, Institut für Organische und Analytische Chemie, Organische Funktionsmaterialien, Universität Bremen
3. Prof. Dr. Reinhard X. Fischer, Fachbereich 05 Geowissenschaften, Kristallographie, Universität Bremen
4. Prof. Dr. Lutz Mädler, Fachbereich 04 Produktionstechnik –Maschinenbau & Verfahrenstechnik-, Mechanische Verfahrenstechnik, Leitung Verfahrenstechnik am Leibniz-Institut für Werkstofforientierte Technologien IWT Bremen, Universität Bremen
5. Dr. Michael Maas, Fachbereich 04 Produktionstechnik –Maschinenbau & Verfahrenstechnik-, Advanced Ceramics, Universität Bremen
6. Marius Wolpmann, Fachbereich 02 Biologie/Chemie, Institut für Anorganische Chemie und Kristallographie, Student im Masterstudiengang Chemie, Universität Bremen

Acknowledgments

First of all, I would like to thank Prof. Dr. Thorsten Gesing who gave me the possibility to conduct my PhD studies in his group “Solid State Chemical Crystallography”. Many thanks also go to PD Dr. M. Mangir Murshed. Both of them continuously supported my PhD studies and I appreciate all their guidance, contributions of time, encouragements and insightful comments. Besides my supervisors, I would like to thank Prof. Dr. Anne Staubitz for her support, good advices and encouragements. Furthermore, I thank all committee members for donating their time to review my dissertation, especially Prof. Dr. Reinhard X. Fischer who already supported me during my master studies.

For all the collaborational works I thank Dr. Ashfia Huq and Dr. Melanie J. Kirkham (POWGEN, SNS Oak Ridge, USA), Prof. Dr. Klaus-Dieter Becker and Prof. Dr. F. Jochen Litterst (Institut für Physikalische und Theoretische Chemie, TU Braunschweig), Dr. Marco Schowalter and Prof. Dr. Rosenauer (Institute of Solid State Physics, University Bremen) and Prof. Dr. Cecilia B. Mendive and Dr. Mariano Curti (Instituto de Investigaciones Fisicas de Mar del Plata, Universidad Nacional de Mar del Plata, Argentina).

I also want to thank all my colleagues at the “Solid State Chemical Crystallography” group for a lot of help and fun during my PhD experience. Many thanks also go to the former trainees Rebecca Siemering, Jasmin Richter and Jannis Diekmann who supported me a lot with their responsible works in the laboratory.

For financial support I thank the MAPEX Center for Materials and Processes and the Central Research Development Fund of the University of Bremen that allowed me to participate in the HERCULES – Summer school in Grenoble, the DESY for a scholarship for the RACIRI Summer School, the DAAD and the University of Bremen.

Last but not least, words cannot express how grateful I am to my family, in particular to my parents, who made my academic studies possible not only with great financial but also with greatest emotional support. Special thanks also go to my dear friends, who are always a motivation for me and who bring so much joy into my life. Thank you.

Declaration

Versicherung an Eides Statt

Hiermit versichere ich, Andrea Kirsch
Wilhelm-Röntgenstr. 10, 28357 Bremen
Matr.Nr.: 2707592

an Eides statt durch meine Unterschrift, dass ich die vorstehende Arbeit mit dem Titel „*Multiferroic bismuth ferrates: Synthesis, structure-property relationships and phase transformations*“ selbständig und ohne fremde Hilfe angefertigt und alle Stellen, die ich wörtlich dem Sinne nach aus Veröffentlichungen entnommen habe, als solche kenntlich gemacht habe, mich auch keiner anderen als der angegebenen Literatur oder sonstiger Hilfsmittel bedient habe.

Ich versichere an Eides statt, dass ich die vorgenannten Angaben nach bestem Wissen und Gewissen gemacht habe und dass die Angaben der Wahrheit entsprechen und ich nichts verschwiegen habe.

Die Strafbarkeit einer falschen eidesstattlichen Versicherung ist mir bekannt, namentlich die Strafandrohung gemäß § 156 StGB bis zu drei Jahren Freiheitsstrafe oder Geldstrafe bei vorsätzlicher Begehung der Tat bzw. gemäß § 161 Abs. 1 StGB bis zu einem Jahr Freiheitsstrafe oder Geldstrafe bei fahrlässiger Begehung.

_____ _____

(Andrea Kirsch)

Bremen, 2018

Table of contents

Publications

Kirsch, A., Murshed, M. M., Gesing, Th. M.; Facile sol-gel synthesis of $Bi_2Fe_4O_9$ and nanocomposites of the (1-x) $BiFeO_3$ · (x) $Bi_2Fe_4O_9$ system, *manuscript in preparation.*

Curti, M., Mendive, C.B., Kirsch, A., Granone, L. I., Arana, A., López Robledo, G., Murshed, M. M., Gesing, Th. M., Gesing; Solvent effect in the visible-light photocatalytic degradation of phenol with mullite-type $Bi_2Fe_4O_9$, *manuscript in preparation.*

Kirsch, A., Murshed, M. M., Litterst, F. J., Gesing, Th. M.; Structural, spectroscopic and thermoanalytic studies on Bi2Fe4O9: tunable properties driven by nano- and poly-crystalline states *J Phys Chem C* **2018***, submitted for publication.*

Kirsch, A., Murshed, M. M., Kirkham, M. J., Huq, A., Litterst, F. J., Gesing, Th. M.; Temperature-dependent structural and spectroscopic studies of $(Bi_{1-x}Fe_x)FeO_3$ *J Phys Chem C* **2018**, *submitted for publication.*

Curti, M., Kirsch, A., Granone, L. I., Tarasi, F., López Robledo, G., Bahnemann, D.W., Murshed, M. M., Gesing, Th. M., Mendive C.B.; Visible-light photocatalysis with mullite-type $Bi_2(Al_{1-x}Fe_x)_4O_9$: Striking the balance between bandgap narrowing and conduction band lowering *ACS Catal.* **2018***, 8*, 8844−8855.

Kirsch, A., Murshed, M. M., Schowalter, M., Rosenauer, A., Gesing, Th. M.; Nanoparticle Precursor into Polycrystalline $Bi_2Fe_4O_9$: An Evolutionary Investigation of Structural, Morphological, Optical, and Vibrational Properties *J Phys Chem C* **2016**, *120* 18831−18840.

Kirsch, A., Murshed, M. M., Gaczynski, P., Becker, K.-D., Gesing, Th. M.; $Bi_2Fe_4O_9$: Structural changes from nano- to micro-crystalline state *Z. Naturforsch*. **2016**; *71(5)b* 447–455.

List of abbreviations

ADP	Atomic displacement parameter
APS	Advanced Photon Source
ASF	Absorption spectrum fitting method
DASF	Derivative absorption spectrum fitting method
DEA	Debye-Einstein-Anharmonicity approach
DEG	Diethylene glycol
DSC	Differential scanning calorimetry
EDX	Energy dispersive X-ray spectroscopy
EG	Ethylene glycol
FC	Field-cooled
FTIR	Fourier transform infrared
HRTEM	High-resolution transmission electron microscopy
IS	Isomer shift
LEP	Lone electron pair
NPD	Neutron powder diffraction
ORNL	Oak Ridge National Laboratory
PVA	Polyvinyl alcohol
QS	Quadrupole splitting
SEM	Scanning electron microscopy
SNS	Spallation Neutron Source
SQUID	Superconducting quantum interference device
TEG	Tetraethylene glycol
TEM	Transmission electron microscopy
TREG	Triethylene glycol
XRD	X-ray diffraction
XRPD	X-ray powder diffraction
WLE	Wang-Liebau eccentricity

Zusammenfassung

Heutzutage werden große Anstrengungen unternommen die vielfältige Physik von Materialien mit interessanten magnetischen, elektronischen, optischen und photokatalytischen oder sogar multiferroischen Eigenschaften zu verstehen. Das Hauptziel ist es, die Leistung der Materialien für bestimmte Anwendungen zu verbessern oder sogar neue Mechanismen für Zukunftstechnologien, wie Wasserspaltung, Spintronik, Sensorik sowie Energiespeicherung und –umwandlung, zu finden. Im Rahmen dieser Dissertation wurden zwei dieser potentiell sehr vielversprechenden Verbindungen, die im Perowskit-Typ kristallisierenden Phasen $(Bi_{1-x}Fe_x)FeO_3$ und der Mullit-Typ $Bi_2Fe_4O_9$, synthetisiert und untersucht. Zunächst sollten die Synthesebedingungen verstanden werden, welche die resultierende Phasenzusammensetzung, entstehenden Strukturen und deren Eigenschaften maßgeblich beeinflussen. Das zweite Ziel war es, die Struktur-Eigenschafts-Beziehungen basierend auf der mittleren Kristallitgröße, chemischen Zusammensetzung und Phasenzusammensetzung der Materialen zu untersuchen. Es wird gezeigt, dass das Phasensystem Bi_2O_3 – Fe_2O_3 sehr komplex und sensitiv gegenüber vielen Syntheseparametern wie z.B. dem Typ des Komplexbildners, dem pH-Wert sowie der Kalzinierungszeit und -temperatur ist. Des Weiteren wurde beobachtet, dass $BiFeO_3$ und $Bi_2Fe_4O_9$ von ~680 K bis ~920 K immer nebeneinander kristallisieren, weshalb in diesem Temperaturbereich eine geringe Energiedifferenz in der Stabilität dieser Phasen erwartet wird. Das Verhältnis von $BiFeO_3$: $Bi_2Fe_4O_9$ kann z.B. durch Einstellen des pH-Werts der Syntheselösung stark modifiziert werden. Darüber hinaus wurde während der Transformation eines röntgenamorphen Pulvers in polykristallines $Bi_2Fe_4O_9$ (Kapitel 3)[1] eine Zwischenphase $(Bi_{1-x}Fe_x)FeO_3$ gefunden. Bei Erhöhung der Temperatur wandelte sich diese graduell in die stöchiometrische $BiFeO_3$-Phase um. Infolgedessen konnte der Anteil an Bi^{3+} und Fe^{3+} auf der A-Lage der Perowskit-Struktur (ABO_3) durch Anpassung der Kristallisationszeit bei einer bestimmten Temperatur variiert und zwei Proben mit x_{Fe} = 0.15 und 0.25 hergestellt werden (Kapitel 4).[2] Beide Strukturen, $(Bi_{0.75}Fe_{0.25})FeO_3$ und $(Bi_{0.85}Fe_{0.15})FeO_3$, zeigten interessantes super-paramagnetisches Verhalten und signifikant veränderte kristallchemisch-physikalische Eigenschaften in Bezug auf Polyederverzerrung, thermische Expansion, Debye-Temperatur, Schwingungseigenschaften und magnetisches Verhalten im Vergleich zu stöchiometrischem $BiFeO_3$. Eine weitere Studie wurde der

Entwicklung der strukturellen, morphologischen und optischen Eigenschaften sowie den Schwingungseigenschaften von Proben mit variierenden $BiFeO_3$: $Bi_2Fe_4O_9$ Phasenverhältnissen gewidmet (Kapitel 5).[3] Es zeigte sich, dass einige Proben funktionalisierte Oberflächen aufwiesen, die mit 4 – 13 nm großen Partikeln bedeckt waren. Deren Netzebenen ordneten sich während der transmissions-elektronenmikroskopischen Messungen (TEM) bei der Interaktion mit dem Elektronenstrahl um. Außerdem zeigte die Studie, dass die Kombination aus der kürzlich vorgestellten "Derivative Absorption Spectrum Fitting" (DASF) Methode und der seit langem bekannten Tauc Methode ein brauchbares Werkzeug ist, um gleichzeitig die Bandlücke sowie die Natur des optischen Übergangs (direkt und indirekt) von Halbleitern zu bestimmen. Unter Gebrauch dieses Ansatzes wurde die Art des optischen Übergangs, was zuvor ein fortlaufendes Diskussionsthema war, für $Bi_2Fe_4O_9$ als direkt bestimmt. Die Bandlücken der Materialien liegen zwischen 1.80(1) eV und 2.75(3) eV. Darüber hinaus wurden die von der Kristallitgröße abhängigen Struktur-Eigenschafts-Beziehungen von $Bi_2Fe_4O_9$ mittels struktureller und spektroskopischer Methoden (Kapitel 6)[4] untersucht. Rietveld Analysen zeigten unter 122(2) nm eine erhebliche Veränderung der Gitterparameter *a*, *b*, *c* und der Mikroverspannungen als Funktion der mittleren Kristallitgröße. Gleichzeitig konnten große Verzerrungen der FeO_4- und FeO_6-Koordinationen, ein signifikantes Erweichen der Raman Moden und deren Verbreiterung, eine Abnahme der antiferromagnetischen Umwandlungsenthalpie sowie eine veränderte lokale Spinorientierung im Vergleich zum Bulk-Material in diesem Größenbereich festgestellt werden.

(1) Kirsch, A.; Murshed, M. M.; Gaczynski, P.; Becker, K.-D.; Gesing, T. M. $Bi_2Fe_4O_9$: Structural Changes from Nano- to Micro-Crystalline State. *Zeitschrift für Naturforsch. B J. Chem. Sci.* **2016**, *71* (5), 447–455.

(2) Kirsch, A.; Murshed, M. M.; Kirkham, M. J.; Huq, A.; Litterst, F. J.; Gesing, T. M. Temperature-Dependent Structural and Spectroscopic Studies of $(Bi_{1-x}Fe_x)FeO_3$. *J. Phys. Chem. C* **2018***, submitted for publication*.

(3) Kirsch, A.; Murshed, M. M.; Schowalter, M.; Rosenauer, A.; Gesing, T. M. Nanoparticle Precursor into Polycrystalline $Bi_2Fe_4O_9$: An Evolutionary Investigation of Structural, Morphological, Optical, and Vibrational Properties. *J. Phys. Chem. C* **2016**, *120* (33), 18831–18840.

(4) Kirsch, A.; Murshed, M. M.; Litterst, F. J.; Gesing, T. M. Structural, spectroscopic and thermoanalytic studies on $Bi_2Fe_4O_9$: tunable properties driven by nano- and poly-crystalline states *J. Phys. Chem. C* **2018***, submitted for publication.*

Summary

Nowadays, great efforts are made to understand the rich physics of materials that show interesting magnetic, electronic, optic, photocatalytic or even multiferroic properties. The main objective is to finetune the materials performance to certain applications or to even explore new possible mechanisms for future key technologies such as water splitting, spintronics, sensors as well as energy storage and conversion. Within the scope of this dissertation two of such potentially very promising compounds, perovskite-type $(Bi_{1-x}Fe_x)FeO_3$ and mullite-type $Bi_2Fe_4O_9$, were synthesized and studied. The primary focus was placed to understand the synthesis conditions that strongly influence the resulting phase composition, structures and corresponding properties. The second main focus was to study the structure-property relationships based on the average crystallite size, chemical composition and phase composition of the materials.

It could be shown that the phase system Bi_2O_3 – Fe_2O_3 is very complex and sensitive to a lot of synthesis parameters such as the type of complexing agent, pH value as well as calcination time and temperature. Furthermore, $BiFeO_3$ and $Bi_2Fe_4O_9$ were observed to always crystallize side by side from ~680 K to ~920 K therefore a small energy difference in the stability of these phases is expected in this temperature range. The ratio of $BiFeO_3$: $Bi_2Fe_4O_9$ for instance can be modified strongly by varying the pH value of the synthesis solution. In addition, an intermediate $(Bi_{1-x}Fe_x)FeO_3$ phase was found during the transformation of an X-ray amorphous powder into a polycrystalline $Bi_2Fe_4O_9$ (chapter 3).[1] Upon increasing temperature the $(Bi_{1-x}Fe_x)FeO_3$ structure gradually transformed into the $BiFeO_3$ perovskite phase.[1] Consequently, we could vary the Bi^{3+} and Fe^{3+} content on the A-site of the perovskite structure (ABO_3) by adjusting the crystallization time on a certain temperature and two samples with $x_{Fe} = 0.15$ and 0.25 were produced (chapter 4).[2] Both $(Bi_{0.75}Fe_{0.25})FeO_3$ and $(Bi_{0.85}Fe_{0.15})FeO_3$ showed interesting superparamagnetic behaviour and significantly changed crystal-physico-chemical properties such as polyhedral distortion, thermal expansion, Debye temperature, vibrational and magnetic properties compared to the stoichiometric $BiFeO_3$.[2] A further study, was attributed to the evolution of the structural, morphological, optical and vibrational properties of samples with varying $BiFeO_3$: $Bi_2Fe_4O_9$ phase ratios (chapter 5).[3] It was found that some of the samples possessed functionalized surfaces covered by 4 − 13 nm sized particles, whose lattice fringes rearranged by the interaction with the

electron beam during the TEM measurements.[3] Besides that, the study indicated that the combination of the recently proposed derivative absorption spectrum fitting (DASF) method and the Tauc's method, can be a suitable tool to concomitantly determine the band gap as well as the nature of transition (direct and indirect) of a semiconducting material.[3] By using this approach the nature of optical transitions in $Bi_2Fe_4O_9$ was found to be very likely attributable to direct transitions which was an ongoing topic of debate before.[3] The band gaps of the materials were observed to range from 1.80(1) to 2.75(3) eV.[3] Furthermore, the structure-property relationships depending on the crystallite size of $Bi_2Fe_4O_9$ were studied using structural and spectroscopic methods (chapter 6).[4] Rietveld analyses revealed a substantial change of lattice parameters *a*, *b, c* and micro-strain as a function of average crystallite size below 122(2) nm.[4] At the same time huge distortions of both the FeO_4 and FeO_6 coordinations, a significant mode softening and broadening of Raman lines, a decrease of the antiferromagnetic transition enthalpy and a changed local spin orientation in comparison to the bulk could be observed in the same size-regime.[4]

(1) Kirsch, A.; Murshed, M. M.; Gaczynski, P.; Becker, K.-D.; Gesing, T. M. $Bi_2Fe_4O_9$: Structural Changes from Nano- to Micro-Crystalline State. *Zeitschrift für Naturforsch. B J. Chem. Sci.* **2016**, *71* (5), 447–455.

(2) Kirsch, A.; Murshed, M. M.; Kirkham, M. J.; Huq, A.; Litterst, F. J.; Gesing, T. M. Temperature-Dependent Structural and Spectroscopic Studies of $(Bi_{1-x}Fe_x)FeO_3$. *J. Phys. Chem. C, submitted for publication* **2018**.

(3) Kirsch, A.; Murshed, M. M.; Schowalter, M.; Rosenauer, A.; Gesing, T. M. Nanoparticle Precursor into Polycrystalline $Bi_2Fe_4O_9$: An Evolutionary Investigation of Structural, Morphological, Optical, and Vibrational Properties. *J. Phys. Chem. C* **2016**, *120* (33), 18831–18840.

(4) Kirsch, A.; Murshed, M. M.; Litterst, F. J.; Gesing, T. M. Structural, spectroscopic and thermoanalytic studies on $Bi_2Fe_4O_9$: tunable properties driven by nano- and poly-crystalline states *J. Phys. Chem. C* **2018***, submitted for publication.*

Thesis structure

The major focus of the research work presented in this dissertation is based on the investigation of the complex and sensitive phase system $Bi_2O_3 – Fe_2O_3$. A lot of efforts have been made to study the synthesis conditions, structure-property relationships, temperature-dependent behaviour and size-dependent properties of the multiferroic system $BiFeO_3 – Bi_2Fe_4O_9$. The thesis is mainly composed of journal articles published or submitted for publication that are listed in the next section. An introduction provides background information and key insights into the relevant literature addressed in subsequent chapters. It is followed by an experimental section where an overview of the synthesis conditions, the experimental methods and a declaration on the own contributions to the publications is given. The thesis can roughly be divided into two main parts: (1) Detailed investigations on the transformation of a nanocrystalline precursor into polycrystalline $Bi_2Fe_4O_9$ and (2) the study of structure-property relationships based on the average crystallite size, chemical composition and phase composition. Chapter 2 is based on a manuscript in preparation reporting on the synthesis parameters that influence the resulting $Bi_2Fe_4O_9$ precursors and calcined samples. Chapter 3 is a journal article reporting on the transformation of a nanocrystalline precursor material into a perovskite-type bismuth ferrate followed by a second transformation into mullite-type $Bi_2Fe_4O_9$. The structural changes were mainly studied *in situ* and a metastable perovskite-type structure $(Bi_{1-x}Fe_x)FeO_3$ with varying composition depending on the progress of crystallization was found. In a follow-up study, compounds with $x_{Fe} = 0.15$ and 0.25 were synthesized and studied by *ex situ* as well *as in situ* experiments. These results were recently submitted for publication and are presented in chapter 4. The transformation of a nanocrystalline precursor into polycrystalline $Bi_2Fe_4O_9$ was also studied by *ex situ* methods. A special focus was placed on the structural, morphological, optical and vibrational properties in dependence of the phase composition of the samples. These results are published in a journal article and described in detail in chapter 5. Chapter 6 is a journal article recently submitted for publication and reports on the size-dependent structural and physical properties of $Bi_2Fe_4O_9$ using X-ray diffraction (XRD), TEM, thermal, optical and vibrational methods. The thesis ends with a concluding discussion and recommendations for future studies. All references are given separately for each chapter.

Chapter 1

Introduction

Worldwide, researchers and engineers permanently endeavor to improve and discover new technologies to face the grand challenges of today's society such as pollution control, healthcare, climate change and energy supply. Since materials limit the performance and size of devices the understanding and design of them play a key role in developing the relevant technologies. At present, most of them are based on materials in the microscale for instance in the field of biomaterials, electronics and fabrication of alloys and ceramics for mechanical applications. Richard Feynman's talk "There's Plenty of Room at the Bottom" at the meeting of the American Physical Society in 1959[1] brought at the first time the inspiration for the field of nanoscience.[2] Nowadays, it is expected that nanotechnology will revolutionize many areas of the modern society like in medicine, biotechnology, electronics, information technology, communication technology and manufacturing.[3] The physics of microcrystalline materials are mainly the same as that of macroscopic systems. Whereas, the properties of nanoscale materials of the same chemical composition can show enhanced optical, magnetic, mechanical and electronic properties relative to that of their corresponding bulk materials. These observations are attributed to the reduction in dimensionality that causes the domination of quantum effects and a greatly enlarged surface area. Furthermore, nanostructures can possess unusual forms of structural disorder and internal strain that can significantly alter the materials properties.[4]

In the nano-size regime the physical properties are often found to depend on the size of a given system offering a good opportunity for tailoring the materials performance to certain applications. Several examples from literature showed how the materials can be tuned by the control of their size, for instance, the photoluminescence in organometal halide perovskite nanoplatelets[5], piezoelectric effect in $BaTiO_3$[6], magnetic properties in $BiFeO_3$[7], catalytic performances of oxidation and reduction reactions on nanocatalysts[8] and polar ordering in colloidal GeTe nanocrystals[9]. There even exist structures that develop new physico-chemical properties in the nanoscale e.g. superparamagnetic behaviour.[10] Superparamagnetism is generally observed in very small magnetic materials such as magnetite.[11] Due to fast fluctuations of the directions of magnetic moments, a superparamagnet behaves paramagnetically even

below the Curie or Néel temperature. It can highly be magnetized by an external magnetic field without showing a remanent magnetization after its removal.

Another promising approach to feature key technologies is the control of coexisting and coupled 'ferroic' properties (such as ferroelectricity, ferromagnetism and ferroelasticity) by external stimuli.[12,13] Those materials simultaneously exhibiting more than one of the ferroic order parameters are called multiferroics. Multiferroic properties can exist in multiphase systems[11] but also in single-phased materials such as CuO[14], lead-iron mixed perovskites (e.g. $PbFe_{0.5}Ta_{0.5}O_3$, $PbFe_{0.5}Nb_{0.5}O_3$)[14], Cr_2O_3[14] and $BiFeO_3$[15]. Nevertheless, the existence of multiferroic properties in single-phased materials is rare.[13] Since 2003, the interest in materials possessing multiferroic properties has been growing rapidly as shown in Figure 1.

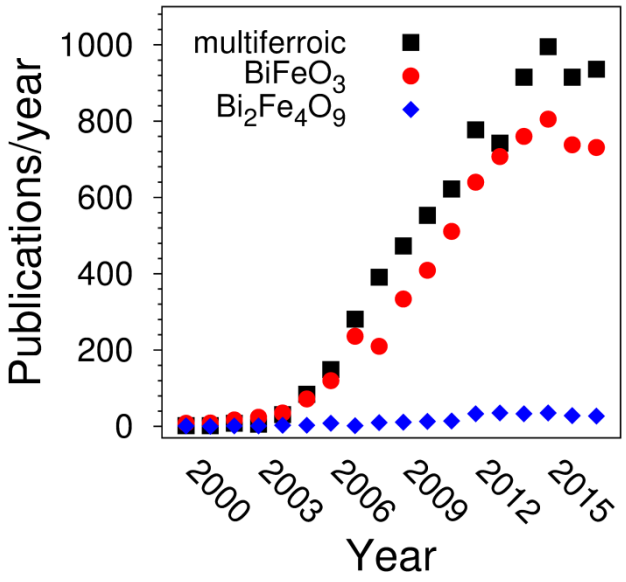

Figure 1. Publications per year using the keywords 'multiferroic', '$BiFeO_3$' and '$Bi_2Fe_4O_9$' (web of science).

Many multiferroics only work at low temperatures making them impractical for commercial device applications, however some room-temperature (or near room-temperature) multiferroics exist.[14] Among them, $BiFeO_3$ is by far the most studied and prominent structure since it is simultaneously ferroelectric and antiferromagnetic at room temperature[16] with high Curie and Néel temperatures of ~1100 K and ~ 640 K, respectively.[17] The publications per year almost reach the numbers of the ones to be concerned with the keyword 'multiferroic' (Figure 1). In spite of intense investigations on $BiFeO_3$ in many forms - such as nanoparticles,[7,18] single crystals,[19] polycrystals[20]

and thin films[15,21] - some of its physical properties are not fully understood. There have been ongoing debates on contradictory results[7,18,22] and Catalan and Scott (2009)[22] encouraged to conduct further systematic studies on the crystal chemistry, phase diagram, structure and dynamics of $BiFeO_3$. Furthermore, great efforts have been made in recent years to enhance the already interesting properties of $BiFeO_3$ by substitution of the A and B site cations reviewed by Silva et al. (2011).[23] $BiFeO_3$ crystallizes in space group *R*3*c* and can be described as a rhombohedrally distorted perovskite as shown in Figure 2. The structure exhibits an interesting canted magnetic spiral spin arrangement with a periodic length of 62 nm[24] and at the same time a spontaneous polarization in the hexagonal c-direction.[25]

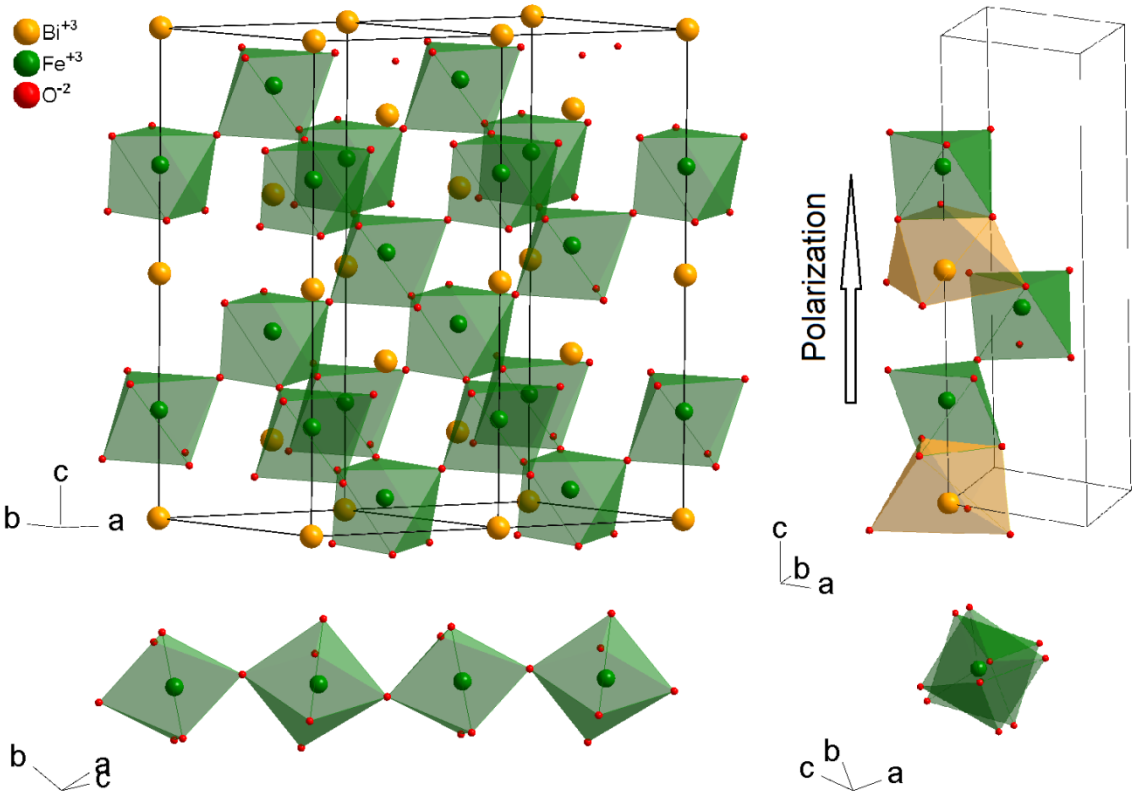

Figure 2. Crystal structure of $BiFeO_3$, showing some polyhedral coordinations and their connectivity.

Besides the $BiFeO_3$ structure, the Bi_2O_3 - Fe_2O_3 phase system possesses a further structure with quite interesting properties that is the mullite-type $Bi_2Fe_4O_9$. Until today, this compound received little attention in literature in comparison with $BiFeO_3$ (Figure 1). Surprisingly, $Bi_2Fe_4O_9$ is often only mentioned as an unwanted impurity in the synthesis of $BiFeO_3$[23,26-29], although it is found to be the first experimental analogue of a geometrically frustrated Cairo pentagonal magnetic lattice[30] and exhibits

multiferroic properties near room temperature.[31] Besides that, interesting magnetic[32], electronic[33], optic[34] and catalytic[35] properties are reported as well. $Bi_2Fe_4O_9$ crystallizes in the orthorhombic space group *Pbam* in a mullite-type structure as depicted in Figure 3. It is built up from the typical edge-sharing octahedral chains along the c-axis that are connected by corner-shared Fe_2O_7 double tetrahedral units. As in $BiFeO_3$, the $6s^2$ lone electron pair of Bi^{3+} is stereochemically active in $Bi_2Fe_4O_9$.[36] Furthermore, the structure shows an interesting crystal chemistry.[37-40]

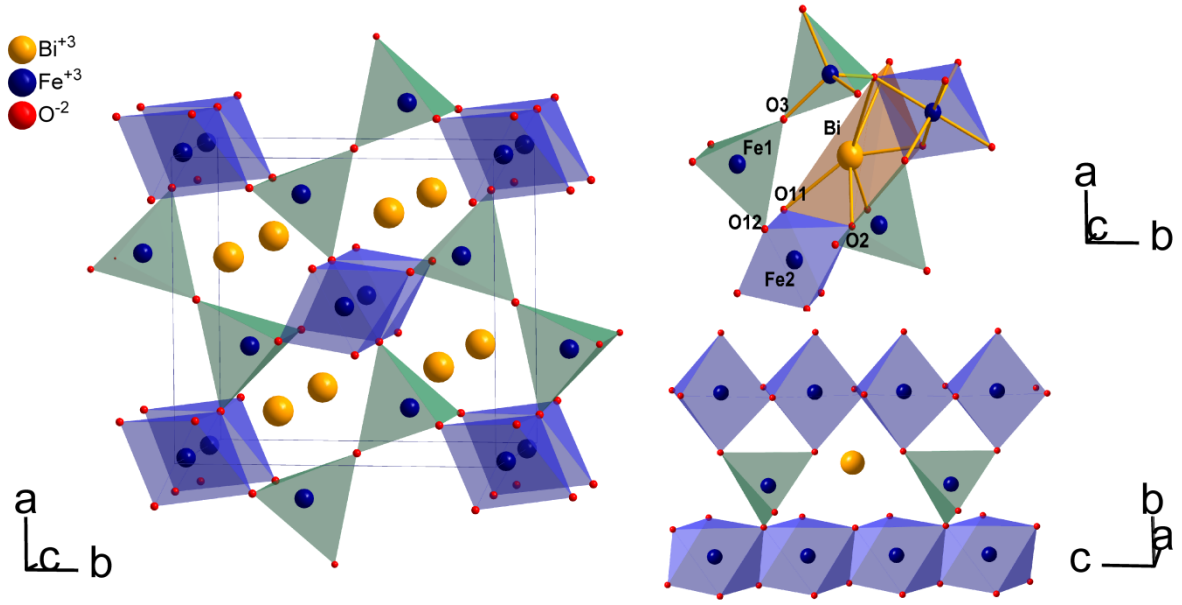

Figure 3. Crystal structure of $Bi_2Fe_4O_9$, showing some polyhedral coordinations and their connectivity.

The phase system Bi_2O_3 - Fe_2O_3 seems to be very sensitive since several compounds – such as $Bi_2Fe_4O_9$[28], $Bi_{25}FeO_{40}$[28], $Bi_{24}Fe_2O_{39}$[28], α-Bi_2O_3 or β-Bi_2O_3[41] and α-Fe_2O_3[42] - are reported to crystallize simultaneously depending on the synthesis conditions used. Jia et al. (2015)[19] for instance revealed a very sluggish phase evolution behaviour for $BiFeO_3$ supported by TEM and Monte Carlo simulations. Thus, the sensitivity of this system provides a great opportunity to finetune the materials properties to a large extent.

The properties of a material obviously can be changed by tuning its dimensionality as well as substitution of elements in the crystal structure. But materials can also show a varying performance depending on the content of two or more phases and/or their degree of crystallinity. As an example, in the case of the photocatalytic active semiconductor TiO_2 was found that a mixture of rutile and anatase (e.g.,1:3.4) is

more active than pure nanocrystalline anatase powder, although anatase is usually considered to be the active polymorph.[43] Furthermore, Maity et al. (2013)[44] reported on a superspin glass mediated giant spontaneous exchange bias in a nanocomposite of $BiFeO_3$ - $Bi_2Fe_4O_9$. These are two examples why it is also interesting to study the properties of phase mixtures besides pure-phase systems.

Within the scope of this dissertation mainly the following questions were addressed:

- Which synthesis parameters influence the formation of $BiFeO_3$ and $Bi_2Fe_4O_9$?
- Is it possible to produce very small crystallites of $Bi_2Fe_4O_9$ without the formation of $BiFeO_3$?
- What is happening during the transformation of a precursor material into polycrystalline $Bi_2Fe_4O_9$?
- How do the average crystallite size, chemical and phase composition change the physical properties of the materials?

References

(1) Feynman, R. P. Plenty of room at the bottom. (talk in December **1959**) http://www.zyvex.com/nanotech/feynman.html (accessed Jul 18, 2018).

(2) Rogers, B.; Adams, J.; Pennathur, S. *Nanotechnology: Understanding Small Systems*, Third edit.; CRC Press, **2015**.

(3) The Royal Society & The Royal Academy of Engineering *Nanoscience and Nanotechnologies : Opportunities and Uncertainties*; **2004**.

(4) Gilbert, B.; Huang, F.; Zhang, H.; Waychunas, G. A.; Banfield, J. F. Nanoparticles: Strained and Stiff. *Science* **2004**, *305* (5684), 651–654.

(5) Sichert, J. A.; Tong, Y.; Mutz, N.; Vollmer, M.; Fischer, S.; Milowska, K. Z.; García Cortadella, R.; Nickel, B.; Cardenas-Daw, C.; Stolarczyk, J. K.; et al. Quantum Size Effect in Organometal Halide Perovskite Nanoplatelets. *Nano Lett.* **2015**, *15* (10), 6521–6527.

(6) Majdoub, M. S.; Sharma, P.; Cagin, T. Enhanced Size-Dependent Piezoelectricity and Elasticity in Nanostructures due to the Flexoelectric Effect. *Phys. Rev. B* **2008**, *77* (12), 125424-1–9.

(7) Park, T.; Papaefthymiou, G. C.; Viescas, A. J.; Moodenbaugh, A. R.; Wong, S. S. Size-Dependent Magnetic Properties of Single-Crystalline Multiferroic $BiFeO_3$ Nanoparticles. *Nano Lett.* **2007**, *7* (3), 766–772.

(8) Cao, S.; Tao, F. F.; Tang, Y.; Li, Y.; Yu, J. Size- and Shape-Dependent Catalytic Performances of Oxidation and Reduction Reactions on Nanocatalysts. *Chem. Soc. Rev.* **2016**, *45* (17), 4747–4765.

(9) Polking, M. J.; Urban, J. J.; Milliron, D. J.; Zheng, H.; Chan, E.; Caldwell, M. A.; Raoux, S.; Kisielowski, C. F.; Ager, J. W.; Ramesh, R.; et al. Size-Dependent Polar Ordering in Colloidal GeTe Nanocrystals. *Nano Lett.* **2011**, *11* (3), 1147–1152.

(10) Xuan, S.; Wang, Y.-X. J.; Yu, J. C.; Cham-Fai Leung, K. Tuning the Grain Size

and Particle Size of Superparamagnetic Fe_3O_4 Microparticles. *Chem. Mater.* **2009**, *21* (21), 5079–5087.
(11) Mikhaylova, M.; Kim, D. K.; Bobrysheva, N.; Osmolowsky, M.; Semenov, V.; Tsakalakos, T.; Muhammed, M. Superparamagnetism of Magnetite Nanoparticles: Dependence on Surface Modification. *Langmuir* **2004**, *20* (6), 2472–2477.
(12) Eerenstein, W.; Mathur, N. D.; Scott, J. F. Multiferroic and Magnetoelectric Materials. *Nature* **2006**, *442* (7104), 759–765.
(13) Hill, N. A. Why Are There so Few Magnetic Ferroelectrics? *J. Phys. Chem. B* **2000**, *104* (29), 6694–6709.
(14) Scott, J. F. Room-Temperature Multiferroic Magnetoelectrics. *NPG Asia Mater.* **2013**, *5* (11), e72.
(15) Zhao, T.; Scholl, A.; Zavaliche, F.; Lee, K.; Barry, M.; Doran, A.; Cruz, M. P.; Chu, Y. H.; Ederer, C.; Spaldin, N. A.; et al. Electrical Control of Antiferromagnetic Domains in Multiferroic $BiFeO_3$ Films at Room Temperature. *Nat. Mater.* **2006**, *5* (10), 823–829.
(16) Park, J.-G.; Le, M. D.; Jeong, J.; Lee, S. Structure and Spin Dynamics of Multiferroic $BiFeO_3$. *J. Phys. Condens. Matter* **2014**, *26* (43), 433202.
(17) Fischer, P.; Polomska, M.; Sosnowska, I.; Szymanski, M. Temperature Dependence of the Crystal and Magnetic Structures of $BiFeO_3$. *J. Phys. C Solid State Phys.* **1980**, *13* (10), 1931–1940.
(18) Huang, F.; Wang, Z.; Lu, X.; Zhang, J.; Min, K.; Lin, W.; Ti, R.; Xu, T.; He, J.; Yue, C.; et al. Peculiar Magnetism of $BiFeO_3$ Nanoparticles with Size Approaching the Period of the Spiral Spin Structure. *Sci. Rep.* **2013**, *3* (1), 2907.
(19) Jia, C.-L.; Jin, L.; Wang, D.; Mi, S.-B.; Alexe, M.; Hesse, D.; Reichlova, H.; Marti, X.; Bellaiche, L.; Urban, K. W. Nanodomains and Nanometer-Scale Disorder in Multiferroic Bismuth Ferrite Single Crystals. *Acta Mater.* **2015**, *82*, 356–368.
(20) Kalinin, S. V; Suchomel, M. R.; Davies, P. K.; Bonnell, D. A. Potential and Impedance Imaging of Polycrystalline $BiFeO_3$ Ceramics. *J. Am. Ceram. Soc.* **2002**, *85* (12), 3011–3017.
(21) Ko, K.-T.; Jung, M. H.; He, Q.; Lee, J. H.; Woo, C. S.; Chu, K.; Seidel, J.; Jeon, B.-G.; Oh, Y. S.; Kim, K. H.; et al. Concurrent Transition of Ferroelectric and Magnetic Ordering near Room Temperature. *Nat. Commun.* **2011**, *2* (1), 567.
(22) Catalan, G.; Scott, J. F. Physics and Applications of Bismuth Ferrite. *Adv. Mater.* **2009**, *21* (24), 2463–2485.
(23) Silva, J.; Reyes, A.; Esparza, H.; Camacho, H.; Fuentes, L. $BiFeO_3$: A Review on Synthesis, Doping and Crystal Structure. *Integr. Ferroelectr.* **2011**, *126* (1), 47–59.
(24) Sosnowska, I.; Neumaier, T. P.; Steichele, E. Spiral Magnetic Ordering in Bismuth Ferrite. *J. Phys. C Solid State Phys.* **1982**, *15* (23), 4835–4846.
(25) Ruette, B.; Zvyagin, S.; Pyatakov, A. P.; Bush, A.; Li, J. F.; Belotelov, V. I.; Zvezdin, A. K.; Viehland, D. Magnetic-Field-Induced Phase Transition in $BiFeO_3$ Observed by High-Field Electron Spin Resonance: Cycloidal to Homogeneous Spin Order. *Phys. Rev. B* **2004**, *69* (6), 64114.
(26) Rojac, T.; Bencan, A.; Malic, B.; Tutuncu, G.; Jones, J. L.; Daniels, J. E.; Damjanovic, D. $BiFeO_3$ Ceramics: Processing, Electrical, and Electromechanical Properties. *J. Am. Ceram. Soc.* **2014**, *97* (7), 1993–2011.
(27) Ortiz-Quiñonez, J. L.; Díaz, D.; Zumeta-Dubé, I.; Arriola-Santamaría, H.; Betancourt, I.; Santiago-Jacinto, P.; Nava-Etzana, N. Easy Synthesis of High-

Purity $BiFeO_3$ Nanoparticles: New Insights Derived from the Structural, Optical, and Magnetic Characterization. *Inorg. Chem.* **2013**, *52* (18), 10306–10317.
(28) Liu, T.; Xu, Y.; Zhao, J. Low-Temperature Synthesis of $BiFeO_3$ via PVA Sol-Gel Route. *J. Am. Ceram. Soc.* **2010**, *93* (11), 3637–3641.
(29) Xian, T.; Yang, H.; Shen, X.; Jiang, J. L.; Wei, Z. Q.; Feng, W. J. Preparation of High-Quality $BiFeO_3$ Nanopowders via a Polyacrylamide Gel Route. *J. Alloys Compd.* **2009**, *480* (2), 889–892.
(30) Ressouche, E.; Simonet, V.; Canals, B.; Gospodinov, M.; Skumryev, V. Magnetic Frustration in an Iron-Based Cairo Pentagonal Lattice. *Phys. Rev. Lett.* **2009**, *103* (26), 267204.
(31) Singh, A. K.; Kaushik, S. D.; Kumar, B.; Mishra, P. K.; Venimadhav, A.; Siruguri, V.; Patnaik, S. Substantial Magnetoelectric Coupling near Room Temperature in $Bi_2Fe_4O_9$. *Appl. Phys. Lett.* **2008**, *92* (13), 132910.
(32) Tian, Z. M.; Yuan, S. L.; Wang, X. L.; Zheng, X. F.; Yin, S. Y.; Wang, C. H.; Liu, L. Size Effect on Magnetic and Ferroelectric Properties in $Bi_2Fe_4O_9$ Multiferroic Ceramics. *J. Appl. Phys.* **2009**, *106* (10), 103912.
(33) Li, Y.; Zhang, Y.; Ye, W.; Yu, J.; Lu, C.; Xia, L. Photo-to-Current Response of $Bi_2Fe_4O_9$ Nanocrystals Synthesized through a Chemical Co-Precipitation Process. *New J. Chem.* **2012**, *36* (6), 1297–1300.
(34) Zhang, Q.; Gong, W.; Wang, J.; Ning, X.; Wang, Z.; Zhao, X.; Ren, W.; Zhang, Z. Size-Dependent Magnetic, Photoabsorbing, and Photocatalytic Properties of Single-Crystalline $Bi_2Fe_4O_9$ Semiconductor Nanocrystals. *J. Phys. Chem. C* **2011**, *115*, 25241–25246.
(35) Zakharchenko, N. I. Catalytic Properties of the System Fe_2O_3 - Bi_2O_3 in Ammonia Oxidation to Nitrogen Oxides. *Kinet. Catal.* **2002**, *43* (3), 95–98.
(36) Curti, M.; Gesing, T. M.; Murshed, M. M.; Bredow, T.; Mendive, C. B. Liebau Density Vector: A New Approach to Characterize Lone Electron Pairs in Mullite-Type Materials. *Zeitschrift für Krist. - Cryst. Mater.* **2013**, *228* (12), 629–634.
(37) Gesing, T. M.; Fischer, R. X.; Burianek, M.; Mühlberg, M.; Debnath, T.; Rüscher, C. H.; Ottinger, J.; Buhl, J.-C.; Schneider, H. Synthesis and Properties of Mullite-Type $(Bi_{1-x}Sr_x)_2(M1_{1-y}M2_y)_4O_{9-x}$ (M = Al, Ga, Fe). *J. Eur. Ceram. Soc.* **2011**, *31* (16), 3055–3062.
(38) Schneider, H.; Fischer, R. X.; Gesing, T. M.; Schreuer, J.; Mühlberg, M. Crystal Chemistry and Properties of Mullite-Type $Bi_2M_4O_9$: An Overview. *Int. J. Mater. Res.* **2012**, *103* (4), 422–429.
(39) Weber, S.-U.; Gesing, T. M.; Röder, J.; Litterst, F. J.; Fischer, R. X.; Becker, K.-D. Temperature-Dependent 57Fe Mössbauer Spectroscopy and Local Structure of Mullite-Type Bi2(FexAl1-x)4O9 (0.1<x<1) Solid Solutions. *Int. J. Mater. Res.* **2012**, *103*, 430–437.
(40) Weber, S.-U.; Gesing, T. M.; Eckold, G.; Fischer, R. X.; Litterst, F.-J.; Becker, K.-D. Temperature-Dependent ^{57}Fe Mössbauer Spectroscopy and Local Structure of the Mullite-Type $Bi_2(Fe_xGa_{1-x})_4O_9$ (0.1<x1) Solid Solution. *J. Phys. Chem. Solids* **2014**, *75*, 416–426.
(41) Chen, J.-C.; Wu, J.-M. Dielectric Properties and Ac Conductivities of Dense Single-Phased $BiFeO_3$ Ceramics. *Appl. Phys. Lett.* **2007**, *91* (18), 182903.
(42) Da Silva, K. L.; Menzel, D.; Feldhoff, A.; Kübel, C.; Bruns, M.; Paesano, A.; Düvel, A.; Wilkening, M.; Ghafari, M.; Hahn, H.; et al. Mechanosynthesized $BiFeO_3$ Nanoparticles with Highly Reactive Surface and Enhanced Magnetization. *J. Phys. Chem. C* **2011**, *115* (15), 7209–7217.
(43) Bakardjieva, S.; Šubrt, J.; Štengl, V.; Dianez, M. J.; Sayagues, M. J.

Photoactivity of Anatase–rutile TiO_2 Nanocrystalline Mixtures Obtained by Heat Treatment of Homogeneously Precipitated Anatase. *Appl. Catal. B Environ.* **2005**, *58* (3–4), 193–202.

(44) Maity, T.; Goswami, S.; Bhattacharya, D.; Roy, S. Superspin Glass Mediated Giant Spontaneous Exchange Bias in a Nanocomposite of $BiFeO_3$ - $Bi_2Fe_4O_9$. *Phys. Rev. Lett.* **2013**, *110* (10), 107201.

Chapter 2

Experimental overview

Synthesis description

The samples resulting from this dissertation were mainly synthesized by sol-gel methods using the corresponding metal nitrates and varying chelating agents. In general, after the dissolution of the metal nitrates into a solvent the solution is heated while stirring to a certain temperature for a defined time. This is followed by a drying step and subsequent grinding. Then the resulting precursors are calcined at defined temperatures and dwelling times. The general procedure is depicted in Figure 4.

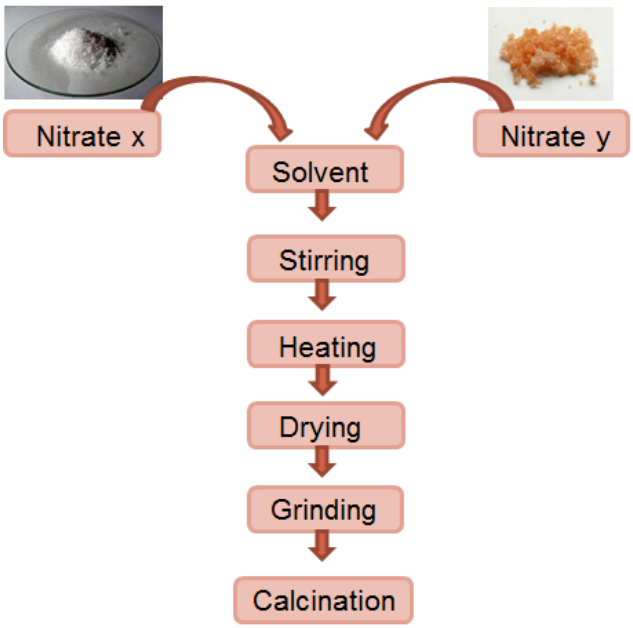

Figure 4. Scheme of general synthesis procedure mainly used in this works.

To understand how the resulting structures and properties can be modified by the synthesis conditions several parameters were varied. These include:

- type of complexing agent (glycerine, polyols, polyvinyl alcohols, sugar alcohols)
- pH value
- calcination time
- calcination temperature
- chemical composition

By varying these parameters 182 different precursor materials were synthesized in total. All the examined parameters were found to have a substantial influence on the resulting phase composition and their kinetics, structures and corresponding properties. In summary, due to the high sensitivity to the synthesis conditions and its very interesting and unique properties the system $BiFeO_3$ – $Bi_2Fe_4O_9$ provides a huge potential for tailoring the materials properties for certain applications.

In the following section, selected examples are presented to give an impression of the various parameters that influence the resulting samples. For instance, Figure 5 shows micrographs of six differently synthesized precursor materials of $Bi_2Fe_4O_9$ chemical composition with their corresponding XRD patterns. They were synthesized by the polyol process[1-4] using polyols as high-boiling solvents heated under reflux. The polyols (e.g. ethylene glycol, diethylene glycol) also function as reducing agent and stabilizer to hinder particle growth.[5] Their synthesis conditions are summarized in Table 1. The precursors vary in their particle size, morphology, structural composition and crystallinity. While sample a, b and d mainly exhibit agglomerates of uniform spherical particles sample c, e and f appear to be totally different (Figure 5). Sample c, for instance, possesses spherical agglomerates of ~25 µm beside cuboid like structures of bigger size (~80 µm) and sample f shows hollow spheres of ~1 µm. Furthermore, the XRD patterns differ strongly. Sample a, b and e are X-ray amorphous having no distinct reflections, whereas c, d and f clearly show crystalline parts (Figure 5). The reflections in sample c and d, for instance, can be assigned to elemental Bi in space group $R\bar{3}m$[6], whereas sample f also contains β-Bi_2O_3 in space group $P\bar{4}2_1c$[7].

Table 1. Selected synthesis conditions of samples produced by the polyol process.

Sample	Solvent	Synthesis time /min	Synthesis temperature /K	Additives
A	DEG	120	413	NaOH; stearic acid
B	DEG	120	423	-
C	DEG	20 1080 120	443 473 493	No reflux
D	TEG	120	430	-
E	EG	60 240	373 416	-
F	EG	120	443	No reflux

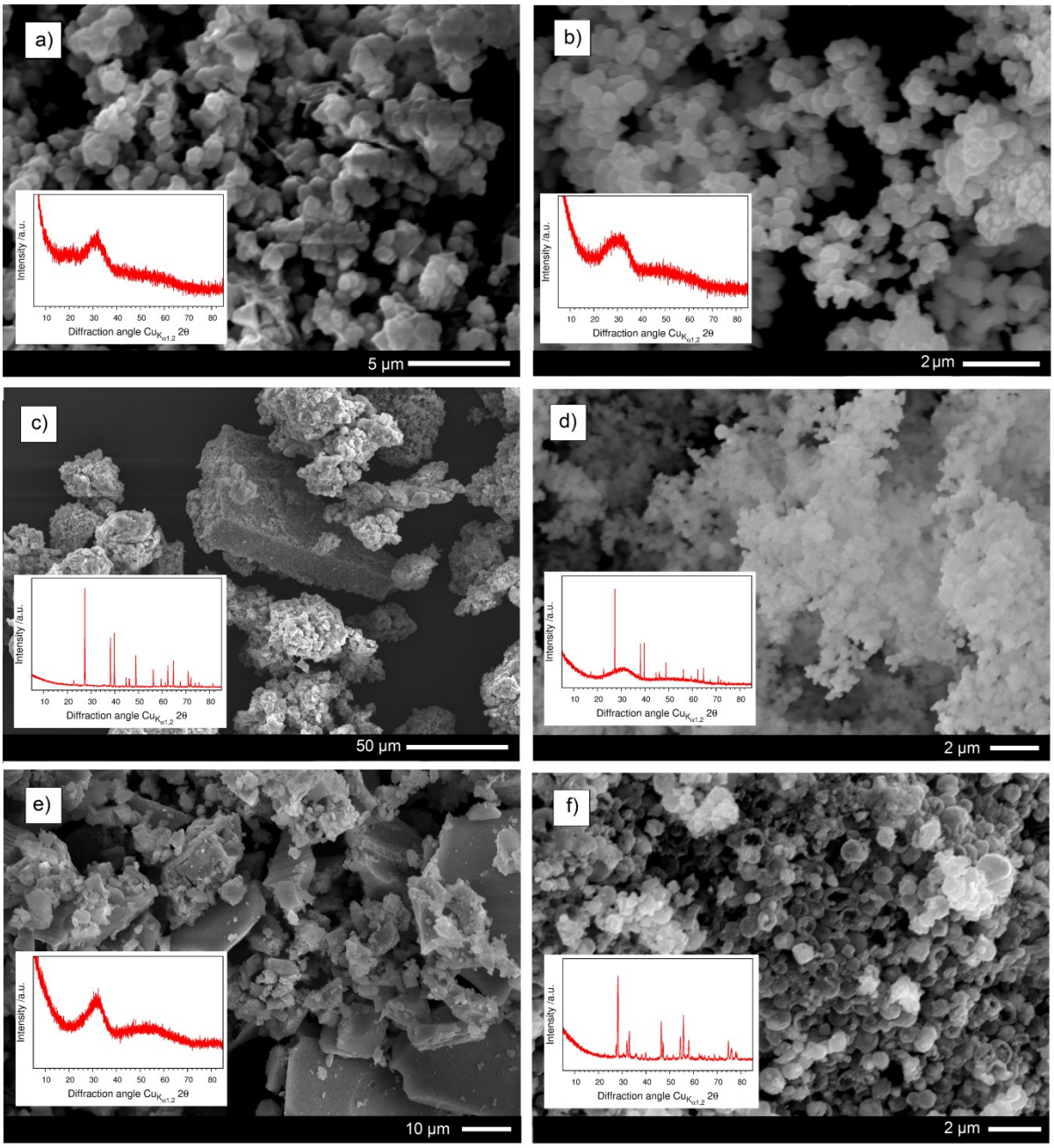

Figure 5. Precursor materials of $Bi_2Fe_4O_9$ composition and their corresponding XRD patterns. The synthesis conditions are given in Table 1.

The influence of the solvent on the resulting precursor was studied systematically by varying the type of polyol. In this study different glycol ethers such as ethylene glycol (EG), diethylene glycol (DEG), triethylene glycol (TREG) and tetraethylene glycol (TEG) as well as mixtures of them were used. The XRD patterns of the corresponding $Bi_2Fe_4O_9$ precursors are presented in Figure 6. In detail, 5 mmol $Bi(NO_3)_3 \cdot 5H_2O$ and 10 mmol $Fe(NO_3)_3 \cdot 9H_2O$ were dissolved into 0.35 mol polyol. The mixture was heated for two hours in a three-necked flask under reflux using a metal

bath at 423 K. After cooling down to ambient conditions, the suspension was separated by centrifugation and washed several times with acetone. The type of polyol used shows a strong influence on the resulting XRD patterns of the precursors (Figure 6). Almost all patterns show huge x-ray amorphous humps. Interestingly, the samples synthesized using a mixture of EG/DEG and EG/TREG have a higher degree of crystallinity. The pattern of the DEG sample shows no distinct reflections and the phase crystallizing when EG is used could not be assigned to a known phase. Elemental Bi in space group $R\bar{3}m$[6], however, could be identified in the samples synthesized in TREG and TEG.

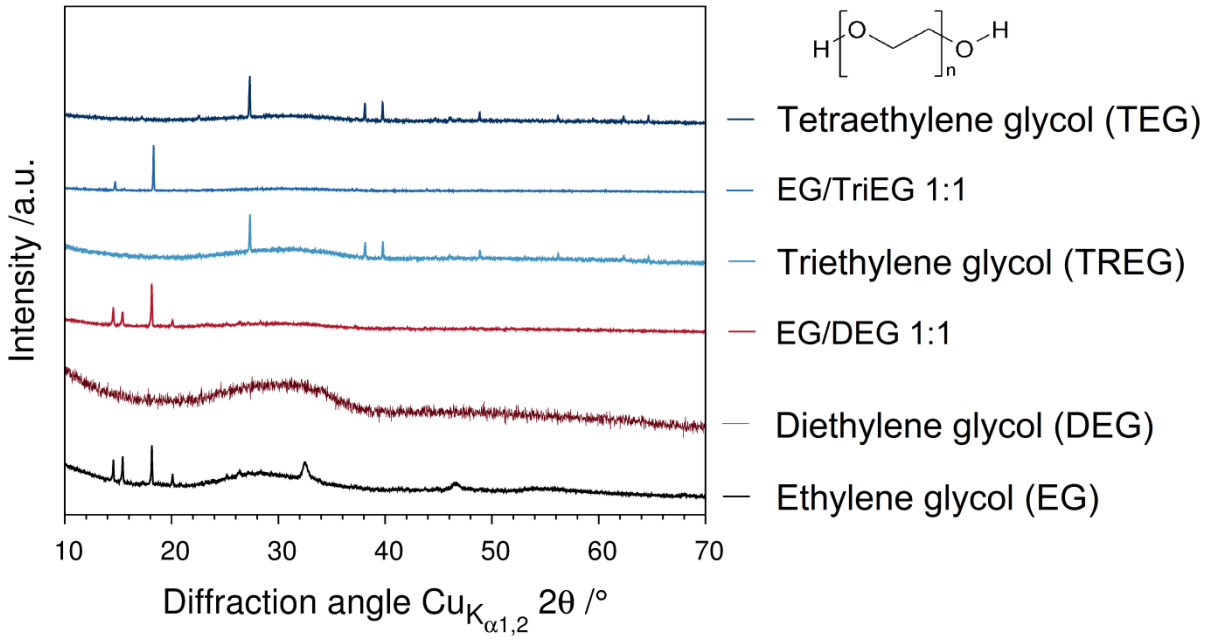

Figure 6. $Bi_2Fe_4O_9$ precursor synthesized by the polyol method using different polyols.

Besides the polyol process a substantial faster and easier sol-gel procedure was also investigated using polyvinyl alcohols (PVA) with different molecular weights or sorbitol as complexing agents. In general, the metal nitrates (5 mmol $Bi(NO_3)_3 \cdot 5H_2O$ and 10 mmol $Fe(NO_3)_3 \cdot 9H_2O$) were dissolved in 40 mL of a 5%-solution of alcohol in deionized water. The mixture was heated in a beaker using a glycerine bath (353 – 373 K) until a solid foam or viscous gel was obtained. Then it was dried in an oven at 523 K, grinded and calcined varying the calcination temperature and time.

Following this procedure using sorbitol as the complexing agent, the influence of the pH value of the synthesis solution on the phase ratio of perovskite-type $BiFeO_3$ to

mullite-type $Bi_2Fe_4O_9$ in calcined samples (here 873 K for two hours) was studied. As depicted in Figure 7 the phase ratio can strongly be controlled by the pH value of the synthesis solution. The mullite-type $Bi_2Fe_4O_9$ structure is found to preferentially crystallize in an acidic medium, whereas the amount of the perovskite-type structure clearly is higher in an alkaline medium. Furthermore, it was observed that sorbitol is complexing the Bi-cations very strongly which makes it possible to work even in a highly alkaline medium without the precipitation of bismuth hydroxide.

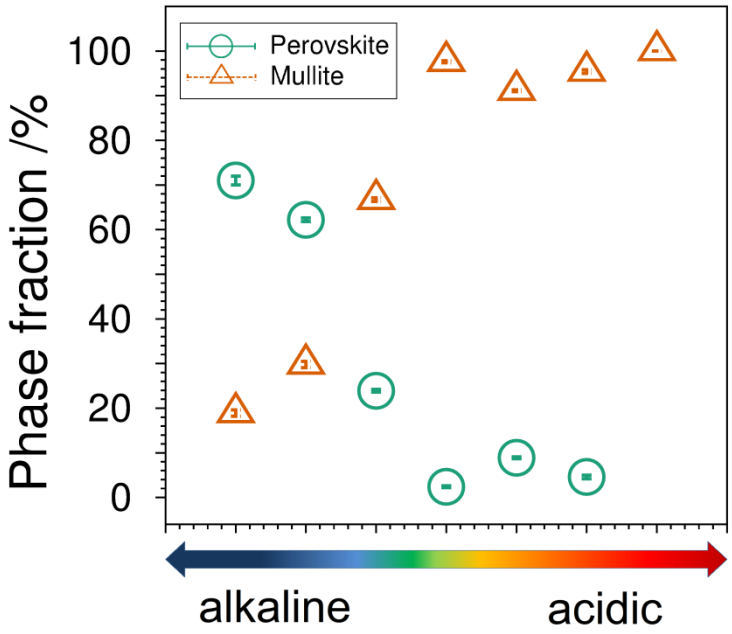

Figure 7. Influence of pH value of the synthesis solution on the phase fraction of perovskite-type $BiFeO_3$ and mullite-type $Bi_2Fe_4O_9$ in samples heated at 873 K for two hours.

The substitution of Fe in the initial chemical composition ($Bi_2Fe_4O_9$) by other elements, for instance Al, Mn and Ga, not only influences the colour of the resulting compounds (exemplarily shown in Figure 8) but also change the kinetics and pathways of crystallization into the mullite-type structure. This could be shown for the solid solution system $Bi_2(Fe_{1-x}Al_x)_4O_9$ in a recent study.[8]

In general, it can be stated that both methods, the polyol process and sol-gel procedure using PVAs, provide a promising and versatile procedure to finetune the synthesis parameters and control the resulting phase composition and their kinetics, structures and corresponding properties of the samples produced. However, the sol-gel procedure using PVAs provide some benefits compared to the polyol process. On

the one hand, the device setup is very easy and the procedure very fast. On the other hand, washing the samples synthesized by the polyol process is very time-consuming since the polyols strongly adhere to the samples surfaces[5] and several washing cycles with intermediate centrifugation steps are needed to obtain a dry powder that can be grinded and calcined.

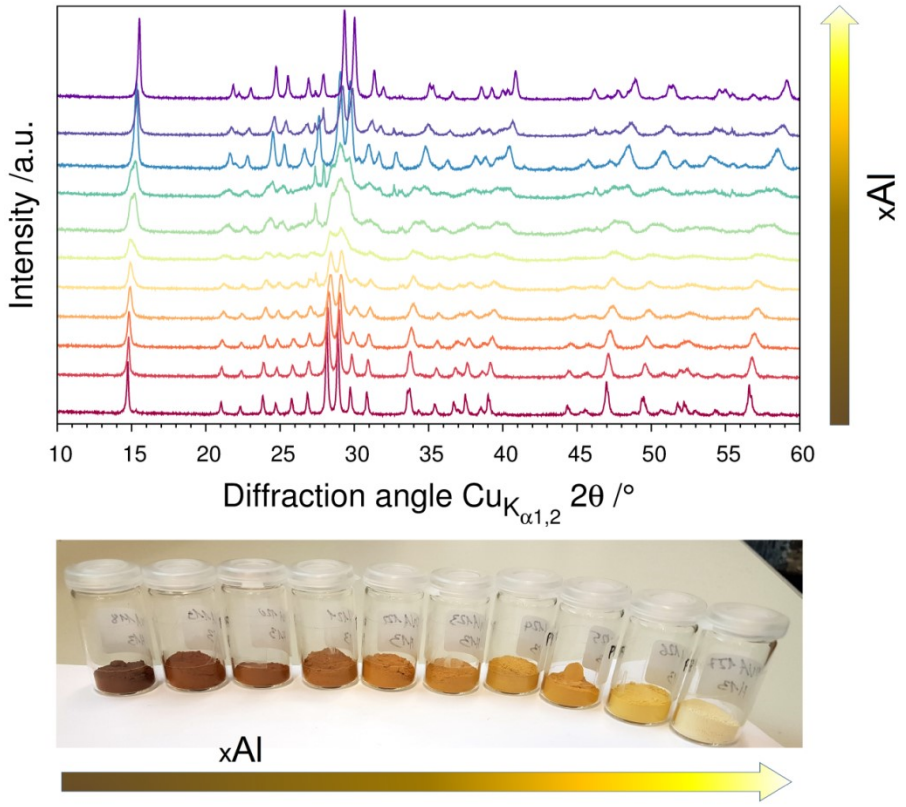

Figure 8. XRD patterns and optical appearance of solid solutions of $Bi_2(Fe_{1-x}Al_x)_4O_9$ synthesized using PVA and heated at 973 K for two hours.

References

(1) Kirsch, A.; Murshed, M. M.; Gaczynski, P.; Becker, K.-D.; Gesing, T. M. $Bi_2Fe_4O_9$: Structural Changes from Nano- to Micro-Crystalline State. *Zeitschrift für Naturforsch. B J. Chem. Sci.* **2016**, *71* (5), 447–455.

(2) Feldmann, C. Polyol-Mediated Synthesis of Nanoscale Functional Materials. *Solid State Sci.* **2005**, *7* (7), 868–873.

(3) Feldmann, C.; Jungk, H. O. Polyol-Mediated Preparation of Nanoscale Oxide Particles. *Angew. Chemie - Int. Ed.* **2001**, *40* (2), 359–362.

(4) Quievryn, C.; Bernard, S.; Miele, P. Polyol-Based Synthesis of Praseodymium Oxide Nanoparticles. *Nanomater. Nanotechnol.* **2014**, *4*, 1–8.

(5) Cai, W.; Wan, J. Facile Synthesis of Superparamagnetic Magnetite Nanoparticles in Liquid Polyols. *J. Colloid Interface Sci.* **2007**, *305*, 366–370.

(6) Robinson, R. A.; Purwanto, A.; Kohgi, M.; Canfield, P. C.; Kamiyama, T.; Ishigaki, T.; Lynn, J. W.; Erwin, R.; Peterson, E.; Movshovich, R. Crystallography and Magnetism of the Heavy-Fermion Compound YbBiPt. *Phys. Rev. B* **1994**, *50* (13), 9595–9598.
(7) Jovalekić, Č.; Zdujić, M.; Poleti, D.; Karanović, L.; Mitrić, M. Structural and Electrical Properties of the $2Bi_2O_3 \cdot 3ZrO_2$ system. *J. Solid State Chem.* **2008**, *181* (6), 1321–1329.
(8) Curti, M.; Kirsch, A.; Granone, L. I.; Tarasi, F.; López Robledo, G.; Bahnemann, D. W.; Murshed, M. M.; Gesing, T. M.; Mendive, C. B. Visible-Light Photocatalysis with Mullite-Type $Bi_2(Al_{1-x}Fe_x)_4O_9$: Striking the Balance between Bandgap Narrowing and Conduction Band Lowering. *ACS Catal.* **2018,** *8*, 8844−8855.

Experimental methods

The samples produced within the scope of this dissertation were characterized by the following methods. Furthermore, all cooperation partners and their conducted measurements are presented.

In-house experiments at the Solid State Chemical Crystallography group of Prof. Gesing, Institute of Inorganic Chemistry and Crystallography, University of Bremen, Germany:

- Synthesis
- XRD (temperature-dependent and ambient conditions)
- SEM
- UV/Vis spectroscopy
- FTIR spectroscopy
- Raman spectroscopy (temperature-dependent and ambient conditions)

TEM measurements at the Electron Microscopy group of Prof. Rosenauer, Institute of Solid State Physics, University of Bremen, Germany

^{57}Fe Mössbauer spectroscopy at the Solid State Chemistry group of Prof. Becker, Institute of Physical and Theoretical Chemistry, Technische Universität Braunschweig, Germany *and* the group of Prof. Litterst, Institute for Condensed Matter Physics, Technische Universität Braunschweig, Germany

Squid measurements at the group of Prof. Meyer, Institute of Inorganic Chemistry, Georg-August-Universität Göttingen, Germany

Neutron diffraction experiments at the high-resolution instrument POWGEN of Dr. Ashfia Huq (lead instrument scientist) of the Chemical and Engineering Materials Division, Oak Ridge National Laboratory, Oak Ridge, Tennessee 37831, USA

Synchrotron XRD experiments at the high-resolution powder diffractometer at beamline 11-BM at the Advanced Photon Source (APS), Argonne National Laboratory, USA

Declaration on own contributions to the publications

The results presented in this dissertation were obtained in collaborations with several other groups. In this section I explicitly declare my own contributions to the individual publications.

The work presented in **chapter 2** is based on a manuscript *in preparation* Kirsch, A., Murshed, M. M., Gesing, Th. M.; Facile sol-gel synthesis of $Bi_2Fe_4O_9$ and nanocomposites of the (1-x) $BiFeO_3$ · (x) $Bi_2Fe_4O_9$ system, *manuscript in preparation.*

I conducted the following tasks:

- Writing of the main manuscript
- Generation of the figures
- Conduction of SEM and XRD measurements as well as their evaluation and interpretation including Rietveld refinements

I was not involved in:

- Synthesis of the samples (done by trainees Rebecca Siemering, Jasmin Richter and Jannis Diekmann under my supervision)

The work presented in **chapter 3** was previously *published* Kirsch, A., Murshed, M. M., Gaczynski, P., Becker, K.-D., Gesing, Th. M.; $Bi_2Fe_4O_9$: Structural changes from nano- to micro-crystalline state. *Z. Naturforsch*. **2016**; *71(5)b,* 447–455.

I conducted the following tasks:

- Writing of the main manuscript
- Generation of the figures (besides Fig. 4 and 5)
- Synthesis of the precursor material by the polyol method
- Conduction of SEM, FTIR and X-ray diffraction measurements as well as their evaluation and interpretation including Rietveld refinements
- I was partly involved in the interpretation of ^{57}Fe Mössbauer parameters (literature review)

I was not involved in:

- Conduction of ^{57}Fe Mössbauer measurements and evaluation of hyperfine parameters from the spectra
- Generation of figures 4 and 5
- Synthesis of the hydrothermal sample and sample used for the ^{57}Fe Mössbauer measurements

The work presented in **chapter 4** was previously *submitted for publication* Kirsch, A., Murshed, M. M., Kirkham, M. J., Huq, A., Litterst, F. J., Gesing, Th. M. Temperature-dependent structural and spectroscopic studies of $(Bi_{1-x}Fe_x)FeO_3$. *J Phys Chem C.* **2018,** *submitted for publication.*

I conducted the following tasks:

- Writing of the main manuscript
  - Chapter 3.2. *Neutron powder diffraction* partly written by Dr. Murshed
  - Chapter 3.3. *Spectroscopy Mössbauer* partly written by Prof. Litterst
- Generation of the figures (besides Fig. 6, 7 and 8 (*left panel*))
- Development of synthesis parameters
- Conduction of Raman and *in-house* XRD measurements including Rietveld refinements (also on synchrotron data) and evaluation of the data
- Simulations of XRD patterns
- Calculations of structural parameters from refined neutron data (e.g. Wang-Liebau eccentricity parameters, mean quadratic elongations, bond lengths and angles)
- Interpretation of SQUID and ^{57}Fe Mössbauer results

I was not involved in:

- Synthesis of the samples (done by trainee Jasmin Richter under my supervision)
- Conduction of SQUID, ^{57}Fe Mössbauer, synchrotron XRD, neutron scattering experiments with subsequent Rietveld refinements
- DEA modelling

- Writing of the chapter 3.4. *DEA Modelling*, 4 *Conclusion* and *Abstract*

The work presented in **chapter 5** was previously *published* Kirsch, A., Murshed, M. M., Schowalter, M., Rosenauer, A., Gesing, Th. M.; Nanoparticle Precursor into Polycrystalline $Bi_2Fe_4O_9$: An Evolutionary Investigation of Structural, Morphological, Optical, and Vibrational Properties. *J Phys Chem C* **2016**, *120,* 18831−18840.

I conducted the following tasks:

- Development of essential concept of the paper
- Writing of the main manuscript
- Generation of the figures (besides Fig. 1)
- Synthesis of the samples
- Conduction of SEM, FTIR, Raman, diffuse UV/Vis and XRD measurements as well as their evaluation and interpretation including Rietveld refinements
- Evaluation of HRTEM micrographs and their interpretation

I was not involved in:

- The conduction of TEM measurements (only attendance)

The work presented in **chapter 6** is a manuscript previously *submitted for publication* Kirsch, A.; Murshed, M. M.; Litterst, F. J.; Gesing, T. M. Structural, spectroscopic and thermoanalytic studies on $Bi_2Fe_4O_9$: tunable properties driven by nano- and poly-crystalline states *J. Phys. Chem. C* **2018***, submitted for publication.*

I conducted the following tasks:

- Development of essential concept of the paper and synthesis procedure
- Writing of the main manuscript
- Generation of the figures
- Conduction of DSC, FTIR, Raman, diffuse UV/Vis and XRD measurements as well as their evaluation and interpretation including Rietveld refinements
- Calculations of structural parameters from refined XRD data (rotation angles, mean quadratic elongations and bond angle variances)
- Evaluation of HRTEM micrographs and their interpretation

I was not involved in:

- Synthesis of the samples (done by trainee Jannis Diekmann under my supervision)
- Conduction of TEM (only attendance)
- Conduction of ^{57}Fe Mössbauer measurements and evaluation of hyperfine parameters from the spectra

The work presented in **chapter 7** was previously *published* Curti, M., Kirsch, A., Granone, L. I., Tarasi, F., López Robledo, G., Bahnemann, D.W., Murshed, M. M., Gesing, Th. M., Mendive C.B. Visible-light photocatalysis with mullite-type $Bi_2(Al_{1-x}Fe_x)_4O_9$: Striking the balance between bandgap narrowing and conduction band lowering. *ACS Catal.* **2018**, *8*, 8844−8855.

I conducted the following tasks:

- Synthesis of the samples
- Conduction of SEM (powder samples), diffuse UV/Vis and XRD measurements including Rietveld refinements
- Generation of the figure S1
- Main contribution to the writing of chapter 3.1 *Rietveld Refinement of XRD Measurements*

Manuscript *in preparation* Curti, M., Mendive, C.B., Kirsch, A., Granone, L. I., Arana, A., López Robledo, G., Murshed, M. M., Gesing, Th. M., Gesing Solvent effect in the visible-light photocatalytic degradation of phenol with mullite-type $Bi_2Fe_4O_9$, *manuscript in preparation.*

I conducted the following tasks:

- Synthesis of the polyol sample
- Conduction of SEM, diffuse UV/Vis and XRD measurements including Rietveld refinements

Chapter 3

$Bi_2Fe_4O_9$: Structural changes from nano- to micro-crystalline state

A published paper reprinted with permission from Kirsch, A., Murshed, M. M., Gaczynski, P., Becker, K.-D., $Bi_2Fe_4O_9$: Structural changes from nano- to micro-crystalline state. In: *Z. Naturforsch. B* **2016**, *71*, 447-455. Copyright (2016) De Gruyter. https://www.degruyter.com/view/j/znb.2016.71.issue-5/znb-2015-0227/znb-2015-0227.xml

Andrea Kirsch[a], M. Mangir Murshed[a], Piotr Gaczynski[b], Klaus-Dieter Becker[b], Thorsten M. Gesing[a]*

[a]Chemische Kristallographie fester Stoffe, Institut für anorganische Chemie und Kristallographie, FB2, Leobener Straße /NW2 und MAPEX Center for Materials and Processes, Bibliothekstraße 1, Universität Bremen, D-28359 Bremen, Germany

[b]Institut für Physikalische und Theoretische Chemie, Technische Universität Braunschweig, Braunschweig, D-38106, Germany

Dedicated to Prof. Dr. W. Jeitschko on the occasion of his 80th birthday.

*Corresponding author; e-mail address: gesing@uni-bremen.de; phone: +49 (0)421 218 63140; fax: +49 (0)421 218 63145

Abstract: $Bi_2Fe_4O_9$ was synthesized using a polyol-mediated method. X-ray powder diffraction (XRD) revealed that the as-synthesized sample is nano-crystalline. During heating, the X-ray amorphous powder transformed into a rhombohedral perovskite-type bismuth ferrate followed by a second transformation into mullite-type $Bi_2Fe_4O_9$ at higher temperatures. This transformation was studied at *in-situ* conditions by temperature-dependent XRPD and ^{57}Fe Mössbauer spectroscopy. The ^{57}Fe Mössbauer spectra indicate the existence of two Fe^{3+} species at two different octahedrally coordinated sites leading to the conclusion that the as-synthesized powder of the polyol synthesis possesses a disordered $(Bi_{1-x}Fe_x)FeO_3$ perovskite structure. Rietveld refinements have unambiguously supported this observation and this results suggest that one third of the Bi^{3+} sites are substituted by Fe^{3+} representing the initial chemical composition. This study has shown that as-synthesized nano-materials are not always similar to the respective micro-crystalline ones.

Keywords: crystal structure, nano-material, ^{57}Fe Mössbauer spectroscopy, X-ray powder diffraction

1. Introduction

Bismuth ferrates, $BiFeO_3$ and $Bi_2Fe_4O_9$, have attracted great attention due to their electronic [1], optic [2], catalytic [3], and magnetic [4] properties making them suitable for advanced applications like photocatalysis [5, 6], photovoltaics [7, 8], and spintronics [9]. $Bi_2Fe_4O_9$ is mainly studied as a gas sensor [10] and as a photocatalytically [11] active material. It also shows multiferroic properties near room-temperature [12], interesting crystal chemistry [13 - 16] and temperature-dependent behavior [17] due to the stereochemically active Bi^{3+} $6s^2$ lone electron pairs (LEPs) [18]. $Bi_2Fe_4O_9$ crystallizes in the orthorhombic space group *Pbam* with $Z = 2$ and possesses a mullite-type structure [14] featuring the typical chains of edge-sharing FeO_6 octahedra parallel to the *c*-axis. The chains are cross-linked by corner-sharing Fe_2O_7 double-tetrahedra. The Bi atoms are located between the chains and their LEPs point toward the vacant sites of the channels [17, 18]. In the $Bi_2O_3 – Fe_2O_3$ quasi-binary phase field co-crystallization of $Bi_2Fe_4O_9$ and $BiFeO_3$ is frequently observed [19 - 21].

$BiFeO_3$ is mostly studied owing to its multiferroic properties at room-temperature and photocatalytic activity in the visible range of light [5, 22]. The widely studied $BiFeO_3$

has a Néel temperature of ~ 640 K and a Curie temperature of ~ 1100 K [23]. The crystal structure of $BiFeO_3$ as given in Figure 1 can be described in the space group *R*3c (Z = 2) as a rhombohedrally distorted perovskite. The tilting of the FeO_6 octahedra around the pseudo-cubic threefold <111> axis is a characteristic structural feature. The displacement of the Bi^{3+} and Fe^{3+} cations along this axis causes spontaneous polarization [24]. From the distorted 6-fold coordination of the Bi atoms with oxygen a stereochemical activity of the LEP can be assumed.

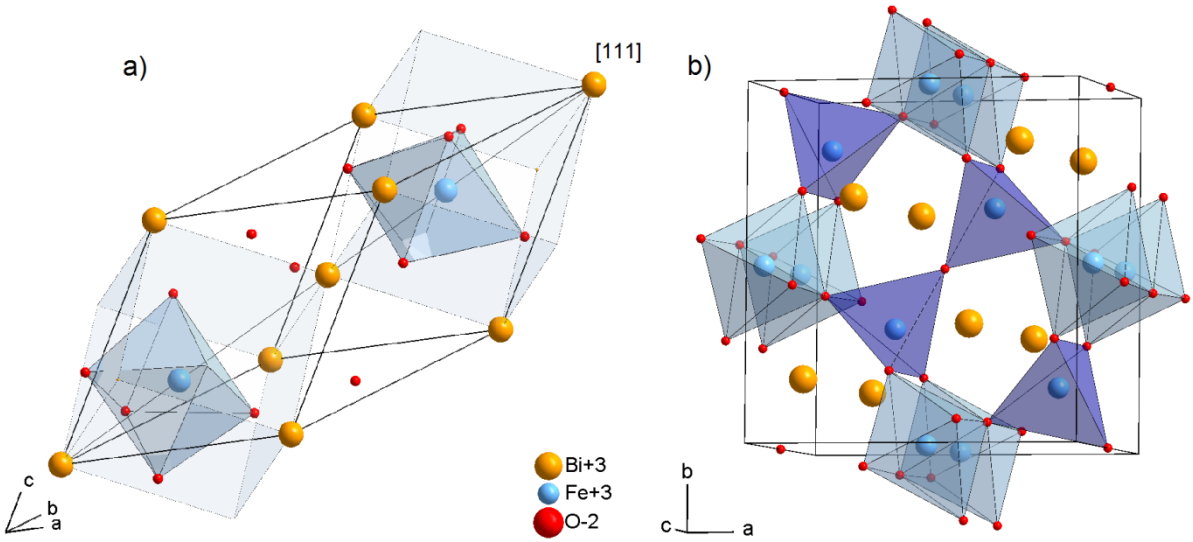

Figure 1. Crystal structures of perovskite-type $BiFeO_3$ in space group *R*3c (a) and of mullite-type $Bi_2Fe_4O_9$ in space group *Pbam* (b).

Zhang et al. [2] demonstrated that small crystallites of $Bi_2Fe_4O_9$ exhibit higher photocatalytic activity. Therefore the synthesis and characterizations of this compound as nano-material up to ~30 nm is of special interest for improved photocatalytic efficiency. $Bi_2Fe_4O_9$ was synthesized through a variety of synthesis methods including conventional solid state reaction [25], chemical co-precipitation [1], sol-gel [19] and EDTA routes [20], the glycerine method [13], and hydrothermal processes [26]. In this context, the polyol method [27, 28] provides a cost effective and easy method for the preparation of larger quantities of nano-crystalline samples. In the present study, a precursor was synthesized by the polyol method and characterized by Fourier transform infrared (FTIR) spectroscopy. The transformation of the perovskite-type (ABX_3) to the mullite-type ($A_2B_4X_9$) compound was studied via *in-situ* temperature-dependent powder X-ray diffraction (PXRD) and ^{57}Fe Mössbauer spectroscopy.

2. Experimental

2.1. Synthesis

Samples were prepared by a polyol-mediated synthesis. In detail, 5 mmol $Bi(NO_3)_3 \cdot 5H_2O$ (Sigma-Aldrich, ≥ 98%), 10 mmol $Fe(NO_3)_3 \cdot 9H_2O$ (Sigma-Aldrich, ≥ 98%) and 40 mmol NaOH (VWR Chemicals, 99.2%) were dissolved in 42 ml diethylene glycol (DEG) (AppliChem, 99%). The mixture was heated in a three-necked flask under reflux using a metal bath at 423 K. After 2 hours 5 mmol stearic acid was added. After cooling down to ambient conditions, the solid product was separated by centrifugation and washed several times with acetone with intermediate centrifugation steps. For comparison samples were also synthesized hydrothermally at 473 K for 24 h in Teflon coated steel autoclaves. Two series of samples were produced. First the molar ratio of $Bi(NO_3)_3 \cdot 5H_2O$ to $Fe(NO_3)_3 \cdot 9H_2O$ was varied from 1 : 2 to 2 : 2 in steps of 0.2 using always 10 mmol $Fe(NO_3)_3 \cdot 9H_2O$ in 20 mL of a 2 mol/L NaOH solution. Thereafter a molar 1 : 1 ratio was used increasing the NaOH concentration up to 12 mol/L in steps of 2 mol/L. After the heat treatment the samples where intensively washed with deionized water. This process was repeated three times before the samples were dried at 393 K for about 12 h.

2.2. Spectroscopy

The FTIR spectra were measured on a Bruker IFS 66v/S spectrometer using the standard KBr method (1 mg sample in 200 mg KBr) between 370 and 4000 cm^{-1}. Background as well as sample spectra were obtained from 128 scans each with a spectral resolution of ca. 1 cm^{-1}. The mode positions were determined by taking the point of the maximum intensity. The temperature-dependent ^{57}Fe Mössbauer spectra were taken between 293 and 973 K in an atmosphere of flowing synthetic air using a standard transmission Mössbauer spectrometer (Halder) in the sinusoidal driving mode employing a ^{57}Co/Rh γ-radiation source with a maximum activity of 1.91 GBq. The velocity scale was calibrated with an α-Fe absorber at room-temperature and the isomer shifts (IS) are stated relative to the center of this calibration.

2.3. X-ray diffraction

X-ray powder diffraction data were collected on a X'Pert MPD PRO diffraction system (PANalytical GmbH, Almelo, The Netherlands) equipped with Ni-filtered $CuK_{\alpha 1,2}$

radiation ($\lambda_{\alpha 1,2}$ = 0.15406 nm, 0.15444 nm), a 0.25° divergence slit, a 0.5° antiscatter slit, a 0.04 rad soller slit in the primary beam and a X'Celerator detector system in the secondary beam in Bragg-Brentano geometry. Room-temperature data were measured between 5 and 85° 2θ with a step width of 0.0167° 2θ and a measurement time of 20 s per step. An HTK 1200N heating chamber (Anton Paar, Graz, Austria) was used for temperature-dependent measurements. Data were collected from 5 to 100° 2θ with a step width of 0.0167° 2θ and a measurement time of 75 s per step. The temperature was increased stepwise from 300 to 1120 K in 20 K steps with an equilibration time of 5 minutes. The obtained data were refined using the Rietveld method (TOPAS V4.2, Bruker AXS, Karlsruhe, Germany). For the profile description the fundamental parameter approach was used, where the fundamental parameters were fitted against a LaB_6 standard material.

2.4. Scanning Electron Microscopy

Scanning electron microscopy (SEM) was carried out on a JSM-6510 (JEOL GmbH, Munich, Germany) equipped with energy dispersive X-ray (EDX) analysis facilities and an XFlash Detector 410-M (Bruker AXS GmbH, Karlsruhe, Germany). To obtain quality data the samples were sputtered with a thin film of gold having a thickness of approx. 10 nm. EDX spectra were collected using an excitation voltage of 20 kV.

3. Results and Discussion

3.1. Synthesis

The synthesis of $Bi_2Fe_4O_9$ using the hydrothermal method was described by Wang *et al.* [29]; the process strongly depends on the hydroxide concentration during the heat treatment at 373 K. The authors used a multi-step synthesis in which the metal nitrates were first dissolved in nitric acid, which was then brought, by adding slowly dropwise a KOH solution, to a pH = 8 leading to a precipitation of a brown solid. This solid was filtered, washed and transferred into a NaOH solution which was then treated hydrothermally. With a NaOH concentration of 2 mol/L they observed the formation of a perovskite phase. Note that the authors [29] took this as the beginning of the crystallization of $Bi_2Fe_4O_9$, but from the reported diffraction pattern the formation of a perovskite is obvious. With increasing concentration the mullite-type phase was formed. To make the synthesis easier, we simply added the metal nitrates

to an aqueous NaOH solution and kept it at 473 K for 24 hours. For a first experiment a 2 mol/L NaOH solution with a Bi to Fe ratio of 1.2 : 2 was used to form the $Bi_2Fe_4O_9$ mullite-type phase. Rietveld refinements of XRPD data confirmed that the product consists of 67 wt% $BiFeO_3$, 24 wt% Fe_2O_3 and 9 wt% $Bi_2Fe_4O_9$. However, using a ratio of 1.4 : 2 as much as 93 wt% $Bi_2Fe_4O_9$ was formed together with 7 wt% $BiFeO_3$. A further increase of the molar ratio to 1.6 : 2 and 1.8 : 2 leads to pure well crystallized $Bi_2Fe_4O_9$ phases as shown in Figure 2. The latter sample was used for further investigations. Increasing the cation ratio further to 1 : 1 and increasing the NaOH concentration at this ratio to 6, 9 or 12 mol/L leads to an increase of the average crystallite size, however, along with the formation of a few percent of the sillenite phase $Bi_{25}FeO_{39}$ [30].

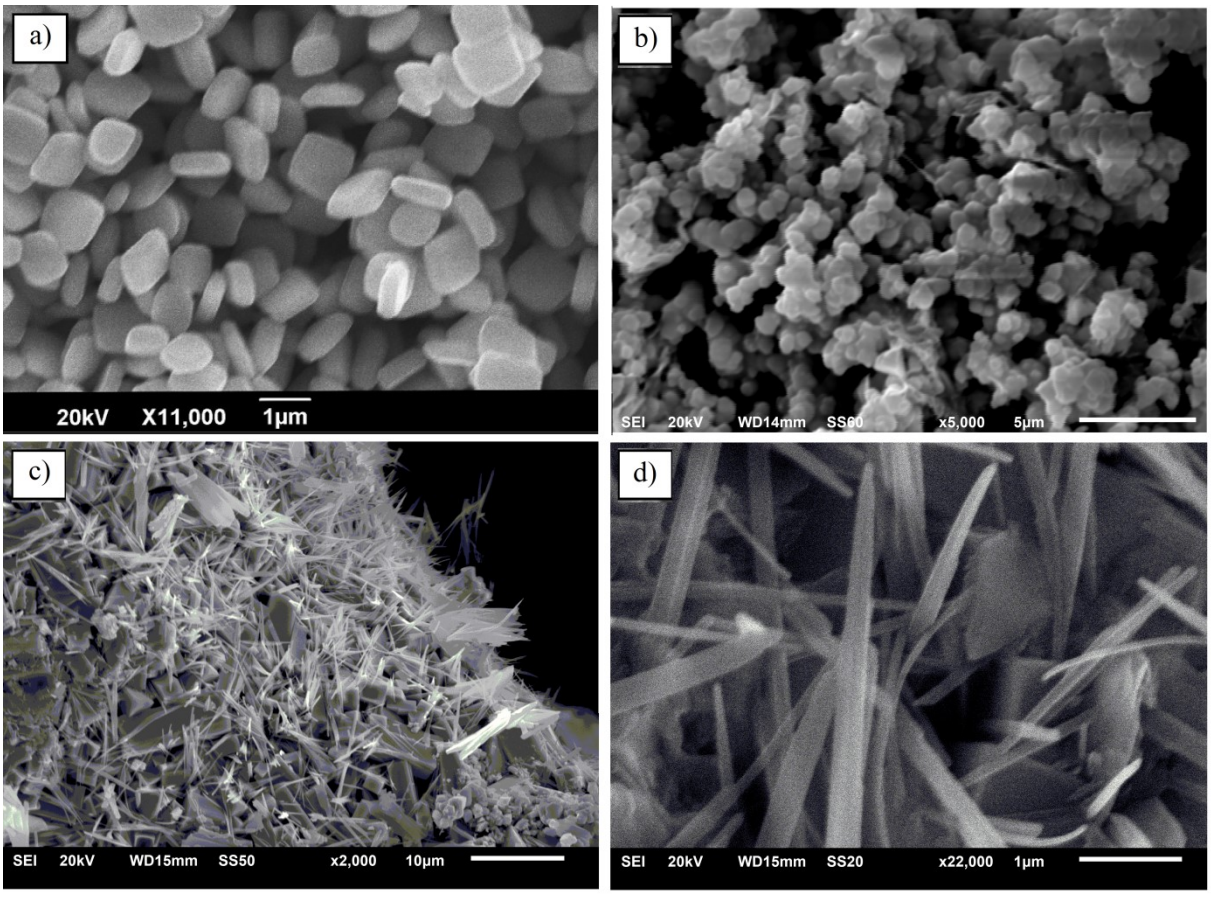

Figure 2. Scanning electron micrographs of $Bi_2Fe_4O_9$ synthesized by the hydrothermal method (a), by the polyol method (b) and the polyol sample obtained after the XRD heating measurements, showing $Bi_2Fe_4O_9$ rods and needles (c & d).

The synthesis of nanoscale metal oxides using the polyol method was described by several authors [28, 31, 32]. The metal precursors were heated in a high-boiling

alcohol such as most commonly used diethylene glycol (DEG) [31], ethylene glycol [22], triethylene glycol [33] and tetraethylene glycol [33] at elevated temperatures. Using this method various metal oxides can be produced showing particle sizes below ~100 nm [31, 33, 34]. However, to produce a crystalline sample a subsequent heat treatment is often required [19, 31, 35]. In this study, metal nitrates were chosen as metal precursors. They were dissolved in DEG in a three-necked flask followed by addition of 40 mmol NaOH. The temperature of the mixture was then ramped to the target reflux temperature of 423 K, concomitantly releasing NO_x gases and forming a brown precipitate at 388 K. Notably, the reflux (423 K) started far below the boiling point of DEG (519 K) owing to the high content of hydrate water in the metal nitrates. The as-synthesized particles are spherical in shape and possess a size distribution ranging from 200 nm – 700 nm as shown by SEM micrograph analysis (Figure 2). X-ray powder diffraction gave no clear Bragg reflections. However, well crystalline mullite-type $Bi_2Fe_4O_9$ could be produced via a subsequent heat treatment. Whereas the hydrothermal synthesis nicely produced crystalline mullite-type material the structure of the polyol synthesized material could hardly be characterized due to the very small average crystallite size leading to very broad diffraction reflections as for an X-ray amorphous material.

3.1. Spectroscopy

Infrared spectroscopy

The infrared spectrum of the hydrothermally synthesized sample corresponds to that reported earlier for $Bi_2Fe_4O_9$ [36], whereas numerous different absorption bands are visible in the FTIR spectrum of the $Bi_2Fe_4O_9$ nano-material synthesized by the polyol method as shown in Figure 3. Most of them are resulting from the (mainly organic) compounds used in the synthesis. The broad absorption bands at 3200 and 1650 cm^{-1} can be assigned to water in the sample [37]. The NO_3^- anions are evidenced by the sharp absorption feature at 1385 cm^{-1}. The C-H stretching bands of stearic acid are represented by modes between 2850 and 2920 cm^{-1} [38], whereas the respective carboxyl groups could be identified by their modes at 1670 cm^{-1}. Remaining DEG (after washing the samples with acetone) leads to the observation of C-O-C, C-OH and C-O vibrations with peak maxima at 1125(3), 1060(3) and 900(3) cm^{-1}, respectively [39]. Octahedral Fe-O stretching vibrations in bismuth ferrates are located in the region between 445 and 548 cm^{-1} ($BiFeO_3$ [40]) and

between 437 and 471 cm^{-1} ($Bi_2Fe_4O_9$ [36]). The appearance of absorption peaks around 500 cm^{-1} of the $Bi_2Fe_4O_9$ nano-material could therefore be assigned to the Fe-O stretching of FeO_6 octahedra. The assignments of the band positions of the vibrational modes of the hydrothermally synthesized mullite-type phase (Figure 3) agree well with those of Voll *et al.* [36]. In the spectrum of this sample an additional strong mode with the maximum intensity at 812(1) cm^{-1} belongs to the Fe-O-Fe stretching mode of the Fe_2O_7 double tetrahedral unit interconnecting the octahedral chains (as calculated for the isotypic aluminum compound [41]), which is absent in the polyol $Bi_2Fe_4O_9$ nano-material material.

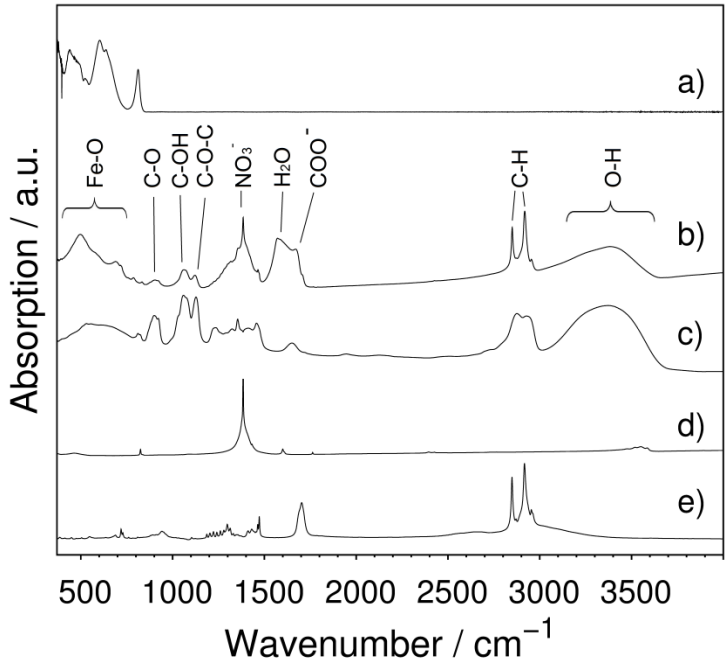

Figure 3. Infrared spectra of $Bi_2Fe_4O_9$ synthesized by the hydrothermal method (a) and precursor formed by the polyol method (b), diethylene glycol (DEG) (c), $Bi(NO_3)_3{\cdot}5H_2O$ (d), and stearic acid (e).

^{57}Fe Mössbauer spectroscopy

To get more insight into the coordination of the iron atoms in the synthesized samples, ^{57}Fe Mössbauer data were collected at different temperatures. The fit of the room-temperature ^{57}Fe Mössbauer spectrum of the polyol-synthesized sample (only polyol from now on) reveals the existence of two Fe^{3+} species in two different octahedrally coordinated sites, Table 1. The majority component shows exactly the same isomer shift (IS) as the octahedrally coordinated Fe-site in $Bi_2Fe_4O_9$ [15]; thus identical coordination and similar bond lengths are expected. The minority

component shows a slightly higher IS, indicating a lower electron charge density at the nucleus, pointing to slightly larger bond lengths. The quadrupole splitting (QS) of the two octahedrally coordinated Fe-sites in the polyol material is significantly larger than that of the octahedrally coordinated site in $Bi_2Fe_4O_9$ [15]. In this context, it is interesting to compare the present results with those of nano-crystalline $BiFeO_3$. Park *et al.* [4] have studied the Mössbauer spectra of $BiFeO_3$ perovskites with crystallite sizes between <14 nm and about 100 nm. The present Mössbauer spectroscopic parameters exhibit some similarity with those of the sample with <14 nm (Table 1), for example in respect to the relative signal area, indicating a similar distribution of iron over two inequivalent sites in the structure. As seen, also quadrupolar interactions take similarly large values indicating significant coordinative distortion in both materials. However, IS values of the nano-perovskite are significantly lower, indicating a higher electron charge density at the nucleus than in the polyol material. The large room-temperature linewidth (Γ = 0.4 mm s^{-1}, Table 1) of the polyol material provides evidence of some kind of disorder around the two Fe-occupied sites. In conclusion, the polyol material appears to be of disordered nature and to possess an unknown local structure with two non-equivalent octahedral sites for Fe^{3+} occurring in an approximate 1 : 3 ratio. According to these signal intensities the material could, for instance, represent a $(Bi_2Fe)Fe_3O_9$ perovskite.

Table 1: Hyperfine parameters of room-temperature ^{57}Fe Mössbauer spectra of $Bi_2Fe_4O_9$ powder prepared by the polyol method, as compared to $Bi_2Fe_4O_9$ synthesized by the glycerine method [15] and to bulk and nano $BiFeO_3$ [4].

Sample	IS 1 / mm s^{-1}	QS 1 / mm s^{-1}	A 1 / %	IS 2 / mm s^{-1}	QS 2 / mm s^{-1}	A 2 / %	Γ / mm s^{-1}
polyol	0.38(1)	1.09(1)	27(1)	0.36(1)	0.70(1)	73(1)	0.40(1)
hydrothermal	0.24(1)	0.95(1)	29(1)	0.36(1)	0.38(1)	29(1)	0.25(1)
$Bi_2Fe_4O_9$ [15]	0.23(1)	0.95(1)	50(1)	0.35(1)	0.37(1)	50(1)	0.22(1)
$BiFeO_3$ [4] bulk	0.39(3)	-0.10(5)*	47(2)	0.38(3)	0.34(5)*	53(2)	0.35(2)
$BiFeO_3$ [4] <14 nm	0.31(3)	1.29(5)	25(2)	0.33(3)	0.79(5)	73(2)	0.23(2)

*Data from the magnetic bulk material represent the quadrupolar perturbation parameter $\varepsilon = QS \cdot (3\cos^2\theta - 1)/2$, where θ is the angle between the direction of the principal component of the electric field gradient and the direction of the local magnetic field.

Temperature-dependent Mössbauer spectra of the hydrothermal and polyol samples are shown in Figure 4. Whereas the thermal evolution of the ^{57}Fe hyperfine

parameters in $Bi_2Fe_4O_9$ prepared by the hydrothermal method is exactly the same as reported for bulk $Bi_2Fe_4O_9$ [15], the parameters for the polyol sample show a different behavior. During heating the spectral features change between 573 and 773 K, showing evidence for structural changes leading to the appearance of two differently coordinated iron sites. The two sites of octahedral coordination of Fe^{3+} in $(Bi_2Fe)Fe_3O_9$ transform into one tetrahedral and one octahedral site. Finally, at 973 K the spectrum is identical to that of $Bi_2Fe_4O_9$ prepared by the hydrothermal method. The temperature dependence of isomer shifts (IS) and quadrupole splittings (QS) of $Bi_2Fe_4O_9$ prepared by the polyol method is presented in Figure 5.

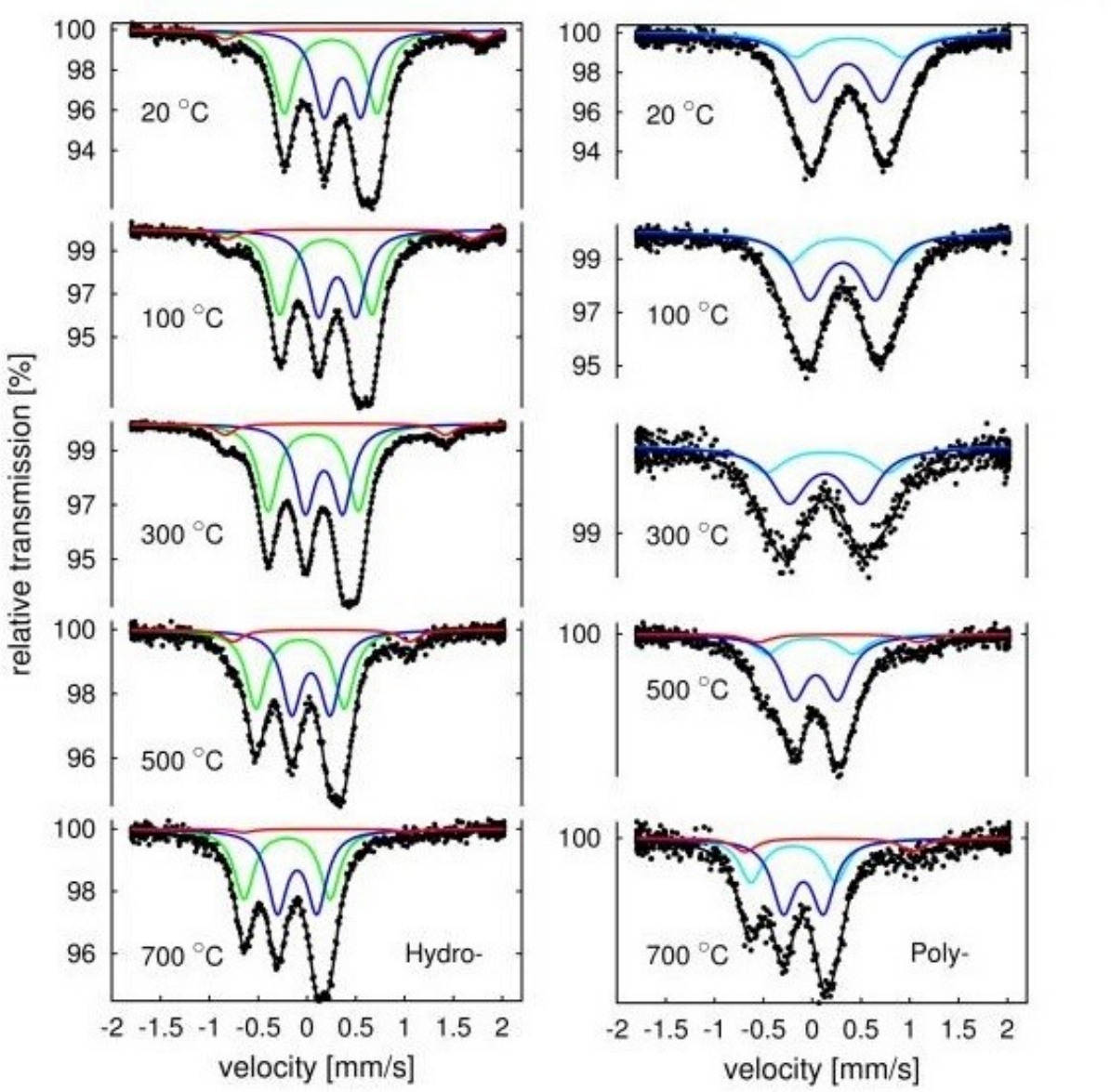

Figure 4. Temperature-dependent ^{57}Fe Mössbauer spectra of $Bi_2Fe_4O_9$ powder materials prepared by the polyol (right) and hydrothermal method (left) in flowing synthetic air. The subspectrum shown in red is attributed to a small admixture of Fe_2O_3.

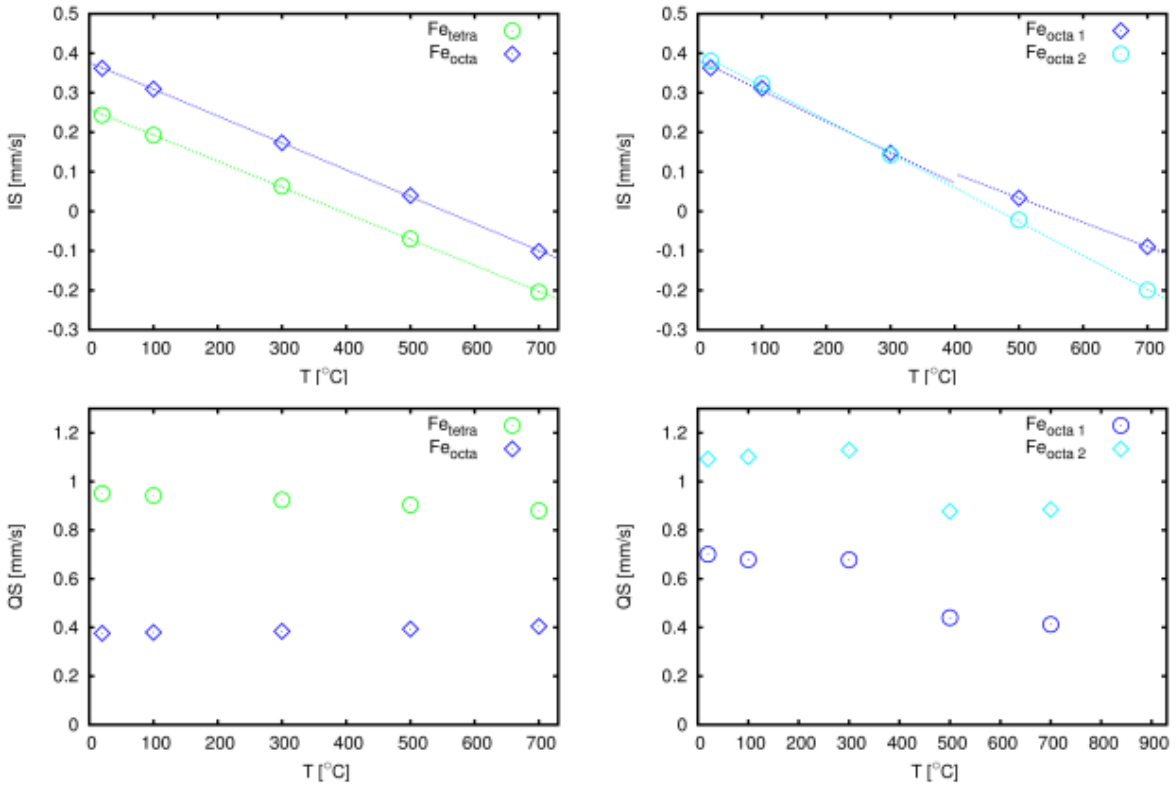

Figure 5: Temperature-dependent isomer shifts (IS) and quadrupole splittings (QS) of $Bi_2Fe_4O_9$ prepared by the hydrothermal (left) and polyol method (right)**.**

3.2. Temperature-dependent X-ray powder diffraction

The *in-situ* heating XRPD experiment of the as-synthesized polyol material showed a transformation from an X-ray amorphous powder into a rhombohedral perovskite-type structure at 680 K followed by a second transformation into $Bi_2Fe_4O_9$ starting from 800 K on as shown in Figure 6. Above 920 K the perovskite-structure cannot be detected anymore. The sharp reflections which appear at diffraction angles greater than 57° 2θ above 620 K are attributed to the sample holder due to mechanical shrinking of the powder sample.

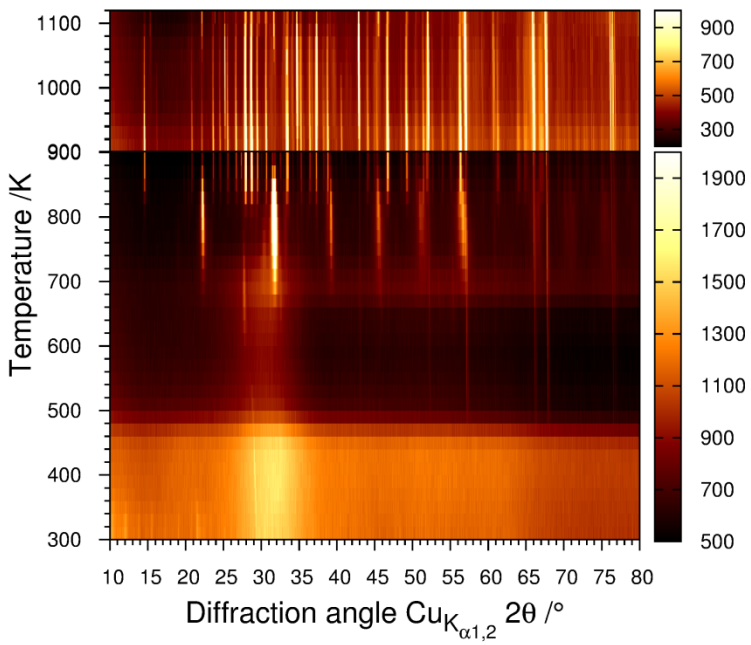

Figure 6: Temperature-dependent diffraction patterns of the polyol material showing the transformation from as-synthesized amorphous powder into rhombohedral $BiFeO_3$ and orthorhombic $Bi_2Fe_4O_9$ (different scale range above 900 K for better visibility).

Rietveld refinements of the temperature-dependent data of the polyol material were carried out using the structure model of Moreau et al. [42] for $BiFeO_3$ with *R*3c symmetry and lattice parameters of *a* = 558.76(3) pm and *c* = 1386.7(1) pm in the hexagonal setting. Taking the results of the ^{57}Fe Mössbauer study into account, Fe^{3+} and Bi^{3+} were both refined on the same 6*a* position (0, 0, 0(fixed)) whereas the second 6*a* position (0, 0, 0.2215(18) at 780 K) was taken as solely occupied by iron ions. The oxygen atoms were found on the 18*b* position (0.421(11), 0.011(8), 0.952(5) at 780 K). With increasing temperature the $(Bi_{1-x}Fe_x)FeO_3$ crystal structure was observed to be rapidly changing as depicted in Figure 7. The lattice parameter *a* increases from 561.4(4) pm (at 740 K) to 562.0(2) pm at 780 K and then decreases to 561.62(6) pm at 860 K as shown in Figure 8. The lattice parameter *c* of $(Bi_{1-x}Fe_x)FeO_3$ is significantly smaller than the one reported for $BiFeO_3$ [42], supporting the site co-shared by Fe^{3+} and Bi^{3+}. Accordingly, the shrinking of the lattice parameter can be explained in terms of the smaller ionic radius of Fe^{3+} [43]. Starting from 740 K, the lattice parameter *c* increases linearly with temperature from 1375(2) pm and approaches the value reported for $BiFeO_3$ [42] at about 800 K (*c* = 1383(1) pm). Notably, this is the temperature at which the lattice parameter *a* as well as the strain, as shown in Figure 9, decrease rapidly. The unit cell volume increases linearly with

temperature. At 860 K, reflections appear (marked with crosses in Figure 7) that can be attributed to Fe-bearing sillenite $Bi_{25}FeO_{39}$ in space group *I*23 [30]. Above 920 K, neither reflections of sillenite nor of the perovskite structure can be detected.

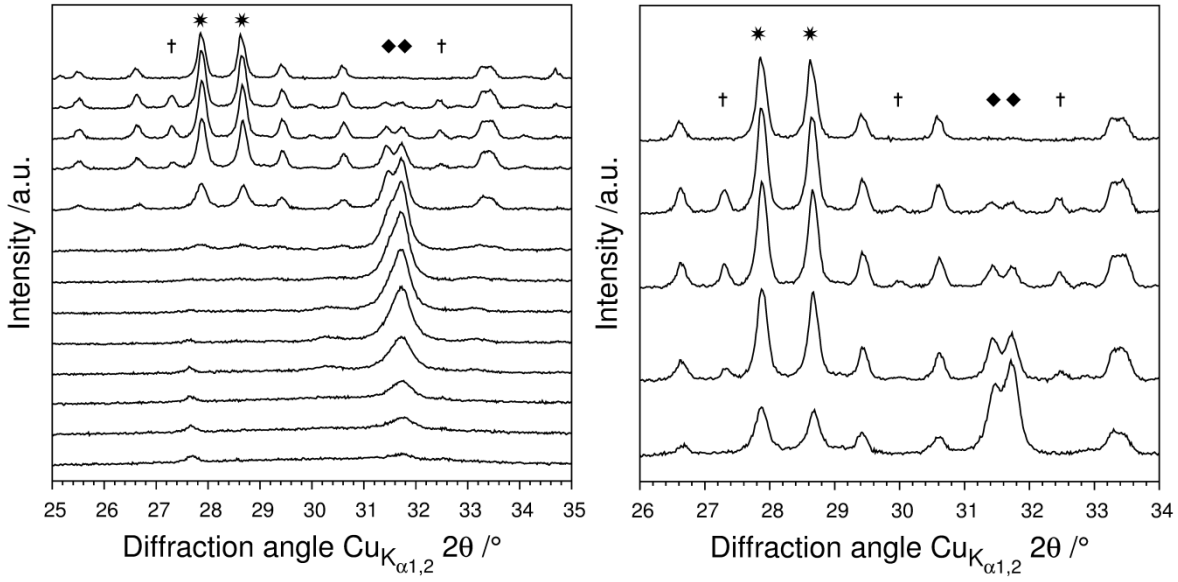

Figure 7. left panel: Temperature-dependent XRPD patterns from 680 to 920 K in 20 K steps showing the evolution of $(Bi_{1-x}Fe_x)FeO_3$ and $Bi_2Fe_4O_9$ phases. Some intense reflections of the $BiFeO_3$ (104) (110) and $Bi_2Fe_4O_9$ phase (121) (211) are indicated by diamonds and stars, respectively. Reflections marked by a cross can be attributed to $Bi_{25}FeO_{39}$. Right panel: Magnified feature of a part of the left panel, showing the appearance and disappearance of reflections marked by the cross.

Substitution of Fe^{3+} with an effective ionic radius of 64.5 pm [43] on the Bi position causes a high strain in the unit cell due to the much larger ionic radius of Bi^{3+} 103 pm [43]. The microstrain at 740 K could be refined to as much as 0.41(1)% giving further evidence that Bi^{3+} is partially substituted by Fe^{3+}. The micro-strain is reduced to about 0.09(1)% at 860 K. The Rietveld refinement results in an occupancy of 69(2)% for Bi3+ at 740 K, the rest is occupied by Fe^{3+} according to the constrained occupancy parameter refinements assuming a fully occupied position. This value fits well to the Mössbauer spectroscopic results, which have suggested 1/3 of the occupancy probability. With increasing temperature the amount of Bi^{3+} on the position is increasing (Figure 9).

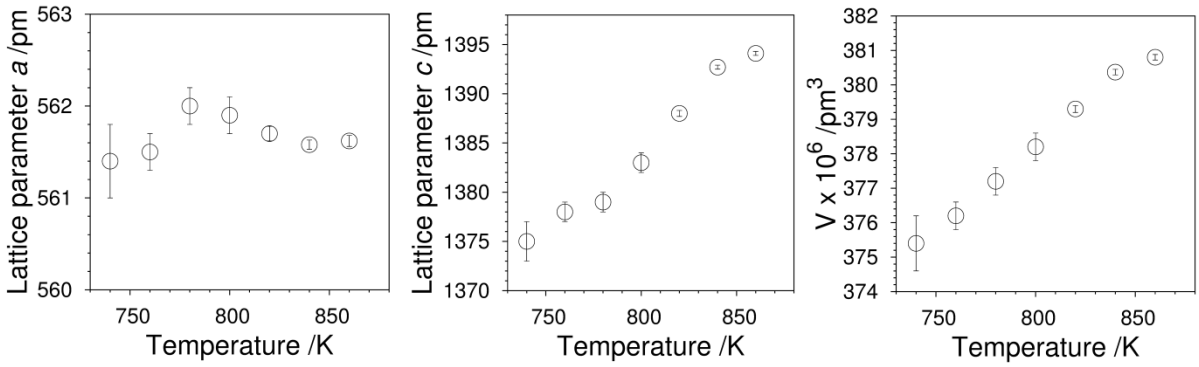

Figure 8: Temperature-dependent lattice parameter *a* (left), *c* (middle) and cell volume (right) of $(Bi_{1-x}Fe_x)FeO_3$.

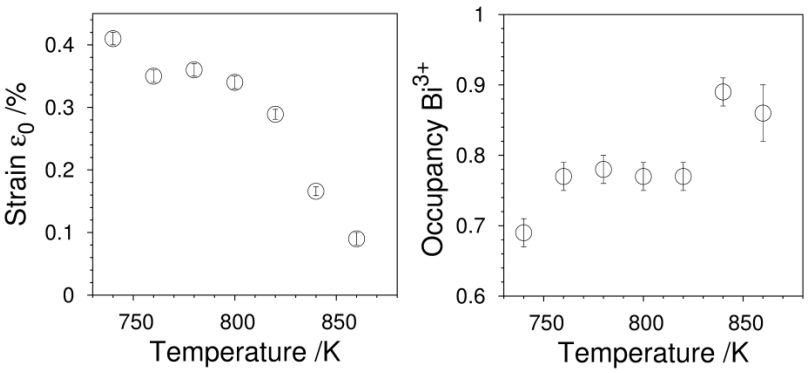

Figure 9: Temperature-dependent strain (left) and occupancy of Bi^{3+} (right) of the $(Bi_{1-x}Fe_x)FeO_3$ phase.

After completion of the temperature-dependent XRD experiments the samples were investigated by scanning electron microscopy. Needle-like rods and plates were identified as shown in the SEM micrograph of Figure 2. It is assumed that the long chains of the stearic acid present in the precursor caused the pronounced unidirectional growth. The sample contains larger crystals as well as very thin needle-like plates (Figure 2). The length of the thin needles ranges from 5 – 10 µm, the width takes values of about 250 nm. Due to their transparency in SEM micrographs these needles are assumed to be only a few nm thick. EDX analyses revealed a molar ratio of Bi : Fe of 1 : 2.1(2) as expected for $Bi_2Fe_4O_9$. Nevertheless, a remaining content of 3.3(3) mol% Na was found, but we assume, based on the substitution experience with this structure-type (e.g. [44]), that sodium is not incorporated in the mullite-type structure.

4. Conclusion

$Bi_2Fe_4O_9$ was synthesized by a polyol-mediated synthesis. It is assumed that the growth along the chains of stearic acid present in the precursor material leads to needle-like rods and plates during heating experiments. Because smaller dimensions of $Bi_2Fe_4O_9$ crystals show higher photocatalytically activity [2], such few nm thick plates would be useful as photocatalytic active material. The comparative temperature-dependent ^{57}Fe Mössbauer spectroscopic study demonstrated that the sample synthesized by the polyol method is of different nature than the sample synthesized by the hydrothermal route. During temperature-dependent studies, the polyol material gradually approached the features of the hydrothermal sample. In addition, the transformation of the as-synthesized amorphous polyol sample into rhombohedral $(Bi_{1-x}Fe_x)FeO_3$ perovskite and subsequent transformation into the orthorhombic $Bi_2Fe_4O_9$ mullite-type structure was confirmed by temperature-dependent X-ray diffraction data analysis showing that the chemical composition of the educts with respect to the metal atoms is conserved during the double reconstructive phase transition process. Mössbauer spectroscopic results as well as Rietveld refinements of temperature-dependent powder X-ray diffraction data suggest that about one third of the octahedral Bi^{3+} sites in the $(Bi_{1-x}Fe_x)FeO_3$ perovskite is substituted by Fe^{3+} leading to high strain in the system and a smaller lattice parameter *c*. Moreover, temperature-dependent Mössbauer spectroscopic and X-ray diffraction investigations have shown that nano-crystalline $Bi_2Fe_4O_9$ (Bi_2O_3*$2Fe_2O_3$) transforms via the $(Bi_2Fe)Fe_3O_9$ perovskite ($(Bi_{1-x}Fe_x)FeO_3$) to micro-crystalline mullite-type $Bi_2Fe_4O_9$, which clearly shows that a nano-crystalline product has to be proven for structural identity with its micro-crystalline appearance before stating the structural relation.

Acknowledgement

KDB thanks the State of Lower Saxony (Germany) and the Volkswagen-Foundation for financial support. TMG gratefully acknowledges the Deutsche Forschungsgemeinschaft (DFG) for the financial support in the Heisenberg program (GE1981/3-1 and GE1981/3-2) and the mullite-LEP project (GE1981/4-1 and GE1981/4-2). We also thank the unknown reviewer for his precise suggestions.

References

[1] Y. Li, Y. Zhang, W. Ye, J. Yu, C. Lu, L. Xia, *New J. Chem.* **2012**, *36*, 1297–1300.
[2] Q. Zhang, W. Gong, J. Wang, X. Ning, Z. Wang, X. Zhao, W. Ren, Z. Zhang, *J. Phys. Chem. C* **2011**, *115*, 25241–25246.
[3] N. I. Zakharchenko, *Kinet. Catal.* **2002**, *43*, 95–98.
[4] T. Park, G. C. Papaefthymiou, A. J. Viescas, A. R. Moodenbaugh, S. S. Wong, *Nano Lett.* **2007**, *7*, 766–772.
[5] F. Gao, X. Chen, K. Yin, S. Dong, Z. Ren, F. Yuan, T. Yu, Z. Zou, J. M. Liu, *Adv. Mater.* **2007**, *19*, 2889–2892.
[6] S. Sun, W. Wang, L. Zhang, M. Shang, *J. Phys. Chem. C* **2009**, *113*, 12826–12831.
[7] Y. Zang, D. Xie, X. Wu, Y. Chen, Y. Lin, M. Li, H. Tian, X. Li, Z. Li, H. Zhu, T. Ren, D. Plant, *Appl. Phys. Lett.* **2011**, *99*, 132904–1–3.
[8] Y. Zhang, Y. Guo, H. Duan, H. Li, L. Yang, P. Wang, C. Sun, B. Xu, H. Liu, *RSC Adv.* **2014**, *4*, 28209–28218.
[9] G. Catalan, J. F. Scott, *Adv. Mater.* **2009**, *21*, 2463–2485.
[10] A. S. Poghossian, H. V. Abovian, P. B. Avakian, S. H. Mkrtchian, V. M. Haroutunian, *Sensors Actuators B* **1991**, *4*, 545–549.
[11] Z. Liu, B. Wu, Y. Zhu, *Mater. Chem. Phys.* **2012**, *135*, 474–478.
[12] A. K. Singh, S. D. Kaushik, B. Kumar, P. K. Mishra, A. Venimadhav, V. Siriguri, S. Patnaik, *Appl. Phys. Lett.* **2008**, *92*, 132910–1–3.
[13] T. M. Gesing, R. X. Fischer, M. Burianek, M. Mühlberg, T. Debnath, C. H. Rüscher, J. Ottinger, J.-C. Buhl, H. Schneider, *J. Eur. Ceram. Soc.* **2011**, *31*, 3055–3062.
[14] H. Schneider, R. X. Fischer, T. M. Gesing, J. Schreuer, M. Mühlberg, *Int. J. Mater. Res.* **2012**, *103*, 422–429.
[15] S.-U. Weber, T. M. Gesing, J. Röder, F. J. Litterst, R. X. Fischer, K.-D. Becker, *Int. J. Mater. Res.* **2012**, *103*, 430–437.
[16] S. Weber, T. M. Gesing, G. Eckold, R. X. Fischer, F. J. Litterst, K.-D. Becker, *J. Phys. Chem. Solids* **2014**, *75*, 416–426.
[17] M. M. Murshed, G. Nénert, M. Burianek, L. Robben, M. Mühlberg, H. Schneider, R. X. Fischer, T. M. Gesing, *J. Solid State Chem.* **2013**, *197*, 370–378.
[18] M. Curti, T. M. Gesing, M. M. Murshed, T. Bredow, C. B. Mendive, *Z. Kristallogr.* **2013**, *228*, 629–634.
[19] X. Wang, M. Zhang, P. Tian, W. S. Chin, C. M. Zhang, *Appl. Surf. Sci.* **2014**, *321*, 144–149.
[20] J. Zhao, T. Liu, Y. Xu, Y. He, W. Chen, *Mater. Chem. Phys.* **2011**, *128*, 388–391.
[21] X. H. Wu, J. Miao, Y. Zhao, X. B. Meng, X. G. Xu, S. G. Wang, Y. Jiang, *Optoelectron. Adv. Mater. Rapid Commun.* **2013**, *7*, 116–120.
[22] X. Wang, Y. Lin, Z. C. Zhang, J. Y. Bian, *J. Sol-Gel Sci. Technol.* **2011**, *60*, 1–5.
[23] P. Fischer, M. Polomska, I. Sosnowska, M. Szymanski, *J. Phys. C* **1980**, *13*, 1931–1940.
[24] B. Ruette, S. Zvyagin, A. P. Pyatakov, A. Bush, J. F. Li, V. I. Belotelov, A. K. Zvezdin, D. Viehland, *Phys. Rev. B* **2004**, *69*, 064114–1–7.

[25] H. Koizumi, N. Niizeki, T. Ikeda, *Jpn. J. Appl. Phys.* **1964**, *3*, 495–496.
[26] Q.-J. Ruan, W.-D. Zhang, *J. Phys. Chem. C* **2009**, *113*, 4168–4173.
[27] F. Fievet, J. P. Lagier, M. Figlarz, *MRS Bull.* **1989**, *14*, 29–34.
[28] C. Feldmann, *Solid State Sci.* **2005**, *7*, 868–873.
[29] Y. Wang, G. Xu, L. Yang, Z. Ren, X. Wei, W. Weng, P. Du, G. Shen, G. Han, *Ceram. Int.* **2009**, *35*, 51–53.
[30] A. M. Lopes, J. P. Araujo, S. Ferdov, *Dalt. Trans* **2014**, *43*, 18010–18016.
[31] C. Quievryn, S. Bernard, P. Miele, *Nanomater. Nanotechnol.* **2014**, *4*, 1–8.
[32] C. Feldmann, H. O. Jungk, *Angew. Chemie - Int. Ed.* **2001**, *40*, 359–362.
[33] W. Cai, J. *J.* Wan, *Colloid Interface Sci.* **2007**, *305*, 366–370.
[34] H.-O. Jungk, C. Feldmann, *J. Mater. Sci.* **2001**, *36*, 297–299.
[35] C. Feldmann, *Adv. Funct. Mater.* **2003**, *13*, 101–107.
[36] D. Voll, A. Beran, H. Schneider, *Phys. Chem. Miner.* **2006**, *33*, 623–628.
[37] L. Kovács, K. Lengyel, Á. Péter, K. Polgár, A. Beran, *Opt. Mater. (Amst).* **2003**, *24*, 457–463.
[38] F. Kimura, J. Umemura, T. Takenaka, *Langmuir* **1986**, *2*, 96–101.
[39] T. T. Nguyen, M. Raupach, L. J. Janik, *Clays Clay Miner.* **1987**, *35*, 60–67.
[40] S. K. Srivastav, N. S. Gajbhiye, *J. Am. Ceram. Soc.* **2012**, *95*, 3678–3682.
[41] M. M. Murshed, C. B. Mendive, M. Curti, M. Šehović, A. Friedrich, M. Fischer, T. M. Gesing, *J. Solid State Chem.* **2015**, *229*, 87–96.
[42] J. M. Moreau, C. Michel, R. Gerson, W. J. James, *J. Phys. Chem. Solids* **1971**, *32*, 1315–1320.
[43] R. D. Shannon, *Acta Crystallogr.* **1976**, *A32*, 751–767.
[44] Th. M. Gesing, M. Schowalter, C. Weidenthaler, M. M. Murshed, G. Nénert, C. B. Mendive, M. Curti, A. Rosenauer, J.-Ch. Buhl, H. Schneider, R. X. Fischer, J*. Mater. Chem*. **2012**, *22*, 18814-18823.

Chapter 4

Temperature-dependent structural and spectroscopic studies of $(Bi_{1-x}Fe_x)FeO_3$

Andrea Kirsch[a,b], M. Mangir Murshed[a,b*], Melanie J. Kirkham[c], Ashfia Huq[c], F. Jochen Litterst[d], Thorsten M. Gesing[a,b]

[a]University of Bremen, Institute of Inorganic Chemistry and Crystallography, Leobener Straße 7, D-28359, Bremen, Germany

[b]University of Bremen, MAPEX center for materials and processes, Bibliothekstraße 1, D-28359 Bremen, Germany

[c]Chemical and Engineering Materials Division, Oak Ridge National Laboratory, Oak Ridge, Tennessee 37831, USA

[d]Institute for Condensed Matter Physics, Technische Universität Braunschweig, Mendelssohnstr. 3, D-38106 Braunschweig, Germany

*Corresponding author; e-mail address: murshed@uni-bremen.de; phone: +49 (0)421 218 63144; fax: +49 (0)421 218 63144

Abstract

We report on temperature-dependent structural and spectroscopic features of $(Bi_{1-x}Fe_x)FeO_3$ perovskite for x = 0.15 and 0.25. Samples were synthesized by heating quantum crystalline precursors obtained by polyol method. Crystal structures of each composition were obtained from in-house X-ray, synchrotron X-ray and time-of-flight neutron powder diffraction data Rietveld refinements. Partial replacement of the Bi-site by Fe^{3+} cation significantly changes the crystal-physico-chemical properties such as thermal expansion, polyhedral distortion, Debye temperature, vibrational and magnetic properties. Whereas $BiFeO_3$ is a multiferroic, both $Bi_{0.85}Fe_{0.15}FeO_3$ and $Bi_{0.75}Fe_{0.25}FeO_3$ are found to be superparamagnetic as observed by temperature-dependent Mössbauer and SQUID measurements. Lattice thermal expansion was modeled using the Debye-Einstein-Anharmonicity approach. Debye temperatures obtained from mean-squared atomic displacement parameter and lattice thermal expansion are compared. Temperature dependency of selective Raman modes is also analyzed.

1. Introduction

Perovskite-type bismuth ferrite $BiFeO_3$ received much attention due to its unique multiferroic properties and promising applications.[1,2] It is concomitantly antiferromagnetic and ferroelectric at room temperature[2] with a Néel temperature of ~640 K and Curie temperature of ~1100 K, respectively.[3] The magnetic structure is of G-type and possesses a canted spiral spin arrangement with a propagation direction of <110> (hexagonal setting) with a periodic length of 62 nm.[4] This cycloidal magnetic order does not show net magnetization in the bulk.[5] However, as much as a net magnetization of ~1.5 A m^2 kg^{-1} is observed in the nanoparticles when the spiral spin is suppressed.[6] The centrosymmetric distortion of the Bi^{3+} and Fe^{3+} cations along the hexagonal **c**-axis, caused by the stereochemical activity of the Bi^{3+} $6s^2$ lone electron pair[7] (LEP), produces a spontaneous polarization in this direction[8], as shown in Figure 1.

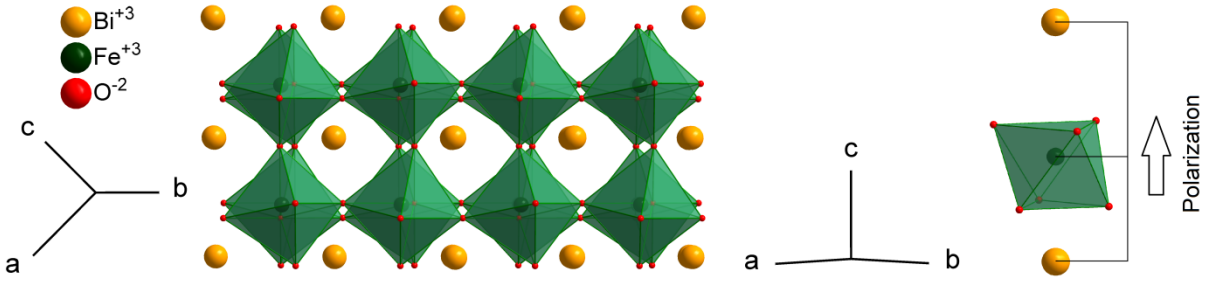

Figure 1. Crystal structure of perovskite-type $BiFeO_3$ in the space group *R*3*c* with a polarization along the **c**-direction when using the hexagonal setting.

The crystal structure is described in the rhombohedral *R*3*c* space group with hexagonal lattice parameter *a* = 558.76(3) pm and *c* = 1386.7(1) pm.[9] The FeO_6 octahedra are tilted towards each other along the **c**-axis, and the Bi^{3+} cations are located eccentrically in their cavities. The multiferroic properties of $BiFeO_3$ have been widely studied in the form of nanoparticles,[10] single crystals,[11] polycrystals[12] and thin films[13]. Despite intense studies on $BiFeO_3$, some of its physical properties are not fully understood, and debates are ongoing on some contradictory results.[1,6,10] Catalan and Scott (2009) pointed out that further systematic studies on the phase diagram, crystal chemistry, structure and dynamics are of crucial importance for an in-depth exploration.[1] Jia et al. (2014) evidently demonstrated substantial atomic- to nano-

scale disordering even in single crystals.[11] They supposed a sluggish phase evolutionary behavior of $BiFeO_3$ that makes it notoriously difficult in producing fully equilibrated single crystals.[11] Indeed, during transformation of an X-ray amorphous powder into a polycrystalline $Bi_2Fe_4O_9$ an intermediate $(Bi_{1-x}Fe_x)FeO_3$ phase was found supported by ^{57}Fe Mössbauer and temperature-dependent X-ray diffraction.[14] In this intermediate structure, the Bi^{3+} site is partially shared by Fe^{3+}, which transformed into the $BiFeO_3$ perovskite phase upon increasing temperature.[14] In the present study, a precursor was synthesized by a sol-gel route using sorbitol as a complexing agent. By subsequent heating, samples with different Fe-content on the Bi position were reproducibly produced. They were characterized by X-ray powder diffraction (XRD), temperature-dependent time-of-flight neutron powder diffraction (NPD), temperature-dependent Raman and ^{57}Fe Mössbauer spectroscopy. The thermal expansion of the metric parameters as well as the atomic displacement parameters (ADP's) were modelled using a microscopic approach.[15-19]

2. Experimental

2.1. Synthesis

The stoichiometric $BiFeO_3$ sample was synthesized using the glycerin method[20] and a molar ratio of Bi : Fe = 1 : 1 with an excess of 5% of Bi. 5.25 mmol $Bi(NO_3)_3 \cdot 5H_2O$ (Sigma-Aldrich, ≥ 98%), 5 mmol $Fe(NO_3)_3 \cdot 9H_2O$ (Sigma-Aldrich, ≥ 98%) and 10% glycerin of the total amount of nitrates were heated in a beaker using a glycerin bath to 353 K until NO_x was released and a dried gel was obtained. The mixture was then heated in a furnace at 523 K for 2 hours, ground in a mortar, afterwards heated at 773 K for 6 hours.

The precursor of the substituted ($(Bi_{1-x}Fe_x)FeO_3$) samples was synthesized by a sol-gel route using sorbitol as a complexing agent. As much as 11 mmol D-Sorbitol was dissolved in 38 mL deionized water under magnetic stirring. Then 5 mmol $Bi(NO_3)_3 \cdot 5H_2O$ (Sigma-Aldrich, ≥ 98%), 2 mL 4 M NaOH (VWR Chemicals, 99.2%) and 10 mmol $Fe(NO_3)_3 \cdot 9H_2O$ (Sigma-Aldrich, ≥ 98%) were added. The mixture was heated in a beaker using a glycerin bath at 353 K until a solid foam was obtained. It was then heated at 523 K for 2 hours, ground in a mortar and heated again at 873 K for different periods (10, 20, 30 and 40 minutes).

2.2. Diffraction

X-ray

X-ray powder diffraction data were collected on a X'Pert MPD PRO diffractometer (PANalytical GmbH, Almelo, The Netherlands) equipped with Ni-filtered $CuK_{\alpha 1,2}$ radiation ($\lambda_{K\alpha 1}$ = 154.05929(5) pm, $\lambda_{K\alpha 2}$ = 154.4414(2) pm) and a X'Celerator detector system in Bragg-Brentano geometry. Room-temperature scans were performed from 5 to 85° 2*θ* with a step width of 0.0167° 2*θ and a measurement time of 142 s per step*. The measurements of samples $(Bi_{0.75}Fe_{0.25})FeO_3$ and $(Bi_{0.85}Fe_{0.15})FeO_3$ were divided into two parts. Dataset-1 was measured between 5° and 85° 2*θ* with a step width of 0.0167° 2*θ and a measurement time of 142 s per step, and dataset-2* between 80° and 130° 2*θ* with a step width of 0.0167° 2*θ and a measurement time of 284 s per step*.

At ambient condition, X-ray powder diffraction patterns were additionally collected on the high-resolution powder diffractometer at beamline 11-BM at the Advanced Photon Source (APS), Argonne National Laboratory, USA. The wavelength was calibrated to 51.7041(1) pm and the diffraction patterns were recorded from 0.5° to 50° 2*θ* with a step width of 0.001° 2*θ, and a measurement time of 0.1 s per step*. The obtained data were refined using the Rietveld method (DIFFRAC PLUS TOPAS V4.2, Bruker AXS, Karlsruhe, Germany). For profile fitting the fundamental parameter approach was used. The fundamental parameters for the in-house data were fitted against a LaB_6 standard material. The occupancy between Fe^{3+} and Bi^{3+} were refined on the 6*a* position. The ADPs and the occupancy parameters were alternately refined until the satisfactory convergence appeared as suggested by Massa[21].

Neutron time-of-flight

NPD data were collected on Powgen high-resolution powder diffractometer at the Spallation Neutron Source (SNS), Oak Ridge National Laboratory (ORNL), USA. Temperature-dependent data were measured using the Cryo-furnace Janis between 10 K and 650 K at 10 K steps and a centre wavelength of about 133(1) pm for about half an hour at each temperature. Rietveld refinements were performed using the GSAS[22] program with EXPGUI interface.[23]

2.3. Spectroscopy

Raman

Temperature-dependent Raman spectra were measured on pressed pellets produced from the powder samples. A Horiba LabRam Aramis spectrometer equipped with a 785 nm emission Laser, a slit of 100 µm, a hole of 1000 µm and an exposure time of 10 s with 30 accumulations was used. Data were collected between 100 cm^{-1} and 1000 cm^{-1}. For the low-temperature measurements a Linkam cooling stage (THMS600) attached to a pump (LNP95 Cooling Pump) providing a continuous flow of liquid nitrogen were used. The high-temperature spectra were collected using a Linkam heating stage (TS1500). Prior to the data collection the sample was equilibrated for 7 min at the desired temperature. The spectra were fitted with single peaks using the above-mentioned Rietveld software TOPAS V4.2.

Mössbauer

^{57}Fe Mössbauer absorption spectra were collected using a standard spectrometer with sinusoidal velocity sweep. The 20 mCi ^{57}Co in Rhodium γ-radiation source was kept at room temperature. Absorbers of the two powder specimens with thicknesses corresponding to about 15 $mg \cdot cm^{-2}$ of ^{57}Fe were included in polyethylene containers. The absorber temperatures were varied using a He-flow cryostat (CRYOVAC®). For data analysis, we used MossWinn 4.0 software.[24]

2.4 Magnetic measurements

Temperature-dependent magnetic susceptibility measurements were carried out with a Quantum-Design MPMS-XL-5 SQUID magnetometer equipped with a 5 T magnet in the range from 2 to 300 K at a magnetic field of 0.1 T. The isothermal magnetization was measured at 300 K. The polycrystalline samples were put into a gel bucket covered with a few drops of low viscosity perfluoropolyether based inert oil (Fomblin YL VAC 25/6) and fixed to a nonmagnetic sample holder. Each raw data of magnetic moment was background corrected for the respective diamagnetic contribution of the gel bucket and the inert oil.

3. Results and discussion

3.1. X-Ray powder diffraction

The in-house X-ray powder diffraction patterns of the samples produced at 873 K using different crystallization times show only reflections of the perovskite-type phase as given in Figure 2. However, some very weakly intense but sharp reflections can be seen from the synchrotron data (Figure 2). The sources of these reflections were not identified so far, and the frequently occurring impurities in the Bi-Fe-O system such as $Bi_2Fe_4O_9$[25], $Bi_{25}FeO_{40}$[25], $Bi_{24}Fe_2O_{39}$[25], α- Bi_2O_3 or β-Bi_2O_3[26], or α-Fe_2O_3[27] do not belong to these reflections.

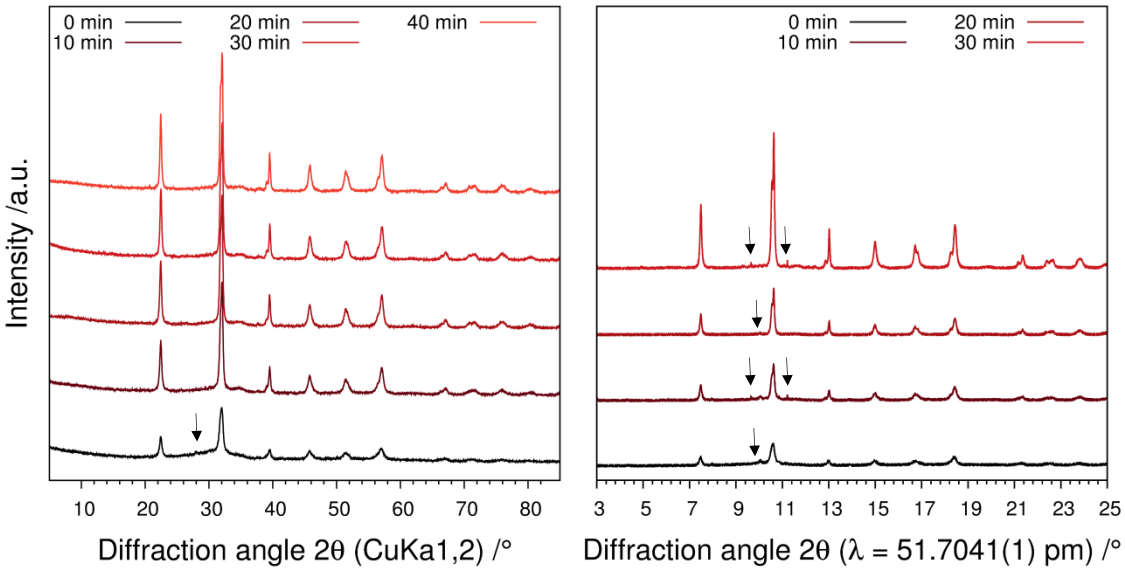

Figure 2. X-ray diffraction patterns of $(Bi_{1-x}Fe_x)FeO_3$ samples produced at 873 K for 0, 10, 20, 30 and 40 min, measured in-house (left panel) and at APS, Argonne, USA (right panel) facilities. Unindexed reflections appeared in the synchrotron X-ray patterns are marked by arrows.

According to earlier studies[14] Rietveld refinements on this data were performed by concomitantly refining the Bi^{3+} and Fe^{3+} content on the 6*a* (0,0,0) site. It was found that the Fe content on this site decreases with crystallization time, as shown in Figure 3.

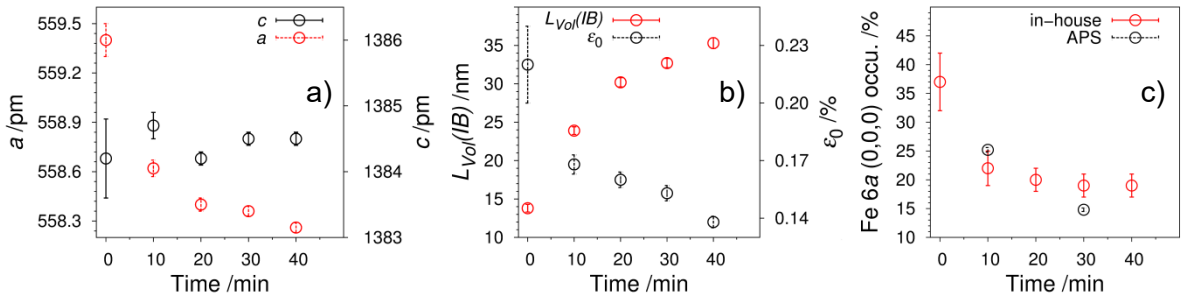

Figure 3. Structural parameters derived from the in-house X-ray data Rietveld refinements on the samples produced at 873 K for 0, 10, 20, 30 and 40 min, respectively.

It is reasonable to assume that with increasing crystallization time an exchange occurs between Bi in the precursor-matrix (quantum crystalline/X-ray amorphous) and the Fe on the 6*a* (0,0,0) site, leading to successive decrease of the Fe-content on this site, followed by formation of stoichiometric $BiFeO_3$. The background (broad hump centered at ~31° 2θ (CuKα)) decreases with increasing crystallization time (Figure 2). As a consequence, the lattice parameter *a* and the micro-strain decrease from 559.4(1) pm to 558.26(3) pm, and from 0.22(2)% to 0.14(1)%, respectively. Opposite, the average crystallite size increases from 13.8(5) nm to 35.3(7) nm (Figure 3). The samples $(Bi_{0.75}Fe_{0.25})FeO_3$ and $(Bi_{0.85}Fe_{0.15})FeO_3$ of this series were further investigated by other techniques (see below); their refined structural data are given in Table 1.

Table 1. Crystal structural parameters of $BiFeO_3$[9], $(Bi_{0.75}Fe_{0.25})FeO_3$ and $(Bi_{0.85}Fe_{0.15})FeO_3$.

Atom	Wyckoff position	*x*	*y*	*z*	Occupancy	*B* /pm^2 x10^4
Ideal model[9]						
Bi	6*a*	0	0	0	1	
Fe	6*a*	0	0	0.25	1	
O	18*b*	0.5	0	0	1	
BiFeO3[9]						
Bi	6*a*	0	0	0[a]	1	0.5
Fe	6*a*	0	0	0.2212(15)	1	0.8
O	18*b*	0.443(2)	0.012(4)	0.9543(20)	1	-
$(Bi_{0.85}Fe_{0.15})FeO_3$*						
Bi/Fe	6*a*	0	0	0 [a]	0.85(1)/0.15(1)	0.143(6) *1.3(2)*
Fe(2)	6*a*	0	0	0.22049(7) *0.2196(4)*	1	0.13(2) *0.32(7)*
O	18*b*	0.4602(9) *0.453(1)*	0.0348(7) *0.027(1)*	0.9470(3) *0.9507(6)*	1	0.8(1) *1.11(8)*
$(Bi_{0.75}Fe_{0.25})FeO_3$*						
Bi/Fe	6*a*	0	0	0 [a]	0.75(1)/0.25(1)	0.183(9) *1.7(2)*
Fe(2)	6*a*	0	0	0.2194(1) *0.2193(5)*	1	0.183(9) *0.63(8)*
O	18*b*	0.459(1) *0.456(2)*	0.0390(9) *0.033(2)*	0.9421(4) *0.9503(8)*	1	0.4(1) *1.6(2)*

*values in normal and italic are obtained by synchrotron X-ray and neutron time-of-flight powder data Rietveld refinement, respectively. [a] Positional parameter were fixed during the refinements

Since Bi and Fe share the 6*a* site (0,0,0; *z* fixed), even though their electronic configuration is significantly different (Z_{Fe} = 26; Z_{Bi} = 83), their displacement parameter was refined with constraint (Table 1). Theoretical X-ray patterns (using identical metric parameters) produced by POWDER CELL[28] showed significant difference between, for instance, $BiFeO_3$ and $(Bi_{0.85}Fe_{0.15})FeO_3$, as can be seen from the intensity of the (*012*) reflection. From a visual inspection one can draw a comparative agreement between the observed and the simulated patterns, as shown in Figure 1S (Supplementary Information). From synchrotron X-ray data Rietveld refinements of $(Bi_{0.85}Fe_{0.15})FeO_3$, of which the plot is shown in Figure 2S (Supplementary information), as much as ~5% mullite-type $Bi_2Fe_4O_9$ was identified in the sample. Some $(Bi_{0.85}Fe_{0.15})FeO_3$ reflections show a strong anisotropy, especially the high intense (*110*) reflection. An even more pronounced anisotropic feature can be seen in the (*202*) reflection, as shown in the magnification in the interested region (Figure 2S). Consequently, the average crystallite size was estimated to be 45.3(5) nm from the diffraction pattern excluding (*110*), (*202*), (*012*) and (*030*) and

almost doubled (75(1) nm) using only the (*110*) reflection. Due to such anisotropies, using separate reflection profiles for the (*110*), (*202*), (*012*) and (*030*) reflections provided better convergence during the structure refinements. Of particular notes, the magnetic spiral spin propagates in the <110> direction, and consequently the spins rotate in the [110] plane[4].

3.2. Neutron powder diffraction

Structural features of the stoichiometric $BiFeO_3$[9] and the ideal perovskite model[9] are given in Table 1. The positional parameters of $(Bi_{0.75}Fe_{0.25})FeO_3$ and $(Bi_{0.85}Fe_{0.15})FeO_3$ together with the isotropic atomic displacement parameters were followed by temperature-dependent NPD as shown in Figure 4.

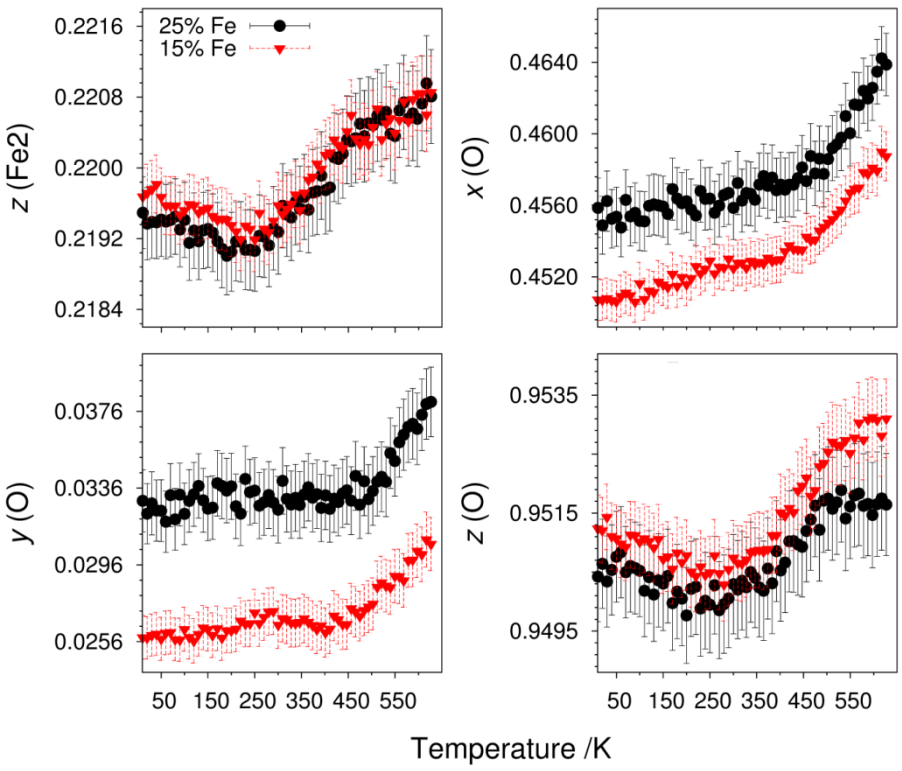

Figure 4. Temperature-dependent changes of selective atomic coordinates obtained from neutron time-of-flight powder diffraction data Rietveld refinements.

With increasing Fe on the Bi-site (6*a*: 0,0,0: *z* fixed), the Fe(2) (6*a*: 0,0,*z*) gradually shifts away from the hypothetical centroid. That is, Fe(2) shifts about 33 pm and 38 pm from the centroid for $(Bi_{0.85}Fe_{0.15})FeO_3$ and $(Bi_{0.75}Fe_{0.25})FeO_3$, respectively. This could be explained by an increased distortion of the BiO_6 coordination due to smaller ionic radius of Fe^{3+} (64.5 pm) than that of Bi^{3+} (103 pm).[29] Palewicz et al.

(2009) studied the evolution of structural parameters of stoichiometric $BiFeO_3$ by neutron powder diffraction below[30] and above[31] room temperature, which increase monotonically with respect to temperature, except a decrease of *y*-coordinate of the O-site.[30] The atomic coordinates change with increasing temperature (Fig. 4). At about 240 K a deep minimum has been observed for the change of the *z*-coordinates of the Fe(2)- and O-site in $(Bi_{0.75}Fe_{0.25})FeO_3$. This minimum has been shifted to 260 K for $(Bi_{0.85}Fe_{0.15})FeO_3$. The *x*- and *y*-coordinates of the O-sites of both phases slowly increase up to ~ 450 K followed by a sharp slope (which is at a slightly higher temperature for $(Bi_{0.75}Fe_{0.25})FeO_3$, opposite to the behaviour of the deep minimum temperatures). At this temperature, a sudden frequency drop of the A_1-1 mode was observed in the Raman spectra (see later). Moreover, a pronounced change in the slope for the ADP's of the Bi/Fe- and Fe-sites was observed (see later). The changes of bond lengths and bond angles are given in Figure 5. The long Bi/Fe-Fe distance (Figure 5a) shows a maximum at about ~ 250 K (Figure 5a), which could be correlated to the deep minimum observed for the change of the *z*-coordinates of the Fe(2)- and O-sites.

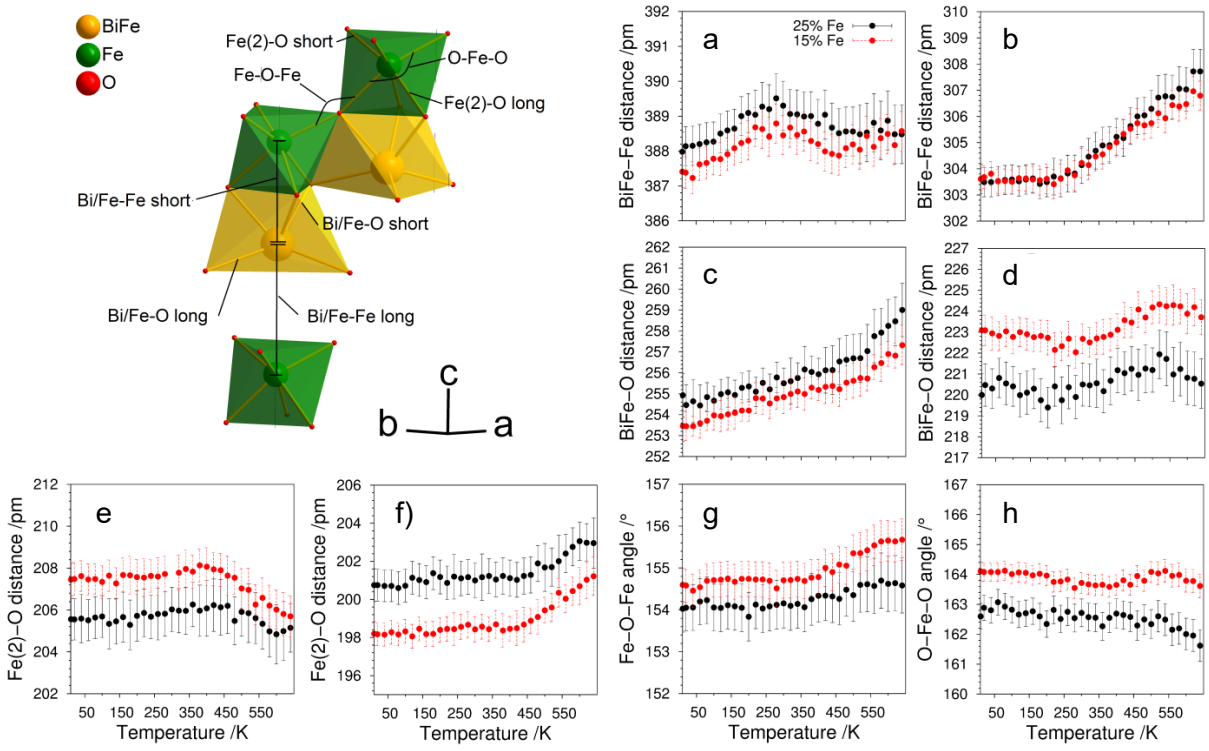

Figure 5. Coordination and connectivity in $(Bi_{1-x}Fe_x)FeO_3$ (top) and the changes of selective structural parameters with temperature (bottom).

The short Bi/Fe-Fe distance (Figure 5b) also shows a point of inflection at 250 K. A maximum in the long Bi-Fe distance was also observed by Palewicz et al. (2007)[31] but only at 550 K. The Fe(2)-O bond length of the fully occupied Fe-position (Figure 5e and 5f) remains nearly unchanged until ~ 400 K for $(Bi_{0.85}Fe_{0.15})FeO_3$ and ~ 450 K for $(Bi_{0.75}Fe_{0.25})FeO_3$. Afterward, the long Fe-O bond length decreases while the short Fe-O bond length increases simultaneously. In general, these bond lengths differ from reported values for $BiFeO_3$ (211.41(17) pm, 194.70(17) pm at 298 K)[30] in a way that the normally huge difference of 16.7(4) pm is decreased to 9(1) pm for $(Bi_{0.85}Fe_{0.15})FeO_3$ (207.87(78) pm, 198.43(67) pm at 300 K) and even more remarkable to 5(2) pm (206(1) pm, 201(09) pm at 300 K) for $(Bi_{0.75}Fe_{0.25})FeO_3$ (Figure 5).

While the difference in the two bond lengths of the $Fe(2)O_6$ octahedra decreases with a higher Fe-content on the Bi-position it increases in the $(Bi/Fe)O_6$ octahedra. The long and short Bi/Fe-O distances are determined to be 255.5(7) pm and 220.5(10) pm for $(Bi_{0.75}Fe_{0.25})FeO_3$ and 254.84(79) pm and 222.68(71) for $(Bi_{0.85}Fe_{0.15})FeO_3$ (Figure 5), respectively. Compared to calculated values of the model structure of $BiFeO_3$[9] (252.42(171) pm, 231.42(231) pm) the difference between long and short Bi/Fe-O distance increases from 21(4) pm, 32(1) pm and 35(2) pm for samples with a Fe-content of 0%, 15% and 25% on the Bi-position, respectively. With increasing temperature, the long Bi/Fe-O bond length linearly increases with a steeper slope from 550 K on. On the contrary, the short Bi/Fe-O distance remains unchanged with a weak rise from ~250 K to ~550 K followed by a negative slope afterwards. The Fe-O-Fe angle, as depicted in Figure 5, slowly increases for both samples (154.0(6)° to 154.6(7)° for $(Bi_{0.75}Fe_{0.25})FeO_3$; 154.6(4)° to 155.7(5)° for $(Bi_{0.85}Fe_{0.15})FeO_3$) from 10 K to 640 K. Palewicz et al. (2007 and 2010) reported an increase of this angle from 154.75(8)[30] to 156.0(1)[31] from 5 K to 643 K for stoichiometric $BiFeO_3$. The internal O-Fe-O angles slightly decrease with temperature.

The Wang-Liebau eccentricity (WLE) parameter[32] was calculated for the $(Bi/Fe)O_6$ octahedra for the samples as well as for the stoichiometric $BiFeO_3$[31]; their temperature dependency is shown in Figure 3S (Supplementary information). The WLE of the $(Bi/Fe)O_6$ octahedra increases with the Fe content on the Bi-position from $2.34 \cdot 10^{-5}$ over $2.96 \cdot 10^{-5}$ to $3.37 \cdot 10^{-5}$ for a Fe occupancy of 0%, 15% and 25%, respectively. Nevertheless, it is unlikely that the stereochemical activity of lone

electron pair (LEP) of the Bi^{3+} cation increases while the Fe content at this site increases. In this case, the octahedral distortion mainly increases due to two different sized ions at a given crystallographic site as shown in Figure 6, where octahedral mean quadratic elongation (λ)[33] was compared between the $(Bi/Fe)O_6$ and $Fe(2)O_6$ octahedra. As such, a pronounced distortion of the Bi/FeO_6 octahedra can be seen for the Bi/Fe sites, and the points of inflection with respect to temperature are comparable to those of interatomic bond distances and angles (Figure 5).

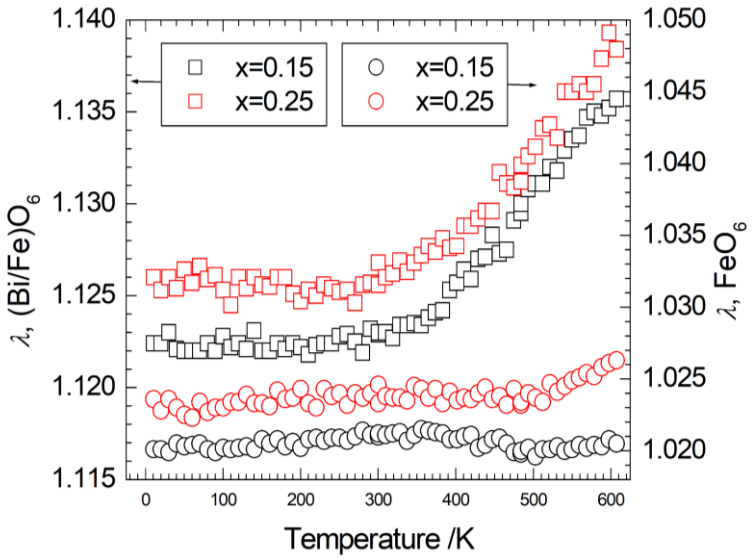

Figure 6. Temperature-dependent octahedral mean quadratic elongation (λ) of the $(Bi/Fe)O_6$ and $Fe(2)O_6$ octahedra of $(Bi_{1-x}Fe_x)FeO_3$.

The temperature-dependent ADPs of both phases are shown in Figure 7 along with the fitting model based on the Debye approach suggested by Lonsdale[34], and the fitting parameters are given in Table 2.

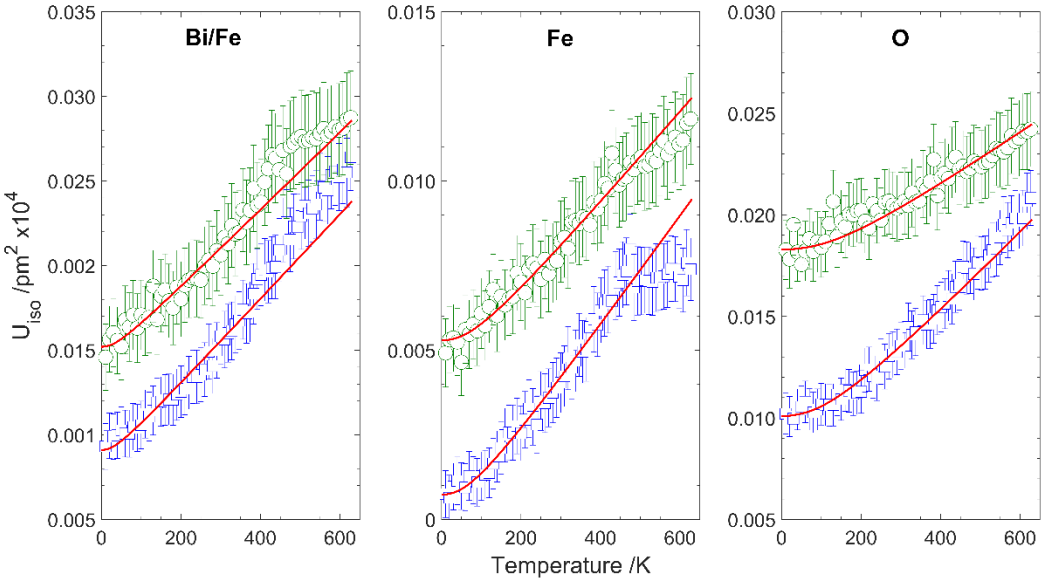

Figure 7. Temperature-dependent isotropic mean-squared atomic displacement parameters (ADPs) of the atoms along with the respective Debye model fit. The circle, square and diamond refer to $BiFeO_3$, $(Bi_{0.85}Fe_{0.15})FeO_3$ and $(Bi_{0.75}Fe_{0.25})FeO_3$, respectively.

Table 2. Fitting parameters of the mean-squared isotropic displacement parameters (ADPs).

	$Bi_{0.85}Fe_{0.15}FeO_3$		$Bi_{0.75}Fe_{0.25}FeO_3$	
Atom	θ_{Di} /K	B_{sta} /pm^2	θ_{Di} /K	B_{sta} /pm^2
Bi/Fe	161(3)	71(7)	184(5)	139(1)
Fe	426(10)	4.5(1)	455(9)	40(2)
O	647(11)	63(7)	854(23)	160(6)
Mass weighted	**293(10)**	**-**	**356(13)**	**-**

B_{sta} refers to static disorder of the respective atom. The estimated uncertainty is given in the parentheses.

The ADPs at any given temperature follow the order O > Fe > Bi, which agree well with most of common findings.[30,31] However, the ADPs as well as the static disorder increase with increasing Fe-content in the perovskite. Static disorder calculated from the 0 K intercept of the linear extrapolation of the ADP data down to the Debye temperature agrees well to the values calculated from the direct Debye-fit of the temperature-dependent ADPs which monotonically increases over the whole temperature range. Since the characteristic Debye temperature represents the binding forces between the lattice sites, the consequent change of the atomic Debye

temperature (θ_{Di}) upon partial replacement of bismuth by iron is clearly observed (Table 2). Whereas the Debye temperatures of Bi/Fe and Fe, for both phases, lie close to each other, the Debye temperature of oxygen atom significantly differs. That is, for instance, the oxygen in $(Bi_{0.75}Fe_{0.25})FeO_3$ locates in a stiffer coordination. Due to this dominant role of oxygen the mass-weighted Debye temperature of $(Bi_{0.75}Fe_{0.25})FeO_3$ (356 K) is higher than that of $(Bi_{0.85}Fe_{0.15})FeO_3$ (293 K). This result differs from that of $(Bi_{1-x}Re_x)FeO_3$ (Re = La, Eu, Ho) multiferroics, where the Debye temperature is inversely proportional to the compositional x-value.[35]

3.2. Spectroscopy

Raman spectroscopy

The Brillouin zone-centre optical phonon modes of space group *R*3*c* can be classified as $4A_1 + 5A_2 + 9E$. The A_1- and E-modes are polarized along the *z*-axis and the *xy*-plane, respectively, and both are Raman and IR active. Some of the A_2 modes calculated at 109, 261, 308, 446, and 579 cm^{-1} are optically silent, however can be observed by inelastic neutron scattering.[36] Raman spectra of the samples are shown in Figure 8. Of better resolved intense modes, the frequencies at 146.5 cm^{-1} and 174.6 cm^{-1} are observed for $BiFeO_3$, which are assigned to E(TO2) and A_1(TO1), respectively.[37] Both of them slightly shift to corresponding higher frequency for $(Bi_{0.85}Fe_{0.15})FeO_3$ (147.3(1) and 174.6(1) cm^{-1}) and $(Bi_{0.75}Fe_{0.25})FeO_3$ (148.8(1) and 175.0(1) cm^{-1}).

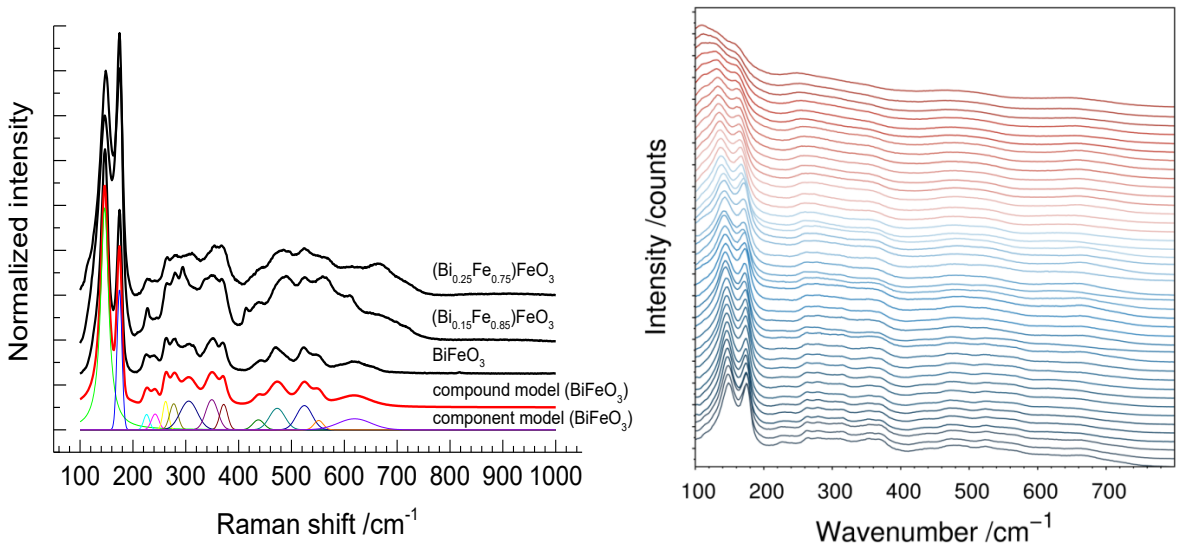

Figure 8. Left panel: Low-temperature (78 K) Raman spectra along with the compound as well as component fit models. Right panel: Temperature-dependent Raman spectra of $(Bi_{0.75}Fe_{0.15})FeO_3$; temperature increases from 78 K (bottom) to 610 K (top) at 10 K step and from 350 K on at 20 K step.

First principal studies[37] demonstrated that frequencies up to 167 cm^{-1} belongs purely to Bi-atoms, and Fe-atoms mainly contribute between 152 and 261 cm^{-1}, and also to higher-frequencies. Consequently, the intensity ratio of I_{147}/I_{175} decreases upon successive replacement of Fe in the Bi-site since both the frequencies are indicative for one of the sites.[10] The temperature-dependence of E(TO2) and A_1(TO1) modes for $BiFeO_3$, $(Bi_{0.75}Fe_{0.25})FeO_3$ and $(Bi_{0.85}Fe_{0.15})FeO_3$ are shown in Figure 4S (Supplementary information). The frequency of the modes at 0 K has been obtained from the linear extrapolation of the low temperature data and listed in Table 3. The mode-Grüneisen parameter was calculated from the volume derivative and listed in Table 1S. The corresponding cell volumes were taken from the respective thermal-expansion model fitting (see later).

Mössbauer spectroscopy

Temperature-dependent ^{57}Fe Mössbauer spectra are depicted in Figure 9. Hyperfine parameters are collected in Table 4. The experimentally determined values of isomer shift (IS) are typical for high spin Fe^{3+} ions.[38] No signals from high spin Fe^{2+} could be resolved; their isomer shifts would lie above about 0.6-0.7 $mm \cdot s^{-1}$.[38,39] Consequently, magnetite (Fe_3O_4) as an impurity must be excluded. Comparing the determined hyperfine parameters (Table 3) one can safely assume that any of our samples does not contain impurities such as γ-Fe_2O_3[40,41,42] or α-Fe_2O_3.[40,43,44] Spectra at 300 K show a superposition of magnetically split patterns (i.e. from sites with static hyperfine fields) and doublet patterns from superparamagnetic sites. Magnetic hyperfine fields in the superparamagnetic fraction are averaged to zero due to fluctuations faster than the nuclear Larmor precession, that is, they must be on the order of GHz. Even at 300 K one can trace a slowing down of superparamagnetic relaxations for parts of the sample $(Bi_{0.85}Fe_{0.15})FeO_3$, resulting in a broad unresolved background covering about half of the total spectral area. Spectra of both samples at 200 K and 100 K reveal strongly broadened patterns and line shapes that deviate from a Lorentzian profile, which is typical for relaxation effects due to slow superparamagnetic fluctuations (Figure 9). These spectra are shown to demonstrate the general temperature-dependent spectral development. A detailed analysis would need knowledge of crystallite size distributions and crystallite anisotropy energies correlated with the relaxation time, which lies out of the scope of the present study. We rather concentrate on the analysis of the spectra at 300 K and 20 K. The latter can be deconvoluted with static magnetic sextets though the strongly broadened lines of sextet-4 of both samples, indicating that superparamagnetic fluctuations persists even at 20 K. All Fe^{3+} coordination's leading to doublets in the Mössbauer spectra exhibit a high quadrupolar splitting QS of 0.54(1) – 1.08(1) mm/s (Table 3). As such, a high distortion of the associated octahedra is expected since the quadrupolar splitting of octahedrally coordinated Fe^{3+} usually increases with a higher distortion.[39] Interestingly, these high QS are strongly reduced (-0.02 mm/s – 0.04 mm/s) when the samples are cooled down to 20 K, and static magnetic sextets of these sites have evolved. The apparent vanishing of QS can be related to a wide distribution of angles between magnetic hyperfine field and electric field gradient due to disorder. The IS of the doublets are smaller than those of the sextets, leading to higher charge density at the nucleus, thus smaller bond length. The sum of the

already static magnetic sextets (1+2, Table 3) in the room-temperature spectra represent a relative area of 36(4)% and 31(4)% for $(Bi_{0.75}Fe_{0.25})FeO_3$ and $(Bi_{0.85}Fe_{0.15})FeO_3$ of the spectra, respectively. However, the relative population of the magnitudes of sextet-1 and sextet-2 is different in both samples at any given temperature (Table 3). The relative areas of the doublets add up to 65(4)% in $(Bi_{0.75}Fe_{0.25})FeO_3$ and turn to sextet-3 and sextet-4 in the 20 K spectrum. Whereas in the room-temperature spectrum of $(Bi_{0.85}Fe_{0.15})FeO_3$ two doublets add up with a singlet to 69(6)%. Interestingly, sextet-3 and sextet-4 in the 20 K spectrum add up to only 55(4)% of the relative area. This corresponds to the area of the singlet in the room-temperature spectrum. Compared to the obtained hyperfine parameters of a $BiFeO_3$ sample with 14 nm sized crystals of Park et al. (2007) the determined parameters are comparable to those of $(Bi_{0.75}Fe_{0.25})FeO_3$.[6] In general, the Mössbauer lines are quite broadened showing values from 0.30(1) mm/s to 0.88(1) mm/s (Table 3), suggesting some sorts of disorder around the Fe-sites. Blaauw and van der Woude[45] pointed out that even in stoichiometric $BiFeO_3$ all Fe-sites are not completely equivalent and the crystallographic structure is of more complicated character.

Table 3. Hyperfine parameters of $(Bi_{1-x}Fe_x)FeO_3$. The standard deviations given in the parentheses.

Fit	*IS /mm s^{-1}	QS /mm s^{-1}	B_{hf} /T	Γ /mm s^{-1}	Rel. area /%
		$(Bi_{0.75}Fe_{0.25})FeO_3$			
Sextets		**300 K**			
1	0.36(1)	0.16(1)	49.4(1)	0.40(1)	20(2)
2	0.35(1)	0.02(1)	48.0(1)	0.50(1)	16(2)
Doublets					
3	0.29(1)	0.54(1)		0.40(1)	37(2)
4	0.27(1)	1.00(1)		0.40(1)	28(2)
Sextets		**20 K**			
1	0.48(1)	0.16(1)	54.9(1)	0.36(1)	18(2)
2	0.47(1)	0.08(1)	53.2(1)	0.40(1)	17(2)
3	0.42(1)	0.02(1)	50.3(1)	0.54(1)	37(2)
4	0.40(1)	-0.02(1)	47.0(1)	0.84(1)	28(2)
		$(Bi_{0.85}Fe_{0.15})FeO_3$			
Sextets		**300 K**			
1	0.35	0.16(1)	49.4(1)	0.40(1)	25(2)
2	0.35	0.00(1)	48.0(1)	0.40(1)	6(2)
Doublets					
3	0.29	0.54(1)		0.40(1)	9(2)
4	0.26	1.08(1)		0.40(1)	7(2)
Singlet	0.35				53(2)
Sextets		**20 K**			
1	0.48	0.34(1)	54.8(1)	0.32(1)	25(2)
2	0.47	-0.08(1)	54.5(1)	0.30(1)	19(2)
3	0.42	0.04(1)	51.0(1)	0.58(1)	35(2)
4	0.39	-0.02(1)	47.1(1)	0.88(1)	20(2)

*The isomer shift (IS) is relative to ^{57}Fe, QS (quadrupole splitting) = 1/2 e^2qQ, and B_{hf} to the magnetic hyperfine field at ^{57}Fe nuclei. Γ is the linewidth.

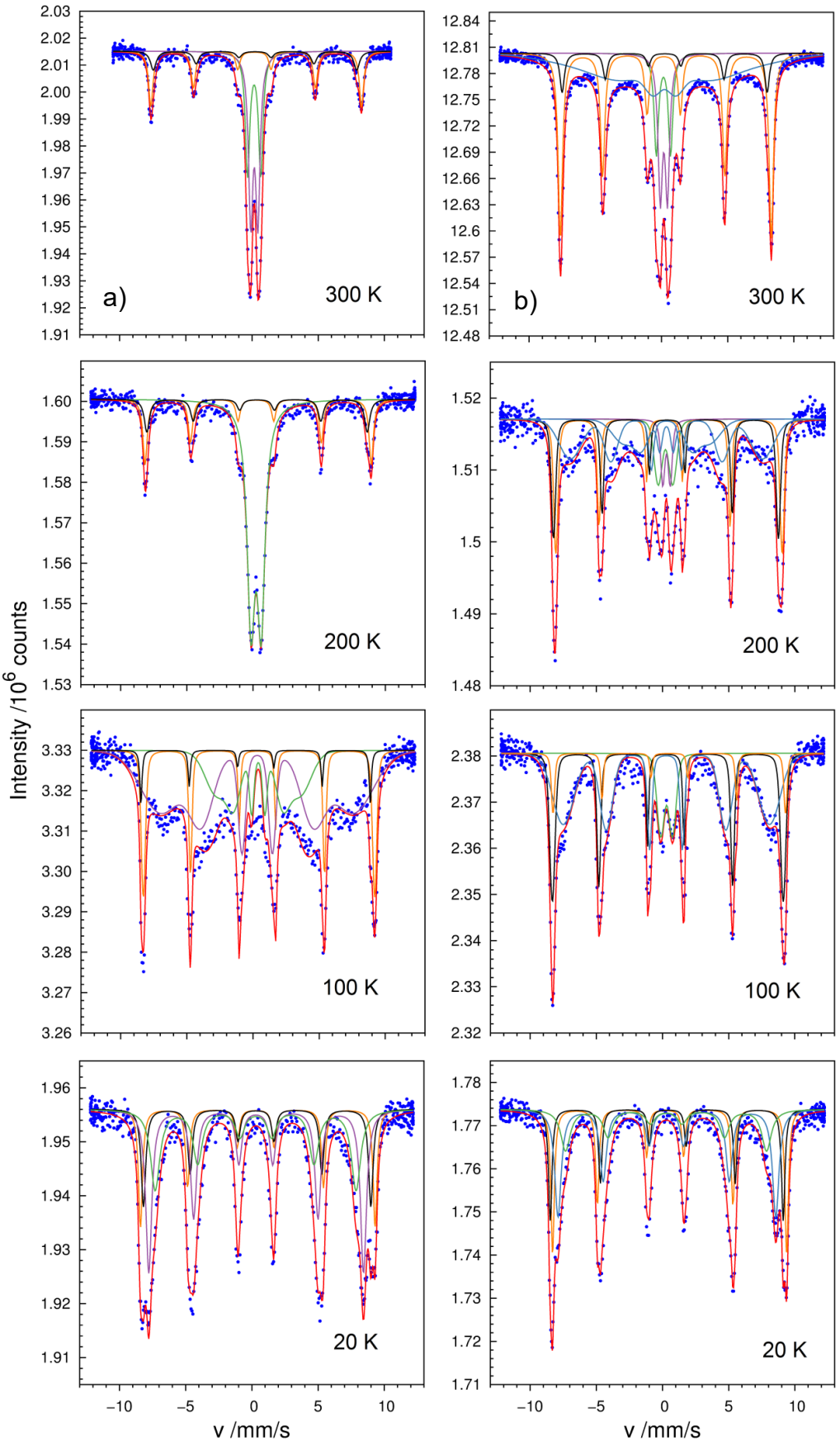

Figure 9. Temperature-dependent ^{57}Fe Mössbauer absorption spectra of $(Bi_{0.75}Fe_{0.25})FeO_3$ (a) and $(Bi_{0.85}Fe_{0.15})FeO_3$ (b).

3.4. DEA Modelling

Despite a large number of papers published on $BiFeO_3$, a complete set of elastic moduli were not experimentally obtained. As such, discrepancies between the experimentally obtained bulk modulus could not be judged as given in Table 2S (Supplementary information). Herein, we consider the ab initio based six independent elastic moduli (C_{ij}) of the rhombohedral symmetry and the corresponding bulk modulus for thermal expansion modeling. The change of the metric parameters with temperature obtained from neutron powder diffraction measurements are shown in Figure 10. The lattice thermal expansion was modelled using the DEA approach[15,17,18] and the fitting parameters are listed in Table 4. For comparison, we also analysed the temperature-dependent neutron powder data of $BiFeO_3$.[3,29,30] For each case, the simulation of the metric parameters shows an excellent fit considering only a single Debye term for the calculation of temperature-dependent vibrational energy. The integral term of the Debye function was numerically evaluated leading to Debye temperatures of 357(89) K, 392(81) K and 375(5) K for $(Bi_{0.75}Fe_{0.25})FeO_3$, $(Bi_{0.85}Fe_{0.15})FeO_3$ and $BiFeO_3$, respectively (Table 4). Notably, the neutron data of $BiFeO_3$ were limited only to 300 K. Kallaev et al. reported a Debye temperature of 500 K[35] calculated from the heat capacity (C_V). It is quite surprising that the Debye temperature evaluated from C_V measurements is higher than those of thermal expansion calculations. However, the authors took the bulk modulus of $Pb(Ti,Zr)O_3$; therefore, the reliability of such physical parameter is difficult to compare.

Table 4. Fitting parameters of the modelled temperature-dependent metric parameters.

	$(Bi_{0.75}Fe_{0.25})FeO_3$	$(Bi_{0.85}Fe_{0.15})FeO_3$	$BiFeO_3$*
Unit cell volume			
M_0 /10^6pm^3	372.4(9)	371.9(8)	372.39(1) / *373.10(5)*
k_D /10^{-12}Pa^{-1}	9.5(24)	8.91(2)	8.71(1) / *8.30(1)*
θ_D /K	357(89)	392(81)	361(30) / *328(42)*
Lattice parameter a			
M_0 /pm	557.5(4)	557.3(4)	557.35(1) / *557.70(2)*
k_D /10^{-12}Pa^{-1}	4.1(3)	3.7(3)	3.75(1) / *3.41(1)*
θ_D /K	321(22)	328(25)	423(5) / *345(10)*
Lattice parameter c			
M_0 /pm	1383.4(6)	1382.1(2)	1384.27(1) / *1384.95(5)*
k_D /10^{-12}Pa^{-1}	12.7(6)	12.7(2)	13.82(1) / *13.27(2)*
θ_D /K	268(12)	269(5)	306(7) / *234(23)*

* data from Palewicz et al.[30,31] and Fischer et al.[3] (*Italic*)

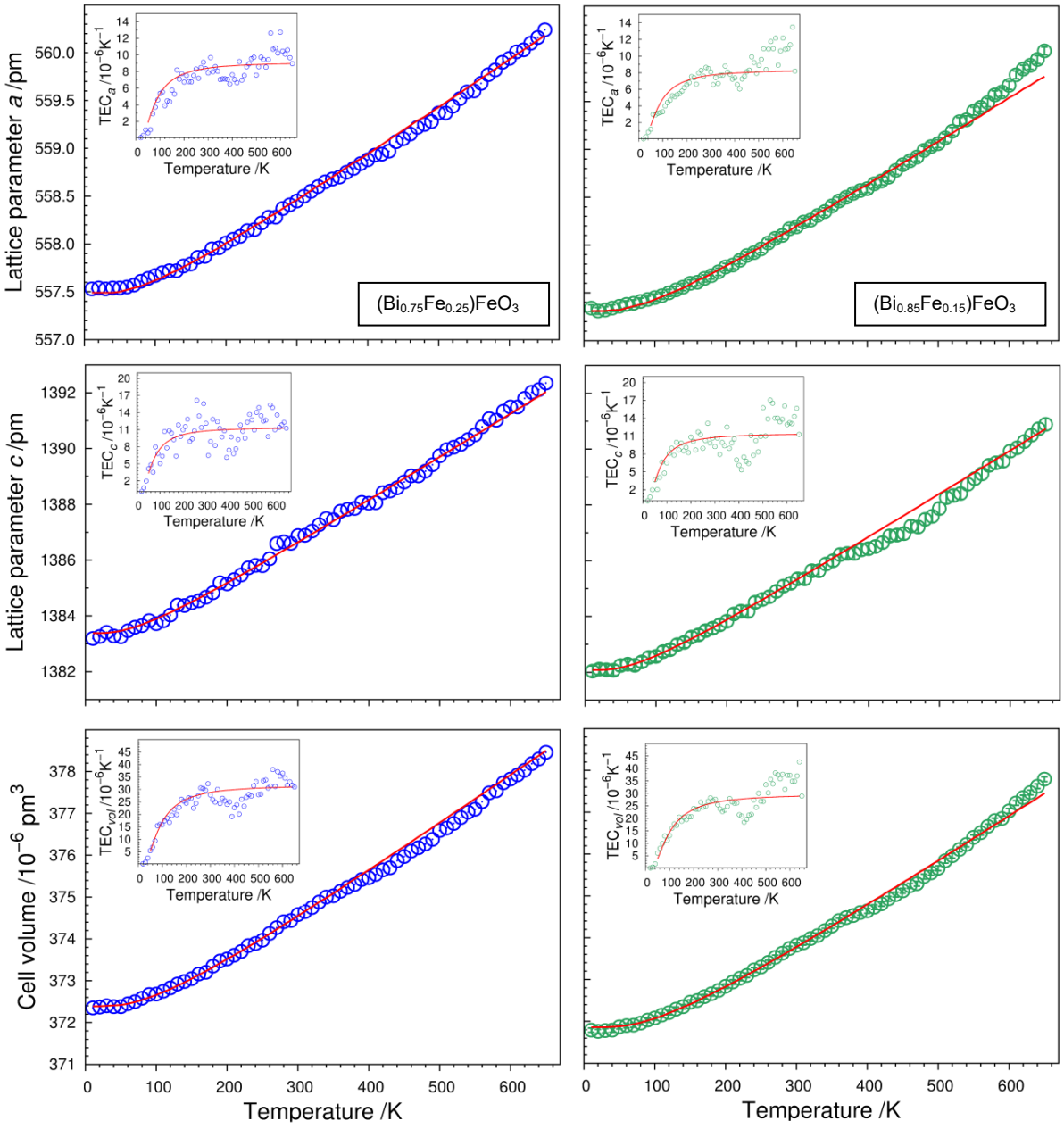

Figure 10. Temperature-dependent metric parameters and respective thermal expansion coefficient (TEC, inset) of $(Bi_{0.75}Fe_{0.25})FeO_3$ (left panel) and $(Bi_{0.85}Fe_{0.15})FeO_3$ (right panel).

The thermoelastic fitting parameter leads the thermodynamic Grüneisen parameter of $BiFeO_3$ to be γ = 0.87. Since the thermoelastic parameter (k_D) does not significantly change upon substitution of Bi with Fe (Table 4), a reasonable assumption of the Grüneisen parameter of 0.87 would lead to bulk moduli of 91(1) GPa, and 98(1) GPa for $(Bi_{0.85}Fe_{0.15})FeO_3$ and $(Bi_{0.75}Fe_{0.25})FeO_3$, respectively. The axial thermal expansion coefficient follows as $\alpha_c > \alpha_a$ (with α_a and α_c for *a*- and *c*-cell parameters). It shows an anomaly with a minimum at about 400 K for $(Bi_{0.75}Fe_{0.25})FeO_3$ and 420 K

for $(Bi_{0.85}Fe_{0.15})FeO_3$ as seen in the insets of Figure 10. However, these anomalies have not been seen for stoichiometric $BiFeO_3$[31] as within the temperature range (10 K - 300 K) the magnetic phase does not change (AFM for the whole range). Whether the TEC anomalies observed for both $(Bi_{0.75}Fe_{0.25})FeO_3$ and $(Bi_{0.85}Fe_{0.15})FeO_3$ are associated with magneto-volume effect due to corresponding magnetic phase transition is not clear at this stage.

3.5. SQUID analysis

To further evaluate the magnetic properties of the samples SQUID measurements on the samples $(Bi_{0.85}Fe_{0.15})FeO_3$, $(Bi_{0.75}Fe_{0.25})FeO_3$ and stoichiometric $BiFeO_3$ were performed. The magnetic hysteresis curves, as shown in Figure 11, clearly reveal a superparamagnetic behavior for $(Bi_{0.85}Fe_{0.15})FeO_3$ and $(Bi_{0.75}Fe_{0.25})FeO_3$ as already seen in the Mössbauer spectra (Figure 9). An enlarged view of these curves clearly shows no hints of remanence. The values obtained for the magnetization of $BiFeO_3$ however well fit those earlier reported.[6,10,46,47] The magnetization of $(Bi_{0.85}Fe_{0.15})FeO_3$ and $(Bi_{0.75}Fe_{0.25})FeO_3$ on the contrary is found to be very high with a magnetic saturation (M_s) of 7.3 A m^2 kg^{-1} and 7.8 A m^2 kg^{-1} at 300 K and 5 T, respectively. In comparison, some reported values for $BiFeO_3$ are 0.2 A m^2 kg^{-1},[48] ~0.35 A m^2 kg^{-1},[49] 1.4 A m^2 kg^{-1},[50] 1.55 A m^2 kg^{-1},[6] and 3.4 A m^2 kg^{-1}.[51] Mazumder et al. (2007)[47] observed saturation of as high as ~7 A m^2 kg^{-1} for nano-sized $BiFeO_3$, which is comparable to the present study. Recently, Guria et al. (2014)[52] found superparamagnetic behaviour of paramagnetic Sm_2O_3 at room temperature. This finding is unusual as superparamagnetism is generally known to be associated with ferromagnetic or ferrimagnetic materials due to size effects. They synthesized variously shaped nanostructures and stated that these differences in the magnetism clearly can be lead back to the difference in the growth patterns of the materials.[52] Our materials also show a strong anisotropy in the (202) and (110) planes, where the latter one is the rotation plane of the magnetic moments that develop the spiral magnetic structure.[4] Whether the modified magnetism is due to strong anisotropy or due to disappearing of the spiral spin ordering with higher spin concentration at the Bi-position requires further investigations.

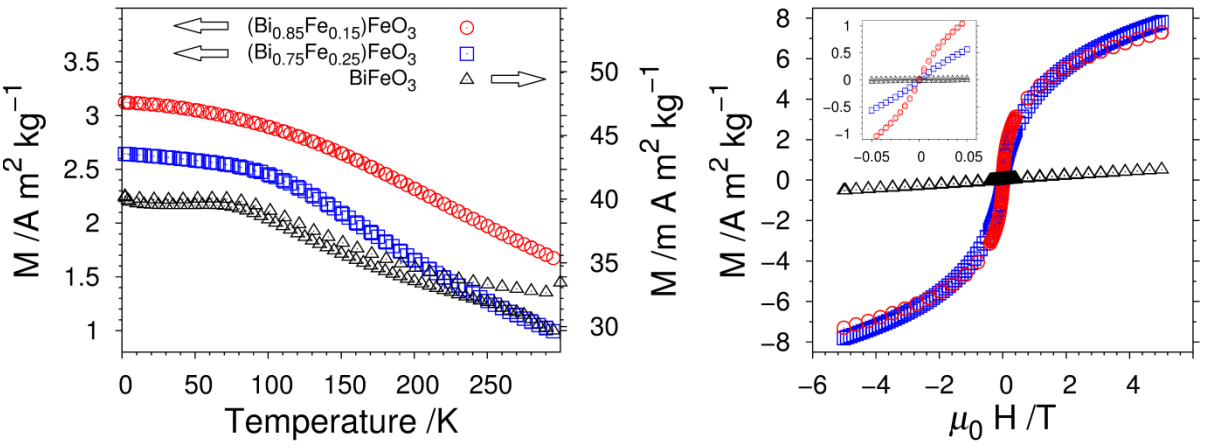

Figure 11. Left panel: Temperature-dependent Fc (0.1 T; cooling and heating) magnetization of $(Bi_{0.85}Fe_{0.15})FeO_3$, $(Bi_{0.75}Fe_{0.25})FeO_3$ and $BiFeO_3$. Right panel: Magnetic hysteresis curves of $(Bi_{0.85}Fe_{0.15})FeO_3$, $(Bi_{0.75}Fe_{0.25})FeO_3$ and $BiFeO_3$ with magnification (inset).

4. Conclusion

The SQUID data and the Mössbauer analysis showed that $(Bi_{0.85}Fe_{0.15})FeO_3$ and $(Bi_{0.75}Fe_{0.25})FeO_3$ show superparamagnetic behaviour. Since both samples are superparamagnetic between 2 K and 300 K it is unlikely that spin ordering occurs above 300 K. As such, the drop of thermal expansion coefficients above 400 K may be associated with the diffusion (Fe) led disordering of the Bi/Fe sites. Moreover, since ferroelectricity and magnetism in these materials are driven by the Bi and Fe sites, respectively, any ferroelectric into paraelectric phase transition can involve significant changes of the Bi/Fe dynamics, leading to axial strong anharmonicity. The consequent compensation may develop volumetric thermal expansion minima as seen at about 400 K. However, this assumption cannot exclude the nano-sized surface effect for phonon anharmonicity. Nevertheless, a clear picture can be found when the magnetic susceptibility can be analyzed at high temperatures.

Acknowledgement

We gratefully acknowledge the magnetic measurements of Dr. Serhiy Demeshko and Prof. Dr. Franc Meyer (University of Göttingen). NPD was conducted at ORNL's Spallation Neutron Source sponsored by the Scientific User Facilities Division, Office of Basic Energy Sciences, US Department of Energy. We thank University of Bremen for the financial support for A.K and MMM.

References

(1) Catalan, G.; Scott, J. F. Physics and Applications of Bismuth Ferrite. *Adv. Mater.* **2009**, *21* (24), 2463–2485.

(2) Park, J.-G.; Le, M. D.; Jeong, J.; Lee, S. Structure and Spin Dynamics of Multiferroic $BiFeO_3$. *J. Phys. Condens. Matter* **2014**, *26* (43), 433202.

(3) Fischer, P.; Polomska, M.; Sosnowska, I.; Szymanski, M. Temperature Dependence of the Crystal and Magnetic Structures of $BiFeO_3$. *J. Phys. C Solid State Phys.* **1980**, *13* (10), 1931–1940.

(4) Sosnowska, I.; Neumaier, T. P.; Steichele, E. Spiral Magnetic Ordering in Bismuth Ferrite. *J. Phys. C Solid State Phys.* **1982**, *15*, 4835–4846.

(5) Ederer, C.; Spaldin, N. A. Influence of Strain and Oxygen Vacancies on the Magnetoelectric Properties of Multiferroic Bismuth Ferrite. *Phys. Rev. B* **2005**, *71* (22), 224103.

(6) Park, T.; Papaefthymiou, G. C.; Viescas, A. J.; Moodenbaugh, A. R.; Wong, S. S. Size-Dependent Magnetic Properties of Single-Crystalline Multiferroic $BiFeO_3$ Nanoparticles. *Nano Lett.* **2007**, *7* (3), 766–772.

(7) Ravindran, P.; Vidya, R.; Kjekshus, A.; Fjellvåg, H.; Eriksson, O. Theoretical Investigation of Magnetoelectric Behavior in $BiFeO_3$. *Phys. Rev. B* **2006**, *74* (22), 224412.

(8) Ruette, B.; Zvyagin, S.; Pyatakov, A. P.; Bush, A.; Li, J. F.; Belotelov, V. I.; Zvezdin, A. K.; Viehland, D. Magnetic-Field-Induced Phase Transition in $BiFeO_3$ Observed by High-Field Electron Spin Resonance: Cycloidal to Homogeneous Spin Order. *Phys. Rev. B* **2004**, *69* (6), 64114.

(9) Moreau, J. M.; Michel, C.; Gerson, R.; James, W. J. Ferroelectric $BiFeO_3$ X-Ray and Neutron Diffraction Study. *J. Phys. Chem. Solids* **1971**, *32*, 1315–1320.

(10) Huang, F.; Wang, Z.; Lu, X.; Zhang, J.; Min, K.; Lin, W.; Ti, R.; Xu, T.; He, J.; Yue, C.; et al. Peculiar Magnetism of $BiFeO_3$ Nanoparticles with Size Approaching the Period of the Spiral Spin Structure. *Sci. Rep.* **2013**, *3* (1), 2907.

(11) Jia, C.-L.; Jin, L.; Wang, D.; Mi, S.-B.; Alexe, M.; Hesse, D.; Reichlova, H.; Marti, X.; Bellaiche, L.; Urban, K. W. Nanodomains and Nanometer-Scale Disorder in Multiferroic Bismuth Ferrite Single Crystals. *Acta Mater.* **2015**, *82*, 356–368.

(12) Kalinin, S. V; Suchomel, M. R.; Davies, P. K.; Bonnell, D. A. Potential and Impedance Imaging of Polycrystalline $BiFeO_3$ Ceramics. *J. Am. Ceram. Soc.* **2002**, *85* (12), 3011–3017.

(13) Wang, J.; Neaton, J. B.; Zheng, H.; Nagarajan, V.; Ogale, S. B.; Liu, B.; Viehland, D.; Schlom, D. G.; Waghmare, U. V.; Spaldin, N. A.; et al. Epitaxial BiFeO3 Multiferroic Thin Film Heterostructures. *Science* **2003**, *299*, 1719–1722.

(14) Kirsch, A.; Murshed, M. M.; Gaczynski, P.; Becker, K.-D.; Gesing, T. M. $Bi_2Fe_4O_9$: Structural Changes from Nano- to Micro-Crystalline State. *Zeitschrift für Naturforsch. B J. Chem. Sci.* **2016**, *71* (5), 447–455.

(15) Murshed, M. M.; Zhao, P.; Fischer, M.; Huq, A.; Alekseev, E. V.; Gesing, T. M. Thermal Expansion Modeling of Framework-Type Na[AsW_2O_9] and K[AsW_2O_9]. *Mater. Res. Bull.* **2016**, *84*, 273–282.
(16) Murshed, M. M.; Mendive, C. B.; Curti, M.; Šehović, M.; Friedrich, A.; Fischer, M.; Gesing, T. M. Thermal Expansion of Mullite-Type $Bi_2Al_4O_9$: A Study by X-Ray Diffraction, Vibrational Spectroscopy and Density Functional Theory. *J. Solid State Chem.* **2015**, *229*, 87–96.
(17) Murshed, M. M.; Mendive, C. B.; Curti, M.; Nénert, G.; Kalita, P. E.; Lipinska, K.; Cornelius, A. L.; Huq, A.; Gesing, T. M. Anisotropic Lattice Thermal Expansion of $PbFeBO_4$: A Study by X-Ray and Neutron Diffraction, Raman Spectroscopy and DFT Calculations. *Mater. Res. Bull.* **2014**, *59*, 170–178.
(18) Murshed, M. M.; Šehović, M.; Fischer, M.; Senyshyn, A.; Schneider, H.; Gesing, T. M. Thermal Behavior of Mullite between 4 K and 1320 K. *J. Am. Ceram. Soc.* **2017**, *100* (11), 5259–5273.
(19) Murshed, M. M.; Gesing, T. M. Anisotropic Thermal Expansion and Anharmonic Phonon Behavior of Mullite-Type $Bi_2Ga_4O_9$. *Mater. Res. Bull.* **2013**, *48* (9), 3284–3291.
(20) Gesing, T. M.; Fischer, R. X.; Burianek, M.; Mühlberg, M.; Debnath, T.; Rüscher, C. H.; Ottinger, J.; Buhl, J.-C.; Schneider, H. Synthesis and Properties of Mullite-Type $(Bi_{1-x}Sr_x)_2(M1_{1-y}M2_y)_4O_{9-x}$ (M=Al, Ga, Fe). *J. Eur. Ceram. Soc.* **2011**, *31* (16), 3055–3062.
(21) Massa, W. *Kristallstrukturbestimmung*, 7. Auflage.; Springer Verlag, 2011.
(22) Larson, A. C.; Von Dreele, R. B. General Structure Analysis System (GSAS), 2004, 86–748.
(23) Toby, B. H. EXPGUI , a Graphical User Interface for GSAS. *Journal of Applied Crystallography*, 2001, *34*, 210–213.
(24) Klencsár, Z. MossWinn 4.0 Manual.
(25) Liu, T.; Xu, Y.; Zhao, J. Low-Temperature Synthesis of $BiFeO_3$ via PVA Sol-Gel Route. *J. Am. Ceram. Soc.* **2010**, *93* (11), 3637–3641.
(26) Chen, J.-C.; Wu, J.-M. Dielectric Properties and Ac Conductivities of Dense Single-Phased $BiFeO_3$ Ceramics. *Appl. Phys. Lett.* **2007**, *91* (18), 182903.
(27) Da Silva, K. L.; Menzel, D.; Feldhoff, A.; Kübel, C.; Bruns, M.; Paesano, A.; Düvel, A.; Wilkening, M.; Ghafari, M.; Hahn, H.; et al. Mechanosynthesized $BiFeO_3$ Nanoparticles with Highly Reactive Surface and Enhanced Magnetization. *J. Phys. Chem. C* **2011**, *115* (15), 7209–7217.
(28) Kraus, W.; Nolze, G. POWDER CELL – a Program for the Representation and Manipulation of Crystal Structure and Calculation of the Resulting X-Ray Powder Patterns. *J. Appl. Crystallogr.* **1996**, *29* (3), 301–303.
(29) Shannon, R. D. Revised Effective Ionic Radii and Systematic Studies of Interatomie Distances in Halides and Chalcogenides. *Acta Crystallogr.* **1976**, *A32*, 751–767.
(30) Palewicz, a; Sosnowska, I.; Przeniosło, R.; Hewat, a W. $BiFeO_3$ Crystal Structure at Low Temperatures. *Acta Phys. Pol. A* **2010**, *117* (2), 296–301.
(31) Palewicz, A.; Przeniosło, R.; Sosnowska, I.; Hewat, A. W. Atomic Displacements in $BiFeO_3$ as a Function of Temperature: Neutron Diffraction

Study. *Acta Crystallogr. Sect. B Struct. Sci.* **2007**, *63* (4), 537–544.
(32) Wang, X.; Liebau, F. Influence of Polyhedron Distortions on Calculated Bond-Valence Sums for Cations with One Lone Electron Pair. *Acta Crystallogr. Sect. B Struct. Sci.* **2007**, *63* (2), 216–228.
(33) Robinson, K.; Gibbs, G. V.; Ribbe, P. H. Quadratic Elongation: A Quantitative Measure of Distortion in Coordination Polyhedra. *Science* **1971**, *172*, 567–570.
(34) Lonsdale, K. Vibration Amplitudes of Atoms in Cubic Crystals. *Acta Crystallogr.* **1948**, *1* (3), 142–149.
(35) Kallaev, S. N.; Mitarov, R. G.; Omarov, Z. M.; Gadzhiev, G. G.; Reznichenko, L. A. Heat Capacity of $BiFeO_3$-Based Multiferroics. *J. Exp. Theor. Phys.* **2014**, *118* (2), 279–283.
(36) Delaire, O.; Stone, M. B.; Ma, J.; Huq, A.; Gout, D.; Brown, C.; Wang, K. F.; Ren, Z. F. Anharmonic Phonons and Magnons in $BiFeO_3$. *Phys. Rev. B* **2012**, *85* (6), 64405.
(37) Hermet, P.; Goffinet, M.; Kreisel, J.; Ghosez, P. Raman and Infrared Spectra of Multiferroic Bismuth Ferrite from First Principles. *Phys. Rev. B* **2007**, *75* (22), 220102.
(38) Murad, E. Mössbauer Spectroscopy of Clays, Soils and Their Mineral Constituents. *Clay Miner.* **2010**, *45* (4), 413–430.
(39) Burns, R. G. Mineral Mössbauer Spectroscopy : Correlations between Chemical Shift and Quadrupole Splitting Parameters. *Hyperfine Interact.* **1994**, *91*, 739–745.
(40) Zhang, X.; Niu, Y.; Meng, X.; Li, Y.; Zhao, J. Structural Evolution and Characteristics of the Phase Transformations between α-Fe_2O_3, Fe_3O_4 and γ-Fe_2O_3 Nanoparticles under Reducing and Oxidizing Atmospheres. *CrystEngComm* **2013**, *15* (40), 8166–8172.
(41) Zakharova, I. N.; Shipilin, M. A.; Alekseev, V. P.; Shipilin, A. M. Mössbauer Study of Maghemite Nanoparticles. *Tech. Phys. Lett.* **2012**, *38* (1), 55–58.
(42) Ramos Guivar, J. A.; Bustamante, A.; Flores, J.; Mejía Santillan, M.; Osorio, A. M.; Martínez, A. I.; De Los Santos Valladares, L.; Barnes, C. H. W. Mössbauer Study of Intermediate Superparamagnetic Relaxation of Maghemite (γ-Fe_2O_3) Nanoparticles. *Hyperfine Interact.* **2014**, *224* (1–3), 89–97.
(43) Ayyub, P.; Multani, M.; Barma, M.; Palkar, V. R.; Vijayaraghavan, R. Size-Induced Structural Phase Transitions and Hyperfine Properties of Microcrystalline Fe_2O_3. *J. Phys. C Solid State Phys.* **1988**, *21* (11), 2229–2245.
(44) Kistner, O. C.; Sunyar, A. W. Evidence for Quadrupole Interaction of Fe57m,and Influence of Chemical Binding on Nuclear Gamma-Ray Energy. *Phys. Rev. Lett.* **1960**, *4*, 412–415.
(45) Blaauw, C.; van der Woude, F. Magnetic and Structural Properties of $BiFeO_3$. *J. Phys. C Solid State Phys.* **1973**, *6*, 1422–1431.
(46) Vijayanand, S.; Mahajan, M. B.; Potdar, H. S.; Joy, P. A. Magnetic Characteristics of Nanocrystalline Multiferroic BiFeO3 at Low Temperatures. *Phys. Rev. B* **2009**, *80* (6), 64423.
(47) Mazumder, R.; Devi, P. S.; Bhattacharya, D.; Choudhury, P.; Sen, A.; Raja, M. Ferromagnetism in Nanoscale $BiFeO_3$. *Appl. Phys. Lett.* **2007**, *91*, 62510-1–3.

(48) Mocherla, P. S. V; Karthik, C.; Ubic, R.; Ramachandra Rao, M. S.; Sudakar, C. Effect of Microstrain on the Magnetic Properties of $BiFeO_3$ Nanoparticles. *Appl. Phys. Lett.* **2014**, *105* (13), 132409.

(49) Wang, X.; Zhang, Y.; Wu, Z. Magnetic and Optical Properties of Multiferroic Bismuth Ferrite Nanoparticles by Tartaric Acid-Assisted Sol–gel Strategy. *Mater. Lett.* **2010**, *64* (3), 486–488.

(50) Lopes, A. M. L.; Araújo, J. P.; Ferdov, S. Room Temperature Synthesis of $Bi_{25}FeO_{39}$ and Hydrothermal Kinetic Relations between Sillenite- and Distorted Perovskite-Type Bismuth Ferrites. *Dalt. Trans.* **2014**, *43* (48), 18010–18016.

(51) Ortiz-Quiñonez, J. L.; Díaz, D.; Zumeta-Dubé, I.; Arriola-Santamaría, H.; Betancourt, I.; Santiago-Jacinto, P.; Nava-Etzana, N. Easy Synthesis of High-Purity $BiFeO_3$ Nanoparticles: New Insights Derived from the Structural, Optical, and Magnetic Characterization. *Inorg. Chem.* **2013**, *52* (18), 10306–10317.

(52) Guria, A. K.; Dey, K.; Sarkar, S.; Patra, B. K.; Giri, S.; Pradhan, N. Tuning the Growth Pattern in 2D Confinement Regime of Sm_2O_3 and the Emerging Room Temperature Unusual Superparamagnetism. *Sci. Rep.* **2014**, *4* (1), 6514.

Supporting information

Temperature-dependent structural and spectroscopic studies of $(Bi_{1-x}Fe_x)FeO_3$

Andrea Kirsch[a,b], M. Mangir Murshed[a,b*], Melanie J. Kirkham[c], Ashfia Huq[c], F. Jochen Litterst[d], Thorsten M. Gesing[a,b]

[a]University of Bremen, Institute of Inorganic Chemistry and Crystallography, Leobener Straße 7, D-28359, Bremen, Germany

[b]University of Bremen, MAPEX center for materials and processes, Bibliothekstraße 1, D-28359 Bremen, Germany

[c]Chemical and Engineering Materials Division, Oak Ridge National Laboratory, Oak Ridge, Tennessee 37831, USA

[d]Institute for Condensed Matter Physics, Technische Universität Braunschweig, Mendelssohnstr. 3, D-38106 Braunschweig, Germany

*Corresponding author; e-mail address: murshed@uni-bremen.de; phone: +49 (0)421 218 63144; fax: +49 (0)421 218 63144

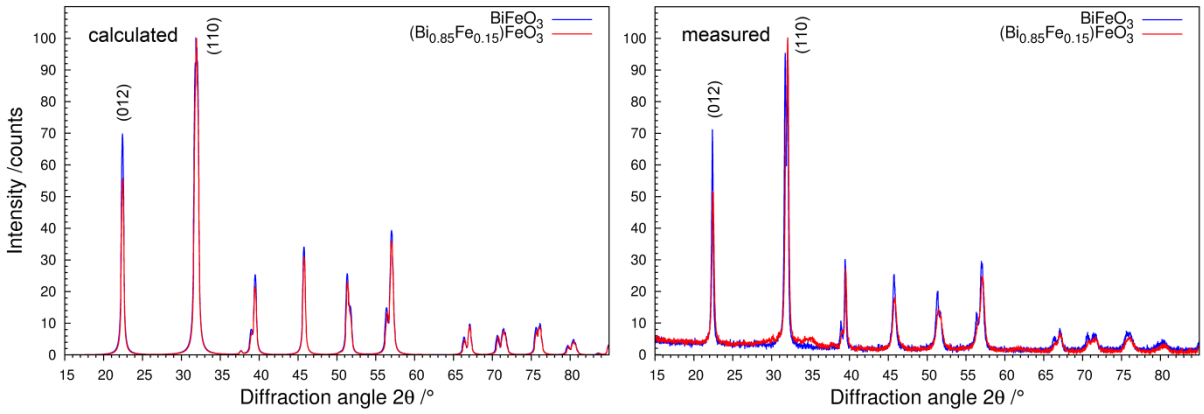

Figure 1S. Simulated (left panel) and measured (right panel) X-ray powder patterns of $BiFeO_3$ and $(Bi_{1-x}Fe_x)FeO_3$. The program POWDER CELL[1] was used for simulations and the data was normalized to the (*110*) reflection.

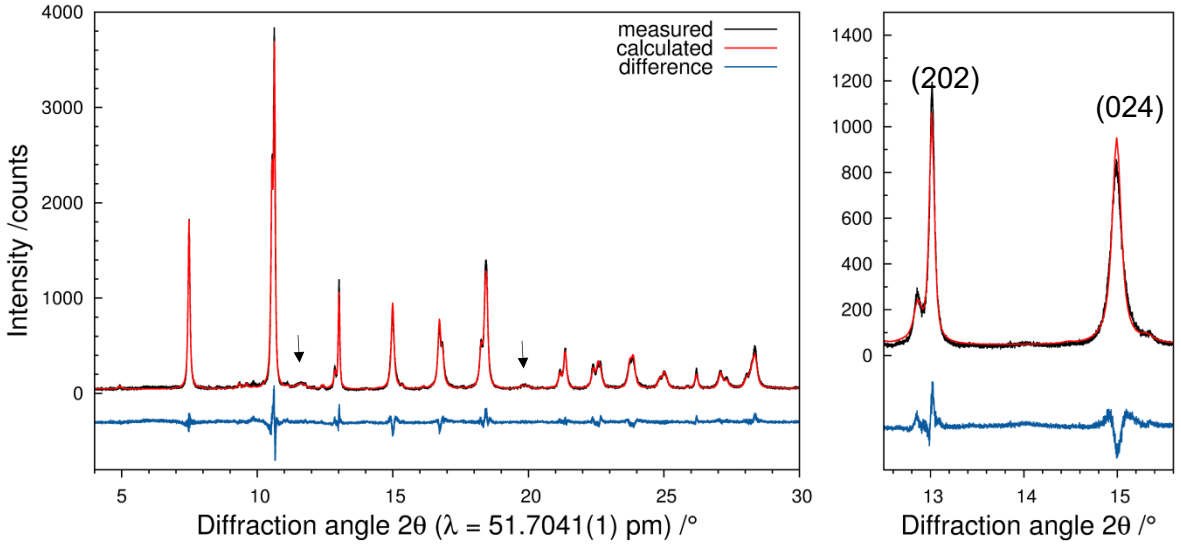

Figure 2S. Rietveld patterns of $(Bi_{0.85}Fe_{0.15})FeO_3$ for the synchrotron X-ray data (APS). The magnification (right) shows the huge anisotropy of two neighbouring reflections.

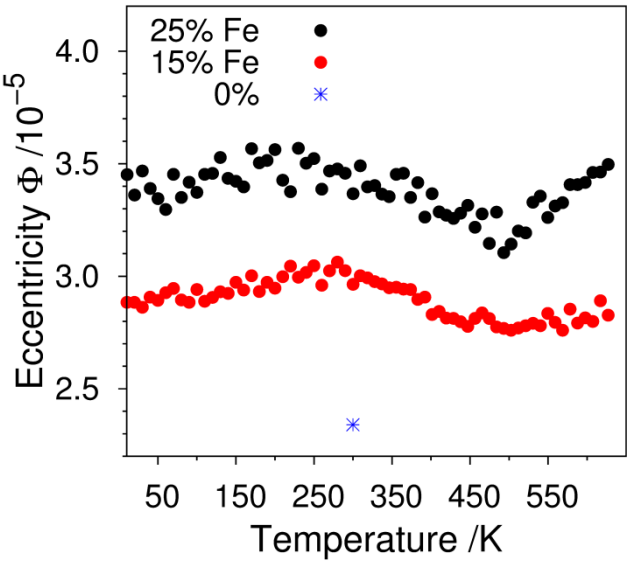

Figure 3S. Temperature-dependent Wang-Liebau eccentricity (WLE) parameter of the (Bi/Fe)O_6 octahedra of ($Bi_{1-x}Fe_x$)FeO_3 and room-temperature value of the BiO_6 octahedra of $BiFeO_3$.

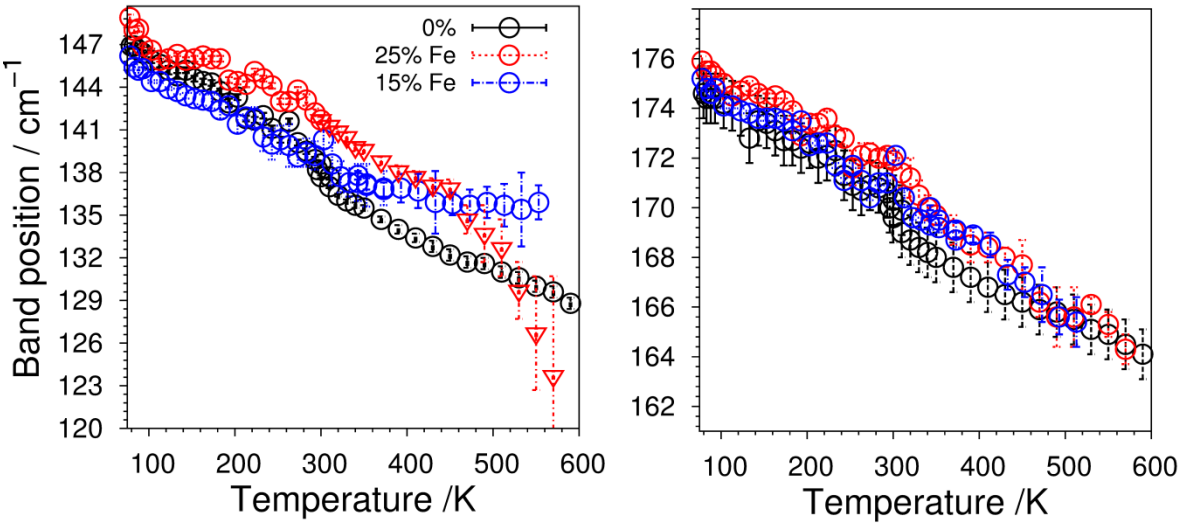

Figure 4S. Temperature-dependent band positions of the E(TO2) and A_1(TO1) modes of ($Bi_{1-x}Fe_x$)FeO_3 for x = 0, 0.15 and 0.25.

Table 1S. Raman frequency of mode E(TO2) and A_1(TO1) at 0 K (obtained from extrapolation of the low-temperature data) along with respective Grüneisen parameter (γ_i).

Compound	E(TO2)		A_1(TO1)	
	$\omega_{i,0}$ /cm^{-1}	γ_i	$\omega_{i,0}$ /cm^{-1}	γ_i
$BiFeO_3$[2]	135.7	1.94	168.9	1.74
$(Bi_{0.85}Fe_{0.15})FeO_3$	141.7(1)	8.9(3)	171.3	4.6(3)
$(Bi_{0.75}Fe_{0.25})FeO_3$	140.9(1)	6.8(2)	171.3	4.1(2)

Table 2S. Elastic coefficients (C_{ij}) and bulk moduli of $BiFeO_3$.

Method	C_{11}	C_{12}	C_{13}	C_{14}	C_{33}	C_{44}	C_{66}	B_R	B_V	B_H	B_0	Ref.
IXA	207(5)	-	-	-	159(4)	30(1)	42(1)	-	-	-	-	[3]
LDA	249	-	75	9	160	44	49	-	-	-	-	[3]
GGA	203	117	50	23	129	31	43	96	108	102	-	[4]
GGA + U (3 V)	213	111	49	19	139	39	51	99	109	104	-	[4]
GGA + (U 6 V)	222	110	50	16	150	49	56	104	113	108	-	[4]
XRPD	-	-	-	-	-	-	-	-	-	-	97.3(7)	[5]
XRPD	-	-	-	-	-	-	-	-	-	-	75(15)	[6]

IXA = Inelastic X-ray, B_0 = Bulk modulus (Reuss), B_R = Bulk modulus (Reuss), B_V = Bulk modulus (Voigt), B_H = Bulk modulus (Hill average)

References

(1) Kraus, W.; Nolze, G. *J. Appl. Crystallogr.* **1996**, *29* (3), 301–303.

(2) Yang, Y.; Sun, J. Y.; Zhu, K.; Liu, Y. L.; Chen, J.; Xing, X. R. *Phys. B Condens. Matter* **2009**, *404* (1), 171–174.

(3) Borissenko, E.; Goffinet, M.; Bosak, A.; Rovillain, P.; Cazayous, M.; Colson, D.; Ghosez, P.; Krisch, M. *J. Phys. Condens. Matter* **2013**, *25* (10).

(4) Shang, S. L.; Sheng, G.; Wang, Y.; Chen, L. Q.; Liu, Z. K. *Phys. Rev. B - Condens. Matter Mater. Phys.* **2009**, *80* (5), 52102-1–4.

(5) Zhu, J. L.; Feng, S. M.; Wang, L. J.; Jin, C. Q.; Wang, X. H.; Li, L. T.; Li, Y. C.; Li, X. D.; Liu, J. *High Press. Res.* **2010**, *30* (2), 265–272.

(6) Gavriliuk, A. G.; Struzhkin, V. V.; Lyubutin, I. S.; Ovchinnikov, S. G.; Hu, M. Y.; Chow, P. *Phys. Rev. B - Condens. Matter Mater. Phys.* **2008**, *77* (15), 1–6.

Chapter 5

Nanoparticle Precursor Into Polycrystalline $Bi_2Fe_4O_9$: An Evolutionary Investigation of Structural, Morphological, Optical and Vibrational Properties

A published paper reprinted with permission from Kirsch, A.; Murshed, M. M.; Schowalter, M.; Rosenauer, A.; Gesing, T. M. Nanoparticle Precursor into Polycrystalline $Bi_2Fe_4O_9$: An Evolutionary Investigation of Structural, Morphological, Optical, and Vibrational Properties. *J. Phys. Chem C* **2016**, *120*, 18831–18840.

https://pubsdc3.acs.org/doi/full/10.1021/acs.jpcc.6b04773

Andrea Kirsch[a], M. Mangir Murshed[a*], Marco Schowalter[b], Andreas Rosenauer[b,c], Thorsten M. Gesing[a,c]

[a]Institute of Inorganic Chemistry and Crystallography, University of Bremen, Leobener Straße/NW2, D-28359, Bremen, Germany

[b]Institute of Solid State Physics, University of Bremen, Otto-Hahn-Allee /NW1, D-28359 Bremen, Germany

[c]MAPEX center for materials and processes, University of Bremen, Bibliothekstraße 1, D-28359 Bremen, Germany

*Corresponding author; e-mail address: murshed@uni-bremen.de; phone: +49 (0)421 218 63144; fax: +49 (0)421 218 63144

ABSTRACT: Mullite-type $Bi_2Fe_4O_9$ was synthesized using a polyol-mediated method. X-ray powder diffraction (XRD) revealed that the as-synthesized sample is nanocrystalline. It transformed into a rhombohedral perovskite-type $BiFeO_3$ followed by a second transformation into mullite-type $Bi_2Fe_4O_9$ during heating. Each structural feature, from as-synthesized into crystalline phase, was monitored through temperature-dependent XRD in situ. The locally resolved high resolution transmission electron micrographs revealed that the surface of some heated samples is covered by 4 − 13 nm sized particles which were identified from the lattice fringes as crystalline $Bi_2Fe_4O_9$. XRD and Raman spectra demonstrate that the nucleation of both $BiFeO_3$ and $Bi_2Fe_4O_9$ might simultaneously commence; however, their growth and ratios are dependent on temperature. The diffuse UV/Vis reflectance spectra showed fundamental absorption edges between 1.80(1) and 2.75(3) eV. A comparative study between the “derivation of absorption spectrum fitting method” (DASF) and the Tauc method suggests $Bi_2Fe_4O_9$ to be a direct band gap semiconductor.

1. INTRODUCTION

Perovskite-type $BiFeO_3$ and mullite-type $Bi_2Fe_4O_9$ are known to show interesting optic,[1] electronic,[2] catalytic,[3] and magnetic[4] properties as well as crystal chemistry[5−8] and temperature-dependent behaviors.[9] Both these compounds can be synthesized through a variety of synthesis methods including solid state reaction method,[10] chemical coprecipitation route,[2] sol−gel method,[11,12] EDTA route,[13,14] combustion method,[15] and hydrothermal process.[16] The widely studied $BiFeO_3$ has a Néel temperature of ∼640 K and a ferroelectric Curie temperature of ∼1100 K.[17] A spontaneous polarization is caused by the centrosymmetric distortion of the Bi^{3+} and Fe^{3+} cations along the pseudocubic threefold [111] axis.[18] Beside its well-known multiferroic properties at room temperature, it is also studied due to its photocatalytic activity in the visible range of light.[12,19] The crystal structure of $BiFeO_3$ can be described as a rhombohedrally distorted perovskite in space group R3c and Z = 6 as shown in Figure 1. Until now, there exists no common agreement in the literature whether the optical band gap of $BiFeO_3$ possesses a direct or an indirect transition.[15] The direct band gap was reported to be within 2.1 − 2.8 eV[15,20−22] and the indirect one to be within 2.1 − 2.2 eV.[19,23] $Bi_2Fe_4O_9$ is also known to exhibit photocatalytic properties in the visible range.[13] Centrosymmetric multiferroic properties near room

temperature are reported,[24,25] which triggers considerable debates. This compound crystallizes in the orthorhombic space group *Pbam* with Z = 2 and shows the characteristic mullite-type feature of edge-sharing FeO_6 octahedra running parallel to the c-axis. These chains are cross-linked by corner-sharing FeO_4 double-tetrahedra. Between the chains the Bi atoms are located, where the $6s^2$ lone electron pairs (LEPs) of Bi^{3+} point toward the vacant sites of the structure.[9] Like $BiFeO_3$, the nature of the optical transition of $Bi_2Fe_4O_9$ is also not yet clear. The direct transitions were reported between 2.1 and 2.3 eV,[2,26] and the indirect ones from 1.9 to 2.1 eV.[16,27] Of particular note, the source of the observed second absorption edge is an ongoing topic of debate. Theoretical calculations suggested that $Bi_2Fe_4O_9$ is a direct multiband semiconductor and the second absorption edge is caused by the d−d-transitions between the Fe atoms.[3] In contrast, another theoretical study indicated that $Bi_2Fe_4O_9$ is an indirect semiconductor with a band gap of 1.23 eV,[28] and the second absorption edge is caused by intervalence charge transfer between randomly arranged Fe^{2+} and Fe^{3+} induced by uneven distributed negative charges.[28]

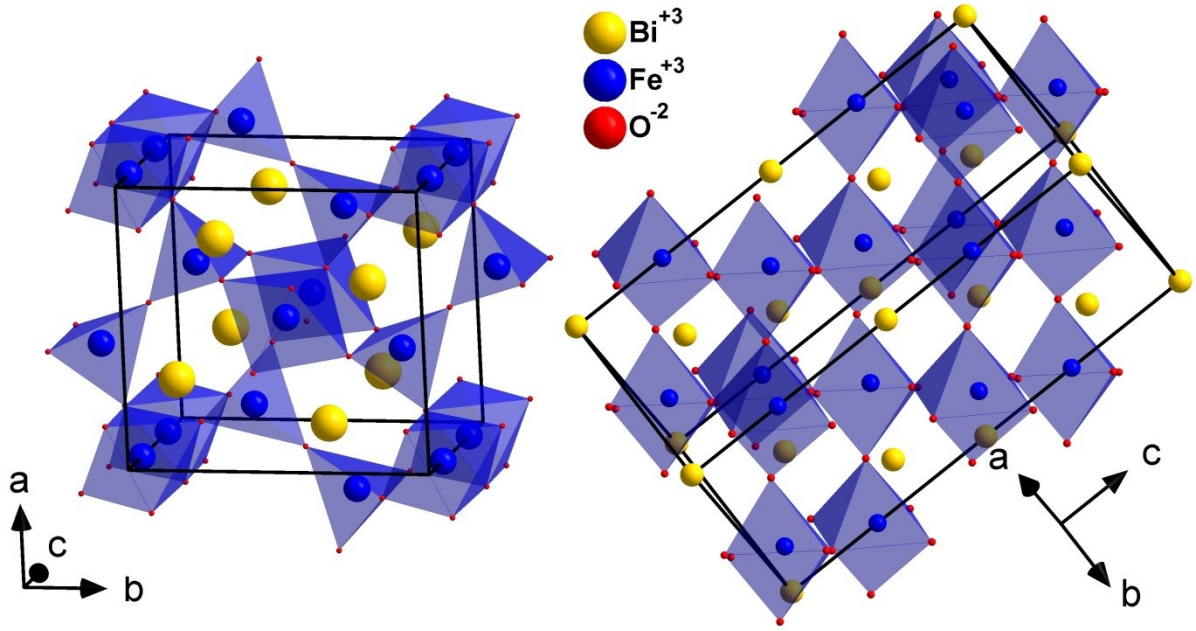

Figure 1. Crystal structures of mullite-type $Bi_2Fe_4O_9$ in space group *Pbam* (left) and perovskite-type $BiFeO_3$ in space group *R*3*c* (right).

Table 1. X-ray characterization of calcined samples prepared by polyol method.

Sample	Calcination temp. /K	Degree of crystallinity /%	Crystalline phase fraction /%				Crystallite size /nm	
			Bi_2O_3	Fe_2O_3	perovskite	Mullite-type	perovskite	Mullite-type
BFO	–	0	–	–	–	–	–	–
BFO/573	573	1(3)	100	–	–	–	–	–
BFO/623	623	2(3)	100	–	–	–	–	–
BFO/673	673	2(3)	100	–	–	–	–	–
BFO/723	723	3(3)	–	–	100	–	–	–
BFO/773	773	14(3)	6.6(9)	–	93.4(8)	–	13.2(4)	–
BFO/823	823	80(3)	–	–	77.6(7)	22.4(7)	25.1(6)	11.5(6)
BFO/873	873	84(3)	–	1.9(4)	32.6(3)	65.5(3)	41(1)	35.4(6)
BFO/923	923	100(3)	–	1.9(3)	3.4(1(	94.7(3)	65(6)	59.5(9)
BFO/973	973	100(3)	–	2.0(3)	1.01(7)	97(3)	–	73(1)
BFO/1023	1023	100(3)	–	2.6(3)	–	97.4(3)	–	129(2)

Smaller crystallites of $Bi_2Fe_4O_9$ [1] and $BiFeO_3$ [23] exhibit higher photocatalytic activities. Moreover, an unexpected red shift of the band gap was observed in $BiFeO_3$ with decreasing crystallite sizes.[29] The polyol method[30,31] is suitable to produce larger quantities of nanocrystalline samples. In the case of the photocatalytic active semiconductor TiO_2, anatase is the active polymorph, but a mixture of rutile and anatase (e.g.,1:3.4) is more active than pure nanocrystalline anatase powder.[32] Hurum et al.[33] concluded that the mixed samples consisted of nanoclusters with atypically small rutile crystallites interwoven with anatase crystallites. So a rapid electron transfer from rutile to anatase takes place at phase boundaries leading to an effective charge separation. Since $BiFeO_3$ and $Bi_2Fe_4O_9$ could be simultaneously crystallized,[11,25,34] their suitable mixture could be more active than either pure $BiFeO_3$ or $Bi_2Fe_4O_9$ sample. In this study, $Bi_2Fe_4O_9$ samples were synthesized by the polyol method. By subsequent heating, samples with various $BiFeO_3$: $Bi_2Fe_4O_9$ ratios and crystallite sizes were produced. They were characterized by SEM, TEM, FTIR, diffuse UV/Vis reflectance spectroscopy, Raman spectroscopy, and XRD. Furthermore, the precursor over perovskite-type to mullite-type transformation was studied via in situ temperature-dependent X-ray diffraction. A comparative study was performed between the “derivation of absorption spectrum fitting method” (DASF) and the commonly used Tauc method for the calculation of both direct and indirect band gaps.

2. EXPERIMENTAL SECTION

2.1. Synthesis

The precursor was synthesized by a polyol mediated synthesis.[30] Both 5 mmol $Bi(NO_3)_3 \cdot 5H_2O$ (Sigma-Aldrich, ≥ 98%) and 10 mmol $Fe(NO_3)_3 \cdot 9H_2O$ (Sigma-Aldrich, ≥ 98%) were dissolved into 42 mL of diethylene glycol (AppliChem, 99%). The mixture was put into a three-necked flask which was then heated in a metal bath at 423 K under reflux. After 2 h the mixture was cooled down to room temperature and washed several times with acetone. The as-synthesized powder (BFO) was then heated for 2 h from 573 to 1023 K at every 50 K (BFO/#) to produce different crystallite sizes and phase ratios as given in Table 1.

2.2. Electron Microscopy

The scanning electron microscopy (SEM) measurements were carried out on a JSM-6510 (JEOL GmbH, Munich, Germany) equipped with energy dispersive X-ray (EDX) analysis facilities and an XFlash Detector 410-M (Bruker AXS GmbH, Karlsruhe, Germany) at 20 kV. TEM measurements were carried out on a Titan 80/300 kV (FEI Europe, Eindhoven, The Netherlands) equipped with a Cs corrector for the spherical aberration of the objective lens. The microscope was operated at 300 kV during all investigations. Specimen were prepared by dissolving the material in ethanol, pestling, and subsequent dispersion on copper grids covered with a thin holey amorphous carbon film.

2.3. X-ray Diffraction

X-ray powder diffraction data were collected on an X'Pert MPD PRO diffractometer (PANalytical GmbH, Almelo, The Netherlands) equipped with Ni-filtered $CuK_{\alpha 1,2}$ radiation ($\lambda\alpha 1,2$ = 0.154 06 nm, 0.154 44 nm) and a X'Celerator detector system in Bragg−Brentano geometry. Room-temperature scans were performed from 5 to 85° 2θ with a step width of 0.0167° 2θ and a measurement time of 275 s per step. An HTK 1200N heating chamber (Anton Paar, Graz, Austria) was used for the temperature-dependent investigations. Data were collected from 5 to 100° 2θ with a step width of 0.0167° 2θ and a measurement time of 75 s per step. The temperature was increased stepwise from 300 to 1120 K at 20 K steps with an equilibration time of 5 min. The obtained data were refined using the Rietveld method (TOPAS V4.2,

Bruker AXS). For profile fitting the fundamental parameter approach was used. The fundamental parameters were fitted against a LaB_6 standard material. The degree of crystallinity, crystalline phase ratios, as well as the crystallite sizes of the perovskite- and mullite-type structures of the synthesized samples are summarized in Table 1 (with estimated standard deviations given in the parentheses).

2.4. Spectroscopy

UV/Vis diffuse reflectance spectra were collected on a Shimadzu UV/Vis spectrophotometer UV-2600 equipped with an ISR-2600 plus two-detector integrating sphere. Barium sulfate was used as a reference. The data were collected from 200 to 1400 nm in 0.5 nm steps. Raman spectra were measured on a Horiba LabRam Aramis spectrometer equipped with a Laser of 785 nm, a slit of 100 µm, a hole of 1000 µm, and an exposure time of 2 s with 10 accumulations. Data were collected between 80 and 1200 cm^{-1} with a spectral resolution of approximately 1.1 cm^{-1} using a grating of 1800 grooves/mm. FTIR measurements were carried out with 128 scans from 370 to 4000 cm^{-1} using the KBr method (0.5 mg sample in 200 mg KBr). The band positions were fitted with TOPAS V4.2, Bruker AXS.

3. RESULTS AND DISCUSSION

3.1. SEM and HRTEM

The as-synthesized powder samples exhibit agglomerated particles showing more or less a uniform distribution of shapes and sizes. Analysis of 2D image allowed for calculation of the average particle size of around 286 ± 81 nm as shown in Figure 2.

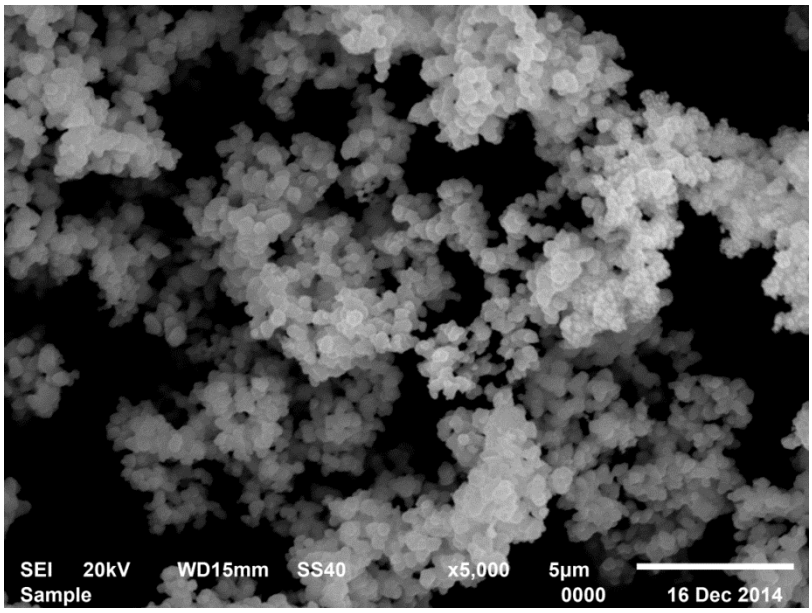

Figure 2. SEM micrograph of as-synthesized powder BFO (see Table 1).

HRTEM micrographs suggest that the as-synthesized powder is amorphous detected by selected area diffraction patterns, showing that at least some parts of the sample are crystalline as shown by the inset of Figure 3b. The symmetry appears to be the same as in the sample calcined at 823 K (inset Figure 3d). The surface of the samples is covered by very small particles of 4 − 13 nm. The fringe analysis of the sample BFO/873 confirms a mullite-type structure for those small particles as indicated by the d-spacing of 330(30) pm attributed to the (201) plane. This plane is particularly suitable to distinguish between the perovskite- and mullite-type structure since the former structure does not have d-spacings around this region. It is worth mentioning that during the measurements the shape and the facet of those small particles rearranged by the electron beam may due to electromagnetic interactions. Micrographs taken from the same particle clearly show this effect as given in Figure 4. This phenomenon was also observed by Ortiz-Quiñonez et al.,[15] which they attributed to a rearrangement through quasi-melt states. In our case, lattice fringes were visible over the full series of 10 images within the whole particle (Supporting Information, S1); the shape changes between the acquisition of the 10 images.

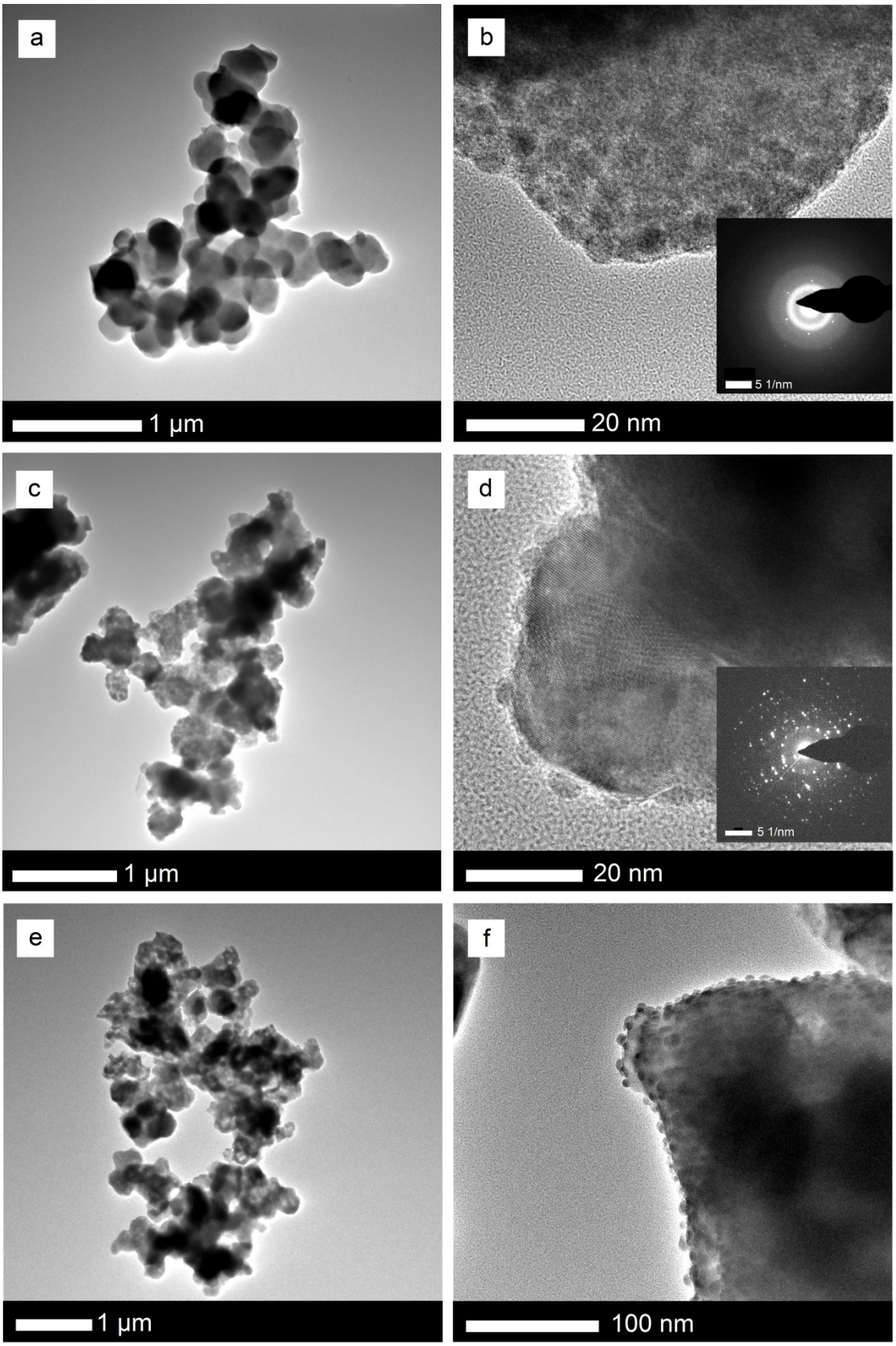

Figure 3. TEM micrographs of the as-synthesized sample BFO (a and b), calcined sample BFO/823 (c and d), and calcined sample BFO/873 (e and f). For detailed description of each sample, see Table 1.

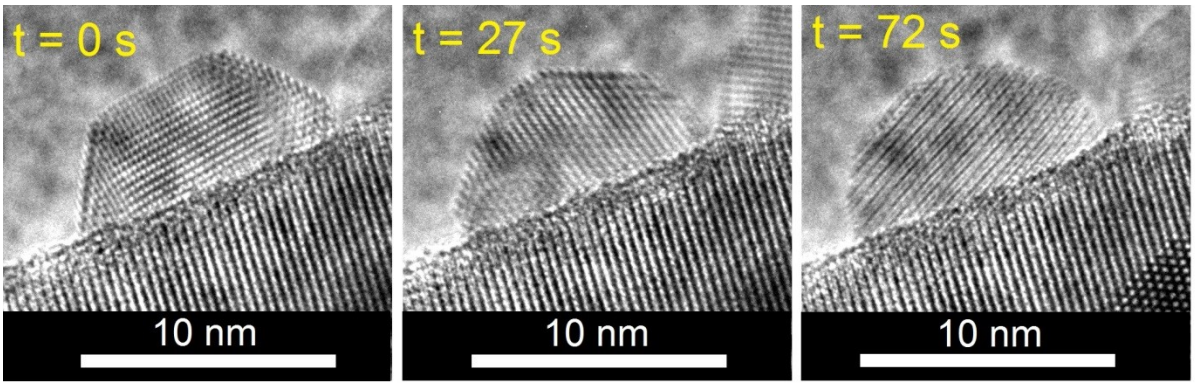

Figure 4. HRTEM micrographs of a surface nanoparticle of the sample BFO/873 (see Table 1) at three different points in time (from left to right t = 0 s; t = 27 s; t = 72 s).

3.2. X-ray Powder Diffraction

The diffraction pattern of the as-synthesized powder exhibits no distinct Bragg reflections indicating an X-ray amorphous phase. By fitting the pattern with single reflections constrained for the average crystallite size, a corresponding value of 0.9(1) nm could be estimated. The XRD patterns of the samples calcined at different temperatures (each for 2 h) are shown in Figure 5. With increasing calcination temperature the successive degree of crystallinity increases toward a saturation point (100% crystalline) started above 923 K as shown in Figure 6. Notably, 923 K is the observed temperature at which the mullite-type $Bi_2Fe_4O_9$ phase comprises more than 94% of the total crystalline composition.

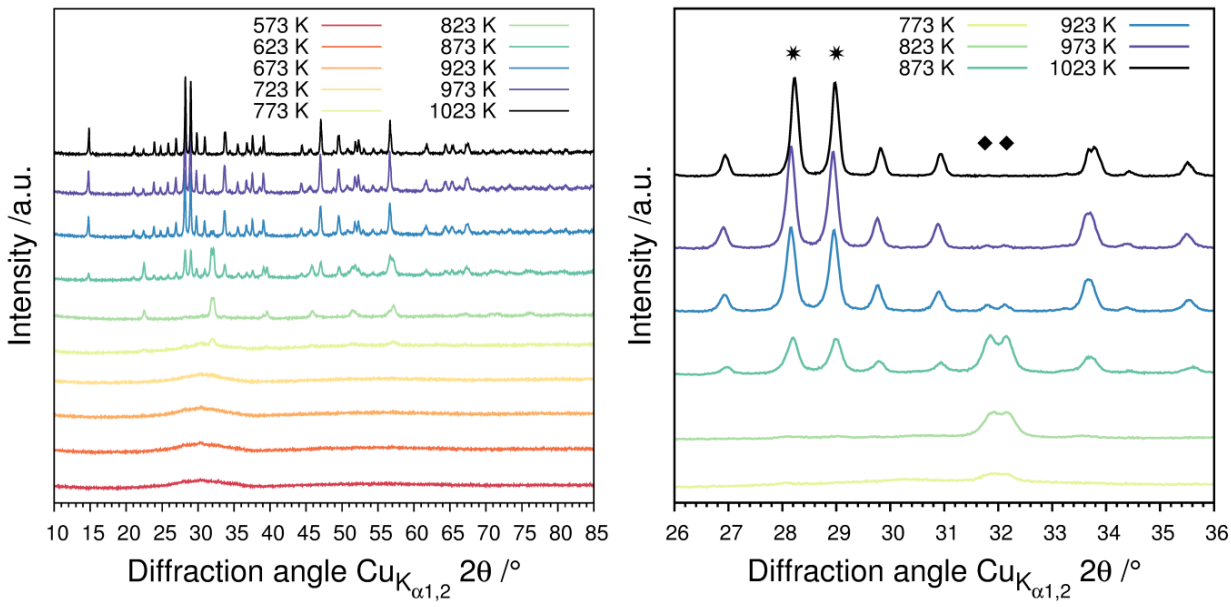

Figure 5. *Left panel*: X-ray powder diffraction patterns of samples calcined at different temperatures (see table 1 for details). *Right panel*: Magnified feature of a part of the left panel, showing some distinctive reflections of $BiFeO_3$ (diamond) and $Bi_2Fe_4O_9$ (star) structures.

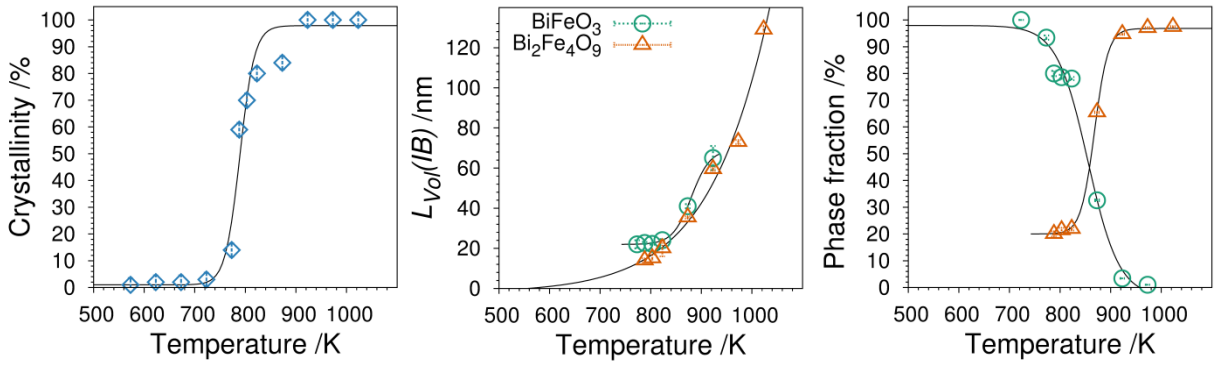

Figure 6. *Left panel:* Degree of crystallinity of the samples heated at 573 – 1023 K at every 50 K for 2 h. *Middle panel:* Crystallite sizes of $BiFeO_3$ and $Bi_2Fe_4O_9$. *Right panel:* Crystalline phase fraction of $BiFeO_3$ and $Bi_2Fe_4O_9$. The solid lines are for eye guidelines.

The XRD diffraction clearly shows that the perovskite structure first appeared at 723 K. The Rietveld refinement analyses demonstrate that the perovskite phase gradually increases with increasing temperature until 823 K followed by a decrease in phase fraction due to the transformation into the mullite-type $Bi_2Fe_4O_9$ structure. In the sample calcined at 1023 K, the perovskite-type structure was no longer detected. The average crystallite sizes of the $BiFeO_3$ perovskite - as well as of the mullite-type $Bi_2Fe_4O_9$ phase - increase with increasing temperature, showing sizes between

13.2(4) and 65(6) nm for perovskite, and 11.5(6) and 129(2) nm for mullite-type. Interestingly, the crystallite sizes of both phases increase very similarly. Throughout the ex situ XRD observation on the calcination process, two minor impurities were so far identified, namely, β-Bi_2O_3 and hematite (Fe_2O_3). The tetragonal β-Bi_2O_3 phase was only observed in samples calcined below 773 K, which disappeared at 823 K. However, the rhombohedral hematite exists as a minor phase (<3% phase fraction) in all samples calcined above 873 K. The in situ heating experiment (temperature increase by 20 K every 60 min) showed a transformation from the as-synthesized powder into the perovskite-type structure at 740 K followed by a second transformation into $Bi_2Fe_4O_9$ starting from 780 K on, as seen in Figure 7. At 860 K the perovskite structure cannot be detected anymore (see Figure 7). Note that the reflections above 40° 2θ showing up from 460 K on can be attributed to the sample holder due to shrinking of the powder.

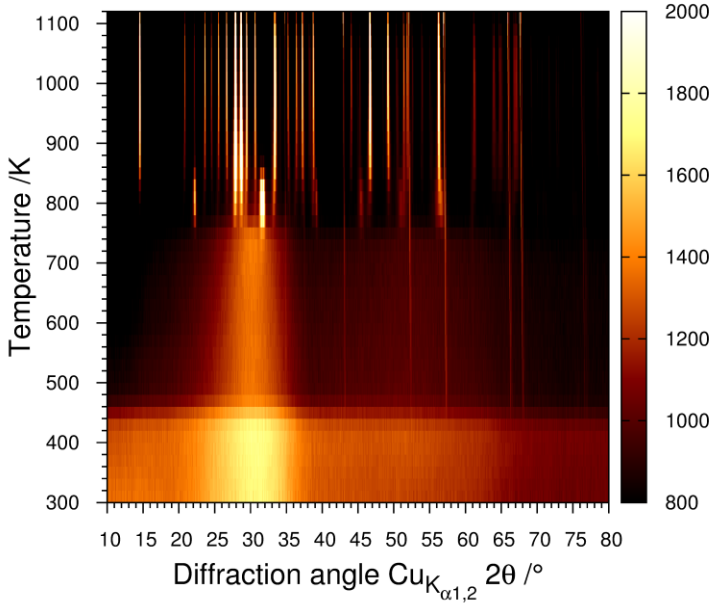

Figure 7. Temperature-dependent diffraction patterns showing the transformation from as-synthesized amorphous powder to rhombohedral $BiFeO_3$ and finally orthorhombic $Bi_2Fe_4O_9$.

Recent investigations[35] indicated a transformation of an as-synthesized polyol powder through ($(Bi_{1-x}Fe_x)FeO_3$) into polycrystalline $Bi_2Fe_4O_9$. It was evidenced by a smaller lattice parameter c with values of ~1379 pm at 780 K.[35] This was attributed to the substitution of Fe^{3+} on the Bi position (6*a* 0,0,0). Refinements performed in this study showed neither a smaller lattice parameter *c* (1393.2(4) pm at 780 K) nor Fe^{3+} and Bi^{3+} on the same position (6*a* 0,0,0). The Fe-bearing sillenite $Bi_{25}FeO_{39}$ phase

observed between 860 and 920 K[35] during the transformation of ($(Bi_{1-x}Fe_x)FeO_3$) into $Bi_2Fe_4O_9$ was also not identified in this study.

3.3. Spectroscopy

Diffuse Reflectance UV/Vis Spectroscopy

Diffuse reflectance UV/Vis spectroscopy is frequently used to determine the optical band gap of semiconductors. Therefore, the Tauc relationship[36] is most commonly used to estimate the band gap energy by finding the intercept of the abscissa from the following relation

$$\alpha(h\nu) \approx B(h\nu - E_g)^n \text{ (with } \alpha \sim F(R)) \quad (1)$$

where α is the extinction coefficient, h the Planck constant, ν the frequency of light, E_g the band gap energy in eV and n the nature of transition, that is, $n = 2$ for an indirect transition (plotted as $\alpha(h\nu)^{1/2}$ versus E) and $n = 1/2$ for a direct transition (plotted as $\alpha(h\nu)^2$ versus E), respectively. The Kubelka-Munk function is used to approximate the optical absorption from the reflectance:

$$F(R) = \frac{(1-R)^2}{2R} \quad (2)$$

Using the Tauc method it is necessary to have information about the nature of transition, so that the data can be properly treated. However, often this information is not available. Recently, the derivation of absorption spectrum fitting method (DASF) was demonstrated by Souri and Tahan[37] providing the opportunity to overcome this problem. They used the method to determine the optical band gap of thin films measured in transmission mode, which may fit to the powder samples measured in the reflectance mode. The DASF method is developed from the absorption spectrum fitting method (ASF method) as:

$$A(\lambda) = D\lambda\left(\frac{1}{\lambda} - \frac{1}{\lambda_g}\right)^n \quad (3)$$

where $D = B(hc)^{n-1}(2.303/z)A$, z is the film thickness, A is the film absorbance, c is the velocity of light and λ_g is the wavelength corresponding to the optical band gap. Equation (3) can be rewritten as:

$$\ln\frac{A(\lambda)}{(\lambda)} = lnD + nln\left(\frac{1}{\lambda} - \frac{1}{\lambda g}\right) \quad (4)$$

and its first derivative with respect to $1/\lambda$ is:

$$\frac{d\{\ln[A(\lambda)/\lambda]\}}{d(1/\lambda)} = \frac{n}{\left(\frac{1}{\lambda}-\frac{1}{\lambda_g}\right)} \quad (5)$$

By plotting left-hand side of equation (5) vs 1/λ can provide peak-shaped data as shown in Figure 9. The peak maximum indicates a band gap[37] [eV] as $E = 1239.83/\lambda_g$. This value can be cross-checked fitting to either of the direct or the indirect one calculated directly by the Tauc method. Notably, the DASF method can also be expressed starting from equation (1) (Tauc method) as follows:

$$F(R) = B(h\nu - E_g)^n \quad (6)$$

$$lnF(R) = lnB + nln(h\nu - E_g) \quad (7)$$

$$\frac{dlnF(R)}{dh\nu} = \frac{n}{(h\nu - E_g)} \quad (8)$$

Thus band gaps calculated by the DASF method does not provide any new value rather validates if the materials possess a direct or an indirect band gap. The data obtained by the DASF method were fitted with the software TOPAS V4.2 (Bruker AXS, Karlsruhe, Germany) to determine the positions of the peak maximum. To judge the applicability of the method we used well studied Degussa's TiO_2 P25 with an indirect band gap of 3.14 eV.[38] The band gaps were determined using both the Tauc's method (assuming direct and indirect transitions) as well as the DASF method as shown in Figure 8 and Figure 9, respectively. The value obtained by the DASF method (3.057(1) eV) is in good agreement with the one using the Tauc's method (3.04 eV) assuming indirect transitions. Since the results are consistent with those of literature ones the combination of the DASF method and the Tauc's method can provide reliable results concerning the width together with its standard deviation as well as the nature of transition of semiconductor band gaps.

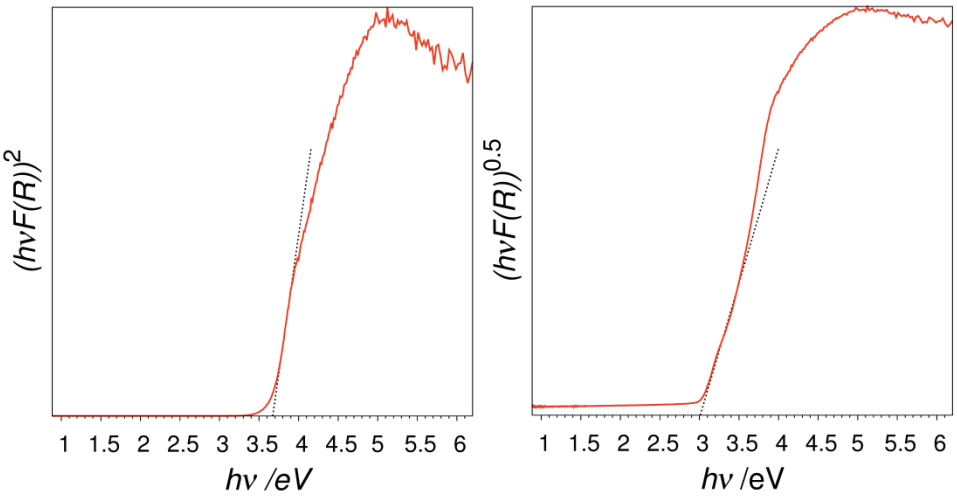

Figure 8. Tauc plot of sample TiO_2 P25 assuming direct (left) and indirect (right) transitions. The dotted lines show the respective intercepts for band gaps.

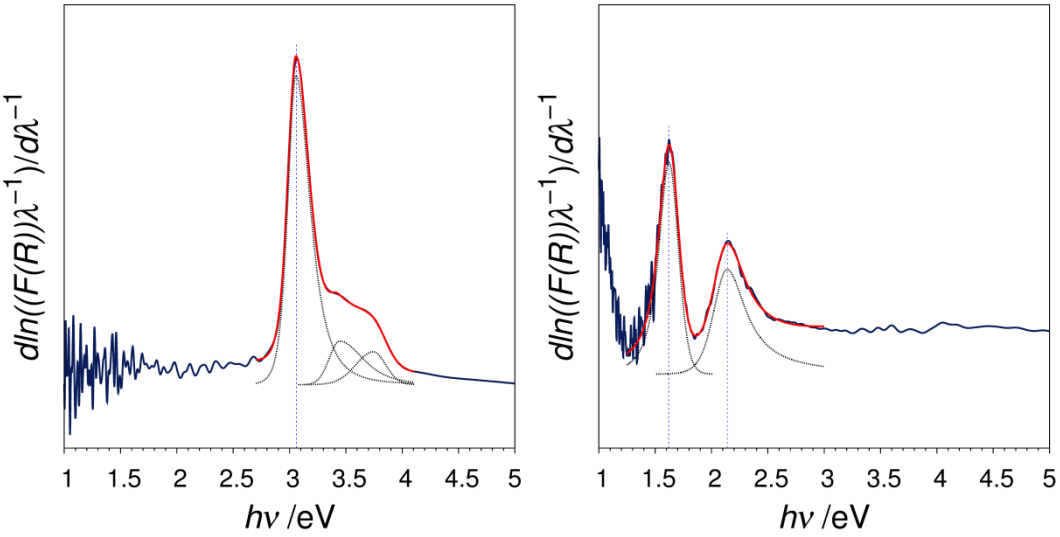

Figure 9. DASF plots of TiO_2 P25 (left) and mullite-type $Bi_2Fe_4O_9$ sample (right) BFO/973 K (see **Table 1**). The dotted lines show the fitted peak positions.

The evolution of the *F*(*R*) spectra with the calcination temperature of the synthesized BFO samples is shown in Figure 10. The as-synthesized powder clearly shows absorption at smaller wavelengths which is in accordance with its greatly smaller crystallite sizes. The variation of calcination temperature not only shifts the absorption edge but also changes the spectral feature. A second absorption edge, typical for the $Bi_2Fe_4O_9$ structure,[1,3,28] appears for samples calcined above 773 K, which gets more pronounced at higher temperatures (see inset in Figure 10). The origin of a second edge in the absorption spectra is an ongoing topic of debates. It is suggested that the second absorption edge is caused by the d-d-transitions of Fe^{3+}.[3]

In contrast, a theoretical study indicated that the second absorption edge is caused by inter-valence charge transfer between randomly arranged Fe^{2+} and Fe^{3+} induced by uneven distributed negative charges.[28] The latter authors also concluded that the previously reported d-d transitions are both spin and Laporte forbidden[28] and therefore the molar absorption coefficient of the ligand field transition is about three order of magnitude lower than that of the charge transfer transitions.[28] In another report Sherman and Waite[39] pointed out that ligand field transitions of Fe^{3+} can be intensified by magnetic coupling of adjacent Fe^{3+} cations and that these transitions become allowed through a strong magnetic coupling of Fe^{3+} - Fe^{3+} pairs. *Ab initio* investigations of Pchelkina and Streltsov[40] revealed that the exchange interactions between the two tetrahedral Fe_t ions are the largest in $Bi_2Fe_4O_9$. In this study the second absorption edge is appearing as soon as the vibrational mode typical for the tetrahedral unit in $Bi_2Fe_4O_9$ (812 cm^{-1}) can be identified in the FTIR and gets more pronounced with higher relative intensity in the spectra (see Figure 13, Table 4). This observation supports the assumption that the second absorption edge is caused by the d-d transitions that may be intensified by strong magnetically coupled Fe^{3+} - Fe^{3+} tetrahedral pairs. We also do not decline the possibility of phonon-driven indirect band gap because a pronounced second-absorption edge was also seen in $Bi_2Al_4O_9$ with no d-d transitions and no magnetic interactions. The fundamental absorption edge gradually shifts to higher wavelengths till 723 K and then shifts back to smaller wavelengths at about 1023 K, resulting in a shift from 2.75(3) eV to 1.80(3) eV and back to 2.13(1) eV, respectively. Due to different treatment of the Tauc method (direct or indirect) disagreements appeared in literature concerning the nature of transition for both $BiFeO_3$ and $Bi_2Fe_4O_9$.[12,15,16,19,20,23,26] We compared the values for the direct as well as indirect transitions determined by the Tauc's method with those obtained by DASF method (see Table 2, Figure 11). The values obtained by DASF method are in very good agreement with the values obtained by the Tauc's method considering direct transitions for samples calcined above 873 K. However, the values obtained for samples calcined between 573 K and 823 K can be attributed neither to direct transitions nor to indirect transitions determined by the Tauc's method (Table 2). The calculated values remain between them. This could be attributed to the difficulties in the determination of band gap of the amorphous materials, because the edges of the tail states complicate determining the true optical band gap.[41] Using the Tauc relationship a quadratic absorption edge is considered but amorphous

semiconductors often show an exponential behavior.[42] In addition, certain selection rules (particularly that of momentum conservation) which apply to optical transitions in crystalline materials are relaxed in amorphous semiconductors.[42] So the values determined by the DASF method seem to be more reliable than the Tauc ones. Interestingly, in the case of as-synthesized sample BFO the DASF method shows two absorption edges at 2.1(1) eV and 2.75(3) eV. The band gap of 2.75(3) eV fits well to the direct transition value of 2.7 eV determined by the Tauc's method; however, the value 2.1 eV fits to the indirect transition value of 2.1(1) eV. An additional indirect band gap at lower energies next to a direct band gap in nano-sized $BiFeO_3$ particles[15] and thin films[43] are reported. Theoretical calculations of Dong et al.[44] predicted an indirect transition in a highly strained $BiFeO_3$ sample.

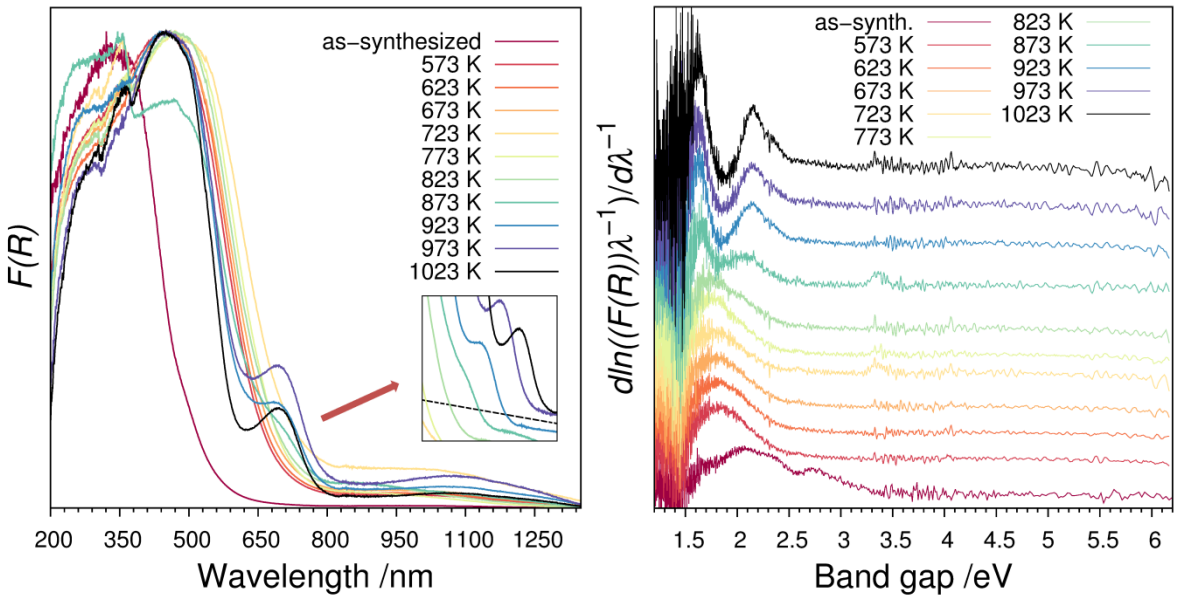

Figure 10. *Left panel:* UV/Vis F(R) spectra calculated out of reflectance spectra by the Kubelka-Munk function. *Right panel:* DASF plots of the as-synthesized powder and samples heated at 573 – 1023 K at every 50 K for 2 h.

Table 2. Absorption edges obtained by Tauc's and DASF methods.

Sample	DASF method		Tauc's method			
			direct $(\alpha h\nu)^2$		indirect $(\alpha h\nu)^{1/2}$	
BFO	2.1(1)	2.75(3)	–	2.70	–	2.08
BFO/573	–	1.82(9)	–	2.04	–	1.62
BFO/623	–	1.82(7)	–	2.03	–	1.61
BFO/673	–	1.80(7)	–	2.00	–	1.57
BFO/723	–	1.80(3)	–	1.90	–	1.46
BFO/773	1.75(7)	2.11(25)	–	1.97	–	1.54
BFO/823	1.69(4)	1.98(25)	–	1.98	–	1.51
BFO/873	1.65(1)	2.08(9)	1.63	2.02	1.40	1.58
BFO/923	1.64(1)	2.13(3)	1.62	2.13	1.45	1.74
BFO/973	1.64(1)	2.13(3)	1.61	2.12	1.44	1.74
BFO/1023	1.63(1)	2.13(1)	1.63	2.19	1.50	1.87

DASF = Derivation of absorption spectrum fitting method
See table 1 for the details of the samples (BFO/#)

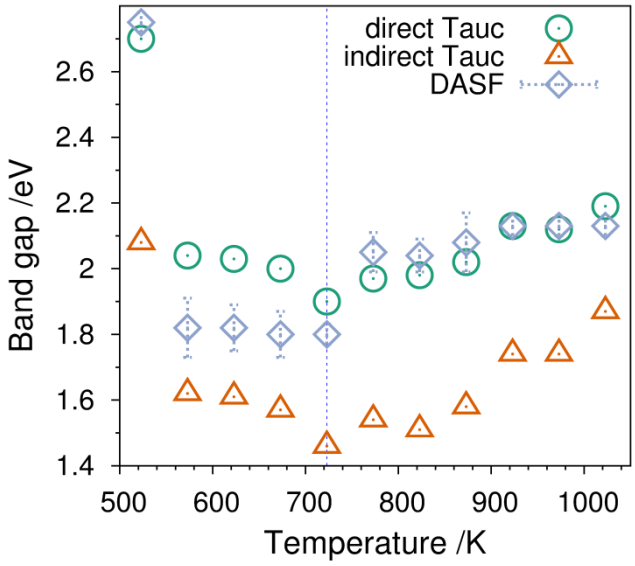

Figure 11. Band gaps of the as-synthesized powder and samples (heated at 573 – 1023 K at every 50 K for 2 h) obtained by Tauc's and DASF methods. The dotted line indicates the smallest found band gap.

Raman Spectroscopy

The Raman spectra of the as-synthesized as well as the samples calcined below 823 K do not show any distinct vibrational feature as seen in Figure 12. The sample calcined at 823 K clearly shows two main bands of the perovskite-type structure at 139.4(9) cm^{-1} and 168.3(1) cm^{-1} assigned to A_1 modes[45] as given in Table 3. From 873 K on the bands of the perovskite-type as well as the mullite-type phases can be

observed. Although XRD results show that the sample BFO/823 contains a significant amount of $Bi_2Fe_4O_9$ (22.4(7)%, Table 1) the respective bands could not be resolved from the Raman spectra maybe due to band merging. For instance, at ambient condition $Bi_2Fe_4O_9$ exhibit Raman bands at 87, 110, 182, 207, 222, 283, 331, 365, 430, 552 and 647 cm^{-1}.[46] Above 873 K the bands of Fe_2O_3[47] at 225, 292, 299, 410 and 611 cm^{-1} can also be identified although the Fe_2O_3 content in the samples is very low (< 3%, Table 1). Starting from 873 K all spectra show the typical mullite-type $Bi_2Fe_4O_9$ modes.

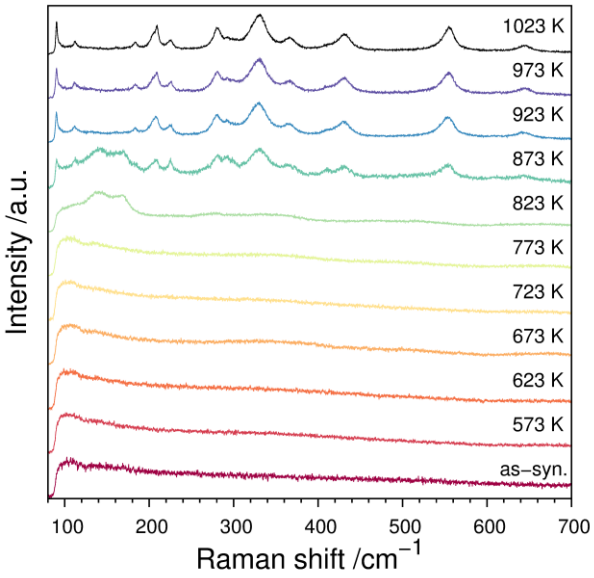

Figure 12. Raman spectra of $Bi_2Fe_4O_9$ as-synthesized powder and samples heated *ex situ* between 573 and 1023 K at 50 K step for 2 h.

Table 3. Raman frequencies [cm^{-1}] of polyol samples calcined between 823 K and 1023 K, bulk $BiFeO_3$ and $Bi_2Fe_4O_9$.

Raman shifts /cm^{-1}						
BFO/823	BFO/873	BFO/923	BFO/973	BFO/1023	$BiFeO_3$[48]	$Bi_2Fe_4O_9$[46]
–	90.6(1)	90.0(2)	90.2(6)	90.3(3)	–	87
108(2)	110.9(11)	111.8(1)	112.0(3)	112.4(1)	–	110
139.4(9)	139.1(12)	–	–	–	136	–
168.3(1)	167.8(10)	–	–	–	170	–
–	184.9(3)	183.2(2)	183.5(3)	183.4(1)	–	182
–	207.2(2)	209.0(4)	209.3(1)	209.3(1)	–	207
223(10)	–	–	–	–	217	–
–	225.2(2)	225.4(2)	225.7(4)	224.6(7)	–	222
260.6(2)	–	–	–	–	260	–
275(1)	–	–	–	–	278	–
–	280.5(9)	279.8(3)	280.3(3)	280.7(2)	–	283
–	330.1(2)	329.4(2)	330.1(3)	332(1)	–	331
340 (17)	–	–	–	–	345	–
366(2)	366.6(8)	366.1(2)	366.6(4)	366.5(2)	365	365
–	–	–	–	–	425	–
–	430.8(3)	430.5(2)	430.8(2)	431.3(1)	–	430
464(8)	–	–	–	–	469	–
526(4)	–	–	–	–	520	–
–	553.1(2)	553.5(1)	554.5(1)	554.2(1)	–	552
640(9)	643.6(7)	643.2(2)	643.9(2)	644.5(2)	–	647

See table 1 for the details of the samples (BFO/#)

Infrared Spectroscopy

The evolutions of FTIR spectra of the calcined samples are shown in Figure 13. The band positions and assignments are summarized and compared to respective literature values as given in Table 4. Typical bands for the perovskite-type $BiFeO_3$[20] around ~445 and ~548 cm^{-1} can be identified in samples until 823 K. From 873 K on, the bands assigned to the stretching and bending of Fe−O of the tetrahedral unit of the mullite-type $Bi_2Fe_4O_9$ structure can clearly be identified.[49] However, the sample calcined at 823 K already contains a significant amount of $Bi_2Fe_4O_9$ (22.4(7)%, Table 1), and the typical modes of the structure cannot be detected (e.g., 812 cm^{-1}) as in the Raman spectra. This behavior might be a hint for a stronger disorder in the double-tetrahedral units compared to the octahedral chains during the formation of the mullite-type phase[5] caused by initial tricluster[50] formation. Starting from 923 K on, no other bands than the expected bands for $Bi_2Fe_4O_9$ can be identified. The modes between 1200 and 1700 cm^{-1} are assumed to be related to the vibrations of some starting/modified organic species which disappeared when the samples were calcined above 873 K.

Table 4. FTIR band positions [cm^{-1}] of polyol samples calcined between 573 K and 1023 K, bulk $BiFeO_3$ and $Bi_2Fe_4O_9$.

Band positions /cm^{-1}											
$BiFeO_3$[20]	BFO /573	BFO /623	BFO /673	BFO /723	BFO /773	BFO /823	BFO /873	BFO /923	BFO /973	BFO /1023	$Bi_2Fe_4O_9$[49]
445	–	–	–	–	444(5)	445(1)	441(3)	437(1)	439(2)	440(4)	437
–	478(3)	472(2)	469(1)	472(4)	–	–	467(4)	473(9)	473(12)	478(10)	471
–	–	–	–	–	–	–	493(4)	497(3)	498(2)	499(4)	497
–	–	–	–	–	–	529(5)	533(15)	530(14)	530(11)	529(10)	527
548	568(4)	564(3)	566(4)	569(3)	562(9)	556(3)	–	–	–	–	–
–	–	–	–	–	–	589(9)	–	587(41)	584(8)	584(10)	570
–	–	–	–	–	–	–	601(9)	609(5)	608(3)	609(6)	600
–	–	–	–	–	–	633(9)	643(2)	639(5)	640(7)	639(6)	648
–	–	–	–	–	–	697(3)	667(31)	653(62)	661(53)	662(40)	–
–	–	–	–	–	–	–	812(1)	812(1)	812(1)	813(1)	812

See table 1 for the details of the samples (BFO/#)

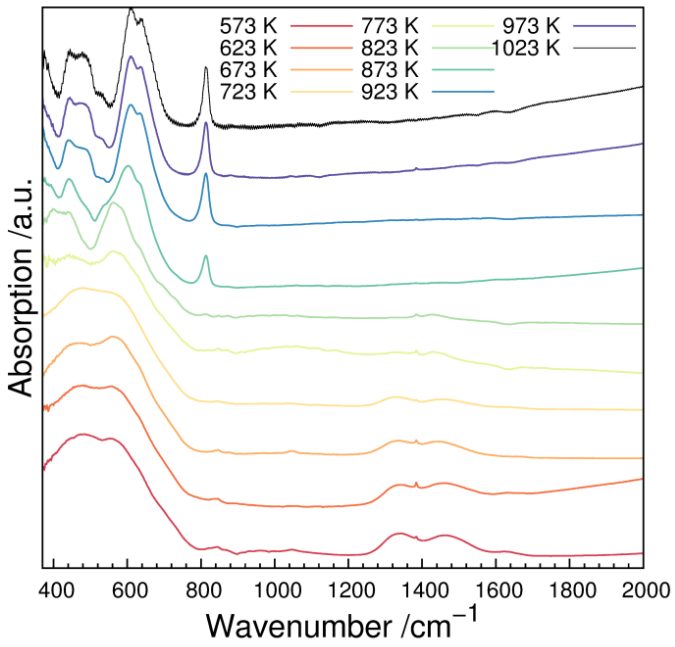

Figure 13. FTIR spectra of $Bi_2Fe_4O_9$ polyol samples heated *ex situ* at 573 – 1023 K at 50 K step for 2 h.

4. CONCLUSION

The mullite-type $Bi_2Fe_4O_9$ was synthesized via the polyol method followed by subsequent calcination. Mixtures of perovskite-type and mullite-type structures with small crystallite sizes were successfully produced showing different optical features with band gaps between 1.80(1) and 2.75(3) eV. The results suggest that $Bi_2Fe_4O_9$ is a direct semiconductor with a band gap of 2.13(3) eV. The observed second absorption edge of $Bi_2Fe_4O_9$ may be related either to thermal phonon driven effect or the d−d transitions of the Fe^{3+}−Fe^{3+} tetrahedral pairs, whereas the latter could not explain the observation of a second absorption edge in isotypic $Bi_2Al_4O_9$. The samples exhibit a well-functionalized surface covered by nanoparticles of 4 – 13 nm in size, which rearranged by the electron beam during TEM investigations. The present study suggests that the derivative absorption spectrum fitting (DASF) method, is found to be a suitable tool to concomitantly determine the band gap and the nature of transition (direct and indirect) by comparing the values to those obtained by the Tauc's method. Whether a mixture of $BiFeO_3$ and $Bi_2Fe_4O_9$ provides a higher photocatalytic activity compared to either $BiFeO_3$ or $Bi_2Fe_4O_9$ (analogous to rutile: anatase) would be interesting.

ASSOCIATED CONTENT

*S Supporting Information

The Supporting Information is available free of charge on the ACS Publications website at DOI: 10.1021/acs.jpcc.6b04773. Change of shape and facet of a nanoparticle during the acquisition of the 10 images using HRTEM (Video S1) (AVI)

AUTHOR INFORMATION

Corresponding Author

*E-mail address: murshed@uni-bremen.de; phone: +49 (0)421 218 63144; fax: +49 (0)421 218 63144. Notes The authors declare no competing financial interest.

ACKNOWLEDGMENTS

We gratefully thank the University of Bremen for the financial support.

Reference

(1) Zhang, Q.; Gong, W.; Wang, J.; Ning, X.; Wang, Z.; Zhao, X.; Ren, W.; Zhang, Z. Size-Dependent Magnetic, Photoabsorbing, and Photocatalytic Properties of Single-Crystalline $Bi_2Fe_4O_9$ Semiconductor Nanocrystals. *J. Phys. Chem. C* **2011**, *115*, 25241–25246.

(2) Li, Y.; Zhang, Y.; Ye, W.; Yu, J.; Lu, C.; Xia, L. Photo-to-Current Response of $Bi_2Fe_4O_9$ Nanocrystals Synthesized through a Chemical Co-Precipitation Process. *New J. Chem.* **2012**, *36* (6), 1297–1300.

(3) Sun, S.; Wang, W.; Zhang, L.; Shang, M. Visible Light-Induced Photocatalytic Oxidation of Phenol and Aqueous Ammonia in Flowerlike $Bi_2Fe_4O_9$ Suspensions. *J. Phys. Chem. C* **2009**, *113*, 12826–12831.

(4) Park, T.; Papaefthymiou, G. C.; Viescas, A. J.; Moodenbaugh, A. R.; Wong, S. S. Size-Dependent Magnetic Properties of Single-Crystalline Multiferroic BiFeO 3 Nanoparticles. *Nano Lett.* **2007**, *7* (3), 766–772.

(5) Gesing, T. M.; Fischer, R. X.; Burianek, M.; Mühlberg, M.; Debnath, T.; Rüscher, C. H.; Ottinger, J.; Buhl, J.-C.; Schneider, H. Synthesis and Properties of Mullite-Type $(Bi_{1-x}Sr_x)_2(M1_{1-y}M2_y)_4O_{9-x}$ (M=Al, Ga, Fe). *J. Eur. Ceram. Soc.* **2011**, *31* (16), 3055–3062.

(6) Schneider, H.; Fischer, R. X.; Gesing, T. M.; Schreuer, J.; Mühlberg, M. Crystal Chemistry and Properties of Mullite-Type $Bi_2M_4O_9$: An Overview. *Int. J. Mater. Res.* **2012**, *103* (4), 422–429.

(7) Weber, S.-U.; Gesing, T. M.; Röder, J.; Litterst, J.; Fischer, R. X.; Becker, K. D. Temperature-Dependent ^{57}Fe Mössbauer Spectroscopy and Local Structure of Mullite-Type $Bi_2(Fe_xAl_{1-x})_4O_9$ ($0.1<x<1$) Solid Solutions. *Int. J. Mater. Res.* **2012**, *103*, 430–437.

(8) Weber, S.; Gesing, T. M.; Eckold, G.; Fischer, R. X.; Litterst, F.; Becker, K. Temperature-Dependent ^{57}Fe Mössbauer Spectroscopy and Local Structure of

the Mullite Type $Bi_2(Fe_xGa_{1-x})_4O_9$ (0.1<x1) Solid Solution. *J. Phys. Chem. Solids* **2014**, *75*, 416–426.
(9) Murshed, M. M.; Nénert, G.; Burianek, M.; Robben, L.; Mühlberg, M.; Schneider, H.; Fischer, R. X.; Gesing, T. M. Temperature-Dependent Structural Studies of Mullite-Type $Bi_2Fe_4O_9$. *J. Solid State Chem.* **2013**, *197*, 370–378.
(10) Koizumi, H.; Niizeki, N.; Ikeda, T. An X-Ray Study on Bi_2O_3-Fe_2O_3 System. *Jpn. J. Appl. Phys.* **1964**, *3*, 495–496.
(11) Wang, X.; Zhang, M.; Tian, P.; Chin, W. S.; Zhang, C. M. A Facile Approach to Pure-Phase $Bi_2Fe_4O_9$ Nanoparticles Sensitive to Visible Light. *Appl. Surf. Sci.* **2014**, *321*, 144–149.
(12) Wang, X.; Lin, Y.; Zhang, Z. C.; Bian, J. Y. Photocatalytic Activities of Multiferroic Bismuth Ferrite Nanoparticles Prepared by Glycol-Based Sol–gel Process. *J. Sol-Gel Sci. Technol.* **2011**, *60* (1), 1–5.
(13) Zhao, J.; Liu, T.; Xu, Y.; He, Y.; Chen, W. Synthesis and Characterization of $Bi_2Fe_4O_9$ Powders. *Mater. Chem. Phys.* **2011**, *128* (3), 388–391.
(14) Xian, T.; Yang, H.; Shen, X.; Jiang, J. L.; Wei, Z. Q.; Feng, W. J. Preparation of High-Quality $BiFeO_3$ Nanopowders via a Polyacrylamide Gel Route. *J. Alloys Compd.* **2009**, *480* (2), 889–892.
(15) Ortiz-Quiñonez, J. L.; Díaz, D.; Zumeta-Dubé, I.; Arriola-Santamaría, H.; Betancourt, I.; Santiago-Jacinto, P.; Nava-Etzana, N. Easy Synthesis of High-Purity $BiFeO_3$ Nanoparticles: New Insights Derived from the Structural, Optical, and Magnetic Characterization. *Inorg. Chem.* **2013**, *52* (18), 10306–10317.
(16) Ruan, Q.-J.; Zhang, W.-D. Tunable Morphology of $Bi_2Fe_4O_9$ Crystals for Photocatalytic Oxidation. *J. Phys. Chem. C* **2009**, *113* (10), 4168–4173.
(17) Fischer, P.; Polomska, M.; Sosnowska, I.; Szymanski, M. Temperature Dependence of the Crystal and Magnetic Structures of $BiFeO_3$. *J. Phys. C* **1980**, *13*, 1931–1940.
(18) Ruette, B.; Zvyagin, S.; Pyatakov, A. P.; Bush, A.; Li, J. F.; Belotelov, V. I.; Zvezdin, A. K.; Viehland, D. Magnetic-Field-Induced Phase Transition in $BiFeO_3$ Observed by High-Field Electron Spin Resonance: Cycloidal to Homogeneous. *Phys. Rev. B* **2004**, *69* (6), 064114.
(19) Gao, F.; Chen, X. Y.; Yin, K. B.; Dong, S.; Ren, Z. F.; Yuan, F.; Yu, T.; Zou, Z. G.; Liu, J.-M. Visible-Light Photocatalytic Properties of Weak Magnetic $BiFeO_3$ Nanoparticles. *Adv. Mater.* **2007**, *19* (19), 2889–2892.
(20) Srivastav, S. K.; S. Gajbhiye, N. Low Temperature Synthesis, Structural, Optical and Magnetic Properties of Bismuth Ferrite Nanoparticles. *J. Am. Ceram. Soc.* **2012**, *95* (11), 3678–3682.
(21) Ihlefeld, J. F.; Podraza, N. J.; Liu, Z. K.; Rai, R. C.; Xu, X.; Heeg, T.; Chen, Y. B.; Li, J.; Collins, R. W.; Musfeldt, J. L.; et al. Optical Band Gap of $BiFeO_3$ Grown by Molecular-Beam Epitaxy. *Appl. Phys. Lett.* **2008**, *92* (14), 142908.
(22) Zhao, Y.; Miao, J.; Zhang, X.; Chen, Y.; Xu, X. G.; Jiang, Y. Ultra-Thin $BiFeO_3$ Nanowires Prepared by a Sol–gel Combustion Method: An Investigation of Its Multiferroic and Optical Properties. *J. Mater. Sci. Mater. Electron.* **2012**, *23* (1), 180–184.
(23) Xian, T.; Yang, H.; Dai, J. F.; Wei, Z. Q.; Ma, J. Y.; Feng, W. J. Photocatalytic

Properties of $BiFeO_3$ Nanoparticles with Different Sizes. *Mater. Lett.* **2011**, *65* (11), 1573–1575.
(24) Singh, A. K.; Kaushik, S. D.; Kumar, B.; Mishra, P. K.; Venimadhav, A.; Siruguri, V.; Patnaik, S. Substantial Magnetoelectric Coupling near Room Temperature in $Bi_2Fe_4O_9$. *Appl. Phys. Lett.* **2008**, *92* (13), 132910.
(25) Wu, X. H.; Miao, J.; Zhao, Y.; Meng, X. B.; Xu, X. G.; Wang, S. G.; Jiang, Y. Novel Multiferroic $Bi_2Fe_4O_9$ Nanoparticles: The Interesting Optical, Photocatalytic, and Multiferroic Properties. *Optoelectron. Adv. Mater. Rapid Commun.* **2013**, *7* (1-2), 116–120.
(26) Hu, Z.-T.; Chen, B.; Lim, T.-T. Single-Crystalline $Bi_2Fe_4O_9$ Synthesized by Low-Temperature Co-Precipitation: Performance as Photo- and Fenton Catalysts. *RSC Adv.* **2014**, *4* (53), 27820.
(27) Cai, D.; Du, D.; Yu, S.; Cheng, J. Oriented Growth of $Bi_2Fe_4O_9$ Crystal and Its Photocatalytic Activity. *Procedia Eng.* **2012**, *27*, 577–582.
(28) Zhang, Y.; Guo, Y.; Duan, H.; Li, H.; Yang, L.; Wang, P.; Sun, C.; Xu, B.; Liu, H. Photoelectrochemical Response and Electronic Structure Analysis of Mono-Dispersed Cuboid-Shaped $Bi_2Fe_4O_9$ Crystals with near-Infrared Absorption. *RSC Adv.* **2014**, *4* (54), 28209–28218.
(29) Chen, P.; Xu, X.; Koenigsmann, C.; Santulli, A. C.; Wong, S. S.; Musfeldt, J. L. Size-Dependent Infrared Phonon Modes and Ferroelectric Phase Transition in $BiFeO_3$ Nanoparticles. *Nano Lett.* **2010**, *10* (11), 4526–4532.
(30) Fievet, F.; Lagier, J. P.; Figlarz, M. Preparing Monodisperse Metal Powders in Micrometer and Submicrometer Sizes by the Polyol Process. *MRS Bull.* **1989**, *14* (12), 29–34.
(31) Feldmann, C. Polyol-Mediated Synthesis of Nanoscale Functional Materials. *Solid State Sci.* **2005**, *7* (7), 868–873.
(32) Bakardjieva, S.; Šubrt, J.; Štengl, V.; Dianez, M. J.; Sayagues, M. J. Photoactivity of Anatase–rutile TiO_2 Nanocrystalline Mixtures Obtained by Heat Treatment of Homogeneously Precipitated Anatase. *Appl. Catal. B Environ.* **2005**, *58* (3-4), 193–202.
(33) Hurum, D. C.; Agrios, A. G.; Gray, K. A.; Rajh, T.; Thurnauer, M. C. Explaining the Enhanced Photocatalytic Activity of Degussa P25 Mixed-Phase TiO_2 Using EPR. *J. Phys. Chem. B* **2003**, *107* (19), 4545–4549.
(34) Zhao, J.; Liu, T.; Xu, Y.; He, Y.; Chen, W. Synthesis and Characterization of $Bi_2Fe_4O_9$ Powders. *Mater. Chem. Phys.* **2011**, *128* (3), 388–391.
(35) Kirsch, A.; Murshed, M. M.; Gaczynski, P.; Becker, K.-D.; Gesing, T. M. $Bi_2Fe_4O_9$: Structural Changes from Nano- to Micro-Crystalline State. *Zeitschrift für Naturforsch. B* **2016**, *0* (0).
(36) Tauc, J.; Grigorovici, R.; Vancu, A. Optical Properties and Electronic Structure of Amorphous Germanium. *Phys. Status Solidi* **1966**, *15*, 627–637.
(37) Souri, D.; Tahan, Z. E. A New Method for the Determination of Optical Band Gap and the Nature of Optical Transitions in Semiconductors. *Appl. Phys. B* **2015**, *119* (2), 273–279.
(38) Zielińska, B.; Grzechulska, J.; Grzmil, B.; Morawski, A. W. Photocatalytic Degradation of Reactive Black 5 A Comparison between TiO_2-Tytanpol A11

and TiO_2-Degussa P25 Photocatalysts. *Appl. Catal. B Environ.* **2001**, *35* (1), L1–L7.

(39) Sherman, D. M.; Waite, T. D. Electronic Spectra of Fe^{3+} Oxides and Oxide Hydroxides in the near IR to near UV. *Am. Mineral.* **1985**, *70* (11-12), 1262–1269.

(40) Pchelkina, Z. V.; Streltsov, S. V. Ab Initio Investigation of the Exchange Interactions in $Bi_2Fe_4O_9$: The Cairo Pentagonal Lattice Compound. *Phys. Rev. B* **2013**, *88* (5), 054424.

(41) Souri, D.; Shomalian, K. Band Gap Determination by Absorption Spectrum Fitting Method (ASF) and Structural Properties of Different Compositions of (60−x) V_2O_5–40 $TeO_{2-x}Sb_2O_3$ Glasses. *J. Non. Cryst. Solids* **2009**, *355* (31-33), 1597–1601.

(42) Mott, N. F.; Davis, E. A. *Electronic Processes In Non-Crystalline Materials*, Second edi.; Oxford University Press, 1979.

(43) Gujar, T. P.; Shinde, V. R.; Lokhande, C. D. Nanocrystalline and Highly Resistive Bismuth Ferric Oxide Thin Films by a Simple Chemical Method. *Mater. Chem. Phys.* **2007**, *103* (1), 142–146.

(44) Dong, H.; Wu, Z.; Wang, S.; Duan, W.; Li, J. Improving the Optical Absorption of $BiFeO_3$ for Photovoltaic Applications via Uniaxial Compression or Biaxial Tension. *Appl. Phys. Lett.* **2013**, *102* (7), 072905–1 – 5.

(45) Yang, Y.; Sun, J. Y.; Zhu, K.; Liu, Y. L.; Chen, J.; Xing, X. R. Raman Study of $BiFeO_3$ with Different Excitation Wavelengths. *Phys. B Condens. Matter* **2009**, *404* (1), 171–174.

(46) Iliev, M. N.; Litvinchuk, A. P.; Hadjiev, V. G.; Gospodinov, M. M.; Skumryev, V.; Ressouche, E. Phonon and Magnon Scattering of Antiferromagnetic $Bi_2Fe_4O_9$. *Phys. Rev. B* **2010**, *81* (2), 024302.

(47) Shim, S.-H.; Duffy, T. S. Raman Spectroscopy of Fe_2O_3 to 62 GPa. *Am. Mineral.* **2001**, *87*, 318–326.

(48) Arora, M.; Sati, P. C.; Chauhan, S.; Chhoker, S.; Panwar, A. K.; Kumar, M. Structural, Optical and Multiferroic Properties of $BiFeO_3$ Nanoparticles Synthesized by Soft Chemical Route. *J. Supercond. Nov. Magn.* **2013**, *26* (2), 443–448.

(49) Voll, D.; Beran, A.; Schneider, H. Variation of Infrared Absorption Spectra in the System $Bi_2Al_{4-x}Fe_XO_9$ (X = 0–4), Structurally Related to Mullite. *Phys. Chem. Miner.* **2006**, *33* (8-9), 623–628.

(50) Gesing, T. M.; Schowalter, M.; Weidenthaler, C.; Murshed, M. M.; Nénert, G.; Mendive, C. B.; Curti, M.; Rosenauer, A.; Buhl, J.-C.; Schneider, H.; et al. Strontium Doping in Mullite-Type Bismuth Aluminate: A Vacancy Investigation Using Neutrons, Photons and Electrons. *J. Mater. Chem.* **2012**, *22* (36), 18814.

Chapter 6

Structural, spectroscopic and thermoanalytic studies on $Bi_2Fe_4O_9$: tunable properties driven by nano- and poly-crystalline states.

Andrea Kirsch[a,b], M. Mangir Murshed[a,b*], F. Jochen Litterst[c], Thorsten M. Gesing[a,b]

[a] University of Bremen, Institute of Inorganic Chemistry and Crystallography, Leobener Straße 7, D-28359 Bremen, Germany

[b] University of Bremen, MAPEX center for materials and processes, Bibliothekstraße 1, D-28359 Bremen Germany

[c] Technische Universität Braunschweig, Institute for Condensed Matter Physics, Mendelssohnstr. 3, D-38106 Braunschweig, Germany

∗Corresponding author Tel.: +49 (0)421 218 63144, fax: +49 421 218 63145; e-mail: murshed@uni-bremen.de

Abstract

We report on average crystallite size dependent structural, spectroscopic and thermoanalytic studies of $Bi_2Fe_4O_9$ synthesized by a sol-gel method. *In-situ* heating X-ray diffraction revealed the transformation of an X-ray amorphous precursor into a rhombohedral perovskite-type $BiFeO_3$ followed by a second transformation into orthorhombic mullite-type $Bi_2Fe_4O_9$ phase. Twelve samples with average crystallite sizes between 35.3(4) nm and 401(17) nm were produced by calcination of the precursor for two hours at temperatures between 900 K and 1073 K. Average crystallite sizes calculated from X-ray diffraction and transmission electron microscopy are in excellent agreement. X-ray powder diffraction data Rietveld refinements demonstrate each structural feature as function of the average crystallite size. Both in the *in-situ* and *ex-situ* experiments the metric parameters evolve through expansion of *a*- and, contractions of *b*- and *c*-cell parameters, leading to a parabolic expansion of the cell volume. The associated nano-properties significantly differ across a critical average crystallite size of 122(2) nm, such as metric parameters, polyhedral distortions, vibrational mode frequencies, bandgaps and hyperfine parameters. The antiferromagnetic transition temperature was found to be 249(1) K for an average crystallite size of 86(1) nm, and its transition enthalpy significantly decreases below the critical size as observed by differential scanning calorimetry. The second absorption feature in the UV/Vis, which is typical for bulk $Bi_2Fe_4O_9$, was found to be mainly caused by the d-d transition of the Fe^{3+} cations in the FeO_4 tetrahedra. Temperature-dependent Raman spectra helped to understand the average crystallite size-dependent characteristic vibrational features of some selective nanomaterials of $Bi_2Fe_4O_9$.

1. Introduction

The study of structure-property relationships is unambiguously important for the development of new key technologies such as water splitting[1], spintronics[2], energy storage[3] and energy conversion[4]. Piezoelectric[5], magnetic[6] or optical properties[7] of a given structure are highly dependent on the dimensionality or crystallite size. Some systems drastically change its magnetic properties[8,9] or even develop magnetism in conventional non-magnetic oxides[10,11] when the crystallites shrink down to a critical nano-size. Therefore, detailed systematic structural studies on nanomaterials and the associated crystallite size-dependent properties are of crucial importance to better understand the rich functionalities of the transition metal oxides. Beside the interesting magnetic[12], electronic[13], optic[14] and catalytic[15] properties of $Bi_2Fe_4O_9$, its crystal-chemistry draws much attention for possible applications as spintronics[14], gas sensors[16] and photocatalysts[17,18]. Although the crystal structure is centrosymmetric the reported multiferroic properties[19,20] harbour considerable ongoing debates. $Bi_2Fe_4O_9$ crystallizes in the orthorhombic space group *Pbam* as shown in Figure 1.[21] $Bi_2Fe_4O_9$ belongs to the mullite-type structure[22] characterized by the edge-sharing FeO_6 octahedra running parallel to the crystallographic **c**-axis. These chains are interconnected by Fe_2O_7 dimers formed by two FeO_4 tetrahedra (Fig. 1). The Bi^{3+} cations reside in the channels formed by the framework, where the stereochemically active $6s^2$ lone electron pairs (LEPs) point toward the vacant sites of the channels.[23] At around $T_N = 240 – 263$ K[19,24-26] the structure undergoes a transition from a paramagnetic into an antiferromagnetic state. The magnetic lattice formed by two non-equivalent iron sites is quite complex and found to be the first analogue of a Cairo pentagonal magnetic lattice.[27] The peculiar non-collinearity of the magnetic lattice was attributed to geometric frustration, and as much as five main magnetic superexchange interactions were identified.[27] There are two equally populated magnetic domains that are phase shifted about 155° alternating along the *c*-axis.[27]

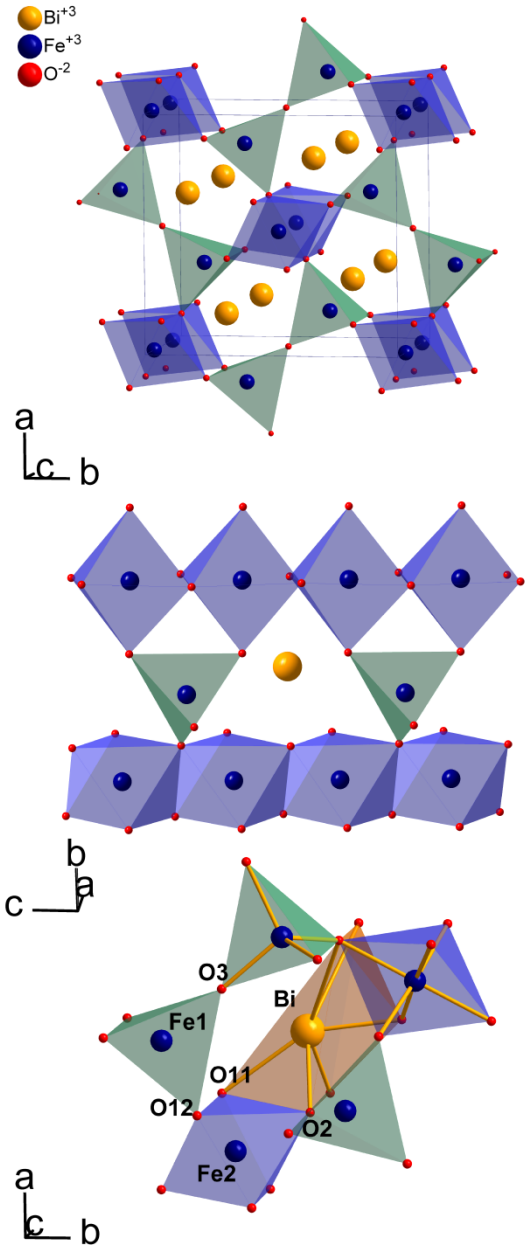

Figure 1. Crystal structure of $Bi_2Fe_4O_9$, showing some polyhedral coordination and their connectivity.

All magnetic moments are found to be perpendicular to the **c**-axis with ferromagnetic coupling between the FeO_6 octahedral units along the chain and antiferromagnetic coupling between the cross-linking Fe_2O_7 tetrahedral units.[27] The latter superexchange interaction was found to be substantially higher (J = 73 K) than the other four (J = 10 – 36 K).[28] Some interesting size-dependent effects in this compound were reported.[12,14] Whereas Tian et al.[12] focused on the magnetic and the ferroelectric properties in the microcrystalline regime, Zhang et al.[14] studied the

magnetic, optic and photocatalytic properties in the nanocrystalline regime (14 – 78 nm). In either case as well as in many relevant publications, it is not clear whether the '*size*' means particle/agglomeration dimension or average crystallite size.[29-31] In this regard, more details on the definition of 'size' is available elsewhere in the review.[32] It is conceivable that a physical parameter such as band gap, Curie/Néel temperature, ferroelectric phase-transition temperature bears significance if the crystallite description includes structural information along with its morphological and distributive descriptions.[33] In the present work, we intend to give a full-fledged structural and spectroscopic analysis of twelve $Bi_2Fe_4O_9$ samples with well-defined crystallite sizes from 35.3(4) nm to 401(17) nm. Each sample was characterized by X-ray powder diffraction (XRD) followed by Rietveld refinement. Raman, Fourier transform infrared (FTIR), diffuse UV/Vis reflectance, ^{57}Fe Mössbauer spectroscopy, transmission electron microscopy (TEM) and differential scanning calorimetry (DSC) were conducted for an in-depth understanding of the size-dependent crystal-physical properties of $Bi_2Fe_4O_9$.

2. Methods

2.1. Synthesis

The synthesis of the sample used for the *in-situ* heating XRD experiment was described elsewhere.[34] The precursors studied for the *ex-situ* XRD were synthesized using the method described by Zhang et al.[14] That is, 5 mmol $Bi(NO_3)_3 \cdot 5H_2O$ (Sigma-Aldrich, ≥ 98%), 10 mmol $Fe(NO_3)_3 \cdot 9H_2O$ (Sigma-Aldrich, ≥ 98%) and 1.98 g PVA (Sigma-Aldrich, Mowiol 10-98, M_W = ~61000 g mol^{-1}) were dissolved into 38 mL deionized water. To prevent the precipitation of $Bi(OH)_3$ 3 mL of conc. HNO_3 were added. The mixture was heated in a glycerine bath to 353 K and stirred, releasing NO_x gases, until a dry foam was obtained after 2.5 h. Afterward, the mixture was dried in an oven at 523 K for about 1.5 h with subsequent grinding. The obtained precursors were separated into two equal portions and calcined in a porcelain crucible for 2 h at temperatures ranging from 900 to 1073 K. In total, 12 samples of mullite-type $Bi_2Fe_4O_9$ structure with ACSs from 35.3(4) nm to 401(17) nm were produced.

2.2. X-ray diffraction

XRD data were collected on an X'Pert MPD PRO diffractometer (PANalytical GmbH, Almelo, The Netherlands). It is equipped with a X'Celerator detector system and uses Ni-filtered $CuK_{\alpha 1,2}$ radiation ($\lambda_{K\alpha 1}$ = 154.05929(5) pm, $\lambda_{K\alpha 2}$ = 154.4414(2) pm) in Bragg-Brentano geometry. For the temperature-dependent investigations an HTK1200N heating chamber (Anton Paar, Graz, Austria) was used. Data were collected from 5 to 100° 2θ with a step width of 0.0167° 2θ and a measurement time of 75 s per step. The *in-situ* measurements were performed from 300 to 1120 K at 20 K step. For each dataset a temperature equilibration time of 5 minute was used. The *ex-situ* measurements were carried out at room temperature from 5 to 85° 2θ with a step width of 0.0167° 2θ and a measurement time of 30 s per step. The obtained data were refined using the Rietveld method (TOPAS V4.2, Bruker AXS) and the fundamental parameter approach was used for profile fitting, where the fundamental parameters were fitted against a standard material (LaB_6). The parameters were refined in a batch; that is, the refined values were used as starting values for the consecutive dataset. During Rietveld refinements the background, metric parameters, profile parameters, atomic coordinates were optimized. In some cases, the isotropic displacement parameters were constrained between atoms of the same element. The average crystallite size (ACS) was calculated from all observed X-ray reflections using the fundamental approach, which is described as $L_{Vol}(IB)$ by the TOPAS suite. $L_{Vol}(IB)$ refers to the volume-weighted mean of the coherently diffracted domain size using the integral breadth for the description of the reflection profile. Since the reflection profile is intrinsically associated with the size, shape, distribution and defects (strain) of the domains[29,30,31] the $L_{Vol}(IB)$ values throughout this study should be considered as 'apparent' ACS for spherical crystallites with a unimodal distribution. Within the TOPAS facilities, the pseudo-Voigt profile function was deconvoluted into Gaussian and Lorentzian components, describing the ACS and micro-strain (ε_0).

2.3. Spectroscopy

Diffuse UV/Vis reflectance spectra were collected on a Shimadzu 2700 UV/Vis spectrophotometer equipped with a UV/Vis DiffuseIR cell (Pike Technologies). Barium sulphate was used for baseline correction. Data were collected in a slow

scanning mode from 190 nm to 850 nm wavelength using 0.5 nm steps. An averaged spectrum was calculated from eight scans for each sample.

Raman spectra were measured on a Horiba LabRam Aramis spectrometer equipped with a Laser of 785 nm, a slit of 100 µm, a hole of 1 mm and an exposure time of 300 s with 2 accumulations. Data were collected between 90 cm^{-1} and 1100 cm^{-1} with a spectral resolution of approx. 2.2 cm^{-1} using a grating of 1200 grooves/mm. Temperature-dependent Raman measurements were performed from 200 – 350 K in 10 K steps using a Linkam cooling stage (THMS600) attached to a pump (LNP95 Cooling Pump) providing a continuous flow of liquid nitrogen. The measurements were carried out on a pressed pellet of the corresponding powder sample with a temperature equilibration time of 7 min. The spectra were fitted with single peaks using the Lamp software[35].

FTIR-measurements were performed from 370 cm^{-1} to 4000 cm^{-1} with 128 scans using the KBr method (0.5 mg sample in 200 mg KBr). The band positions were fitted with the TOPAS V4.2, Bruker AXS software using single peaks of Split-PearsonVII type.

^{57}Fe Mössbauer absorption spectra were collected using a standard spectrometer with sinusoidal velocity sweep. The about 10 mCi ^{57}Co in Rhodium γ-radiation source was kept at room temperature. Absorbers of powder specimens with thicknesses corresponding to about 0.25 $mg \cdot cm^{-2}$ of ^{57}Fe were included in polyethylene containers. The absorber temperatures were varied using a He-flow cryostat (CRYOVAC®). For data analysis, we used the full hyperfine Hamiltonian provided by MossWinn 4.0 software.[36] Due to the relatively high absorber thickness transmission integral analysis was applied.

2.4. Transmission electron microscopy

TEM measurements were carried out on a Titan 80/ 300 kV (FEI Europe, Eindhoven, The Netherlands) equipped with a Cs corrector for the spherical aberration of the objective lens. The microscope was operated at 300 kV during all investigations. The samples were prepared by dissolving the material in ethanol, pestling, and subsequent dispersion on copper grids covered with a thin holey amorphous carbon film.

2.5. Thermal analysis

DSC measurements were performed on a DSC 3^+ STAR^e System of Mettler Toledo. For the measurements, aluminum crucibles were used with an average sample mass of 54 ± 12 mg. After recording the spectra were normalized to their individual mass. The samples were measured with a heating rate of 10 K min^{-1} and a continuous N_2 flow of 20 mL min^{-1} from 200 K to 350 K in 3 full cycles each with a cooling and heating segment, respectively.

3. Results and discussion

3.1. X-ray analysis

In-situ XRD

X-ray powder diffraction revealed that the as-synthesized precursor powder is X-ray amorphous. Upon *in-situ* heating, the precursor first transformed into $BiFeO_3$ perovskite at 740 K followed by a second transformation into mullite-type $Bi_2Fe_4O_9$ from 780 K on.[34] We conducted Rietveld refinements on the XRD data from 780 K to 1120 K to follow the ACS, ε_0 and metric parameters (*a*, *b*, *c* and *V*) of $Bi_2Fe_4O_9$. The structural features were followed starting from the first observation of $Bi_2Fe_4O_9$ reflections. Its crystal structure along with the changes of metric parameters and selected XRD patterns are shown in Figure **2**. $BiFeO_3$ cannot be detected above 860 K, and $Bi_2Fe_4O_9$ was observed to be stable up to 1120 K. That is, the ACS-dependent properties of $Bi_2Fe_4O_9$ between 740 K and 860 K belong to the mixed phase. On the other hand, above 860 K the successive increase of ACS of $Bi_2Fe_4O_9$ at a given temperature is purely due to Ostwald ripening. Figure 3 shows the ACSs obtained from the *in-situ* XRD data Rietveld analyses along with the changes of the metric parameters and the micro-strain while heating the sample.

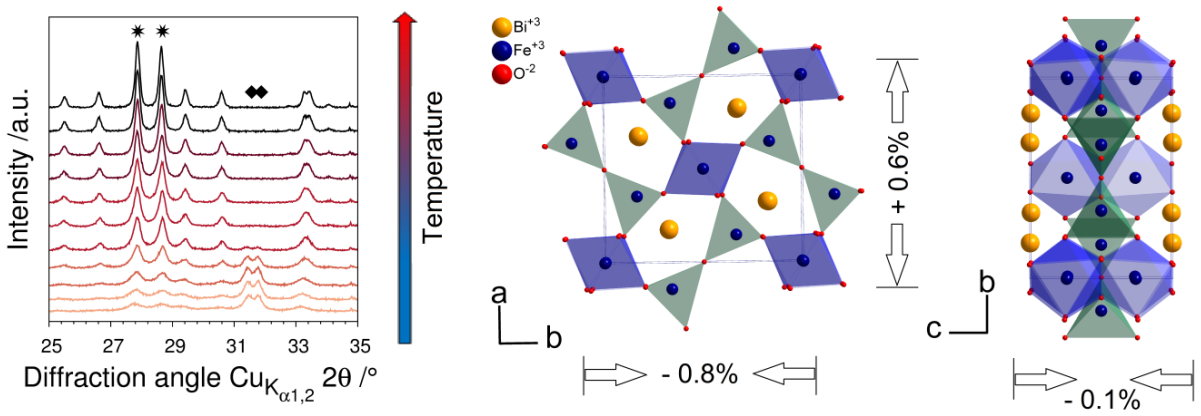

Figure 2. *Left panel*: *In-situ* XRD patterns, where the arrow shows the increase of temperature from 780 K to 980 K at 20 K step. Characteristic intense reflections of $Bi_2Fe_4O_9$ (*121*, *211*) and $BiFeO_3$ (*104, 110*) are shown by stars and diamonds, respectively. *Middle and right panel*: Total changes of metric parameters between 780 K and 980 K.

The pseudo-sigmoid behavior shows that the ACS slightly increases to 46(1) nm until 920 K when the system comprises of the highest micro-strain. Afterward, the steep decrease of the micro-strain follows the steep increase of the ACS till 1120 K. The *b*- and *c*-cell parameters contract, whereas the *a*-cell parameter expands up to 920 K followed by an asymptotic saturation. On the other hand, the *c*-cell parameter steeply contracts to a lowest value at about 850 K and expands afterward. The anisotropic changes of the cell parameters lead to a parabolic change of the cell volume with a trough at 920 K. The lattice thermal expansion of the bulk $Bi_2Fe_4O_9$ material is known to be anisotropic along with positive thermal expansion coefficients (TECs).[37] However, the observed *in-situ* phenomenon cannot be directly compared since below 920 K both formation kinetics and grain coarsening occur influenced by the temperature-dependent changes of the interfacial energy and mass transport. Afterward, the ACS successively increases, indicating that the structural features change during the formation and coarsening of $Bi_2Fe_4O_9$, which may strongly differ from those of the bulk material.

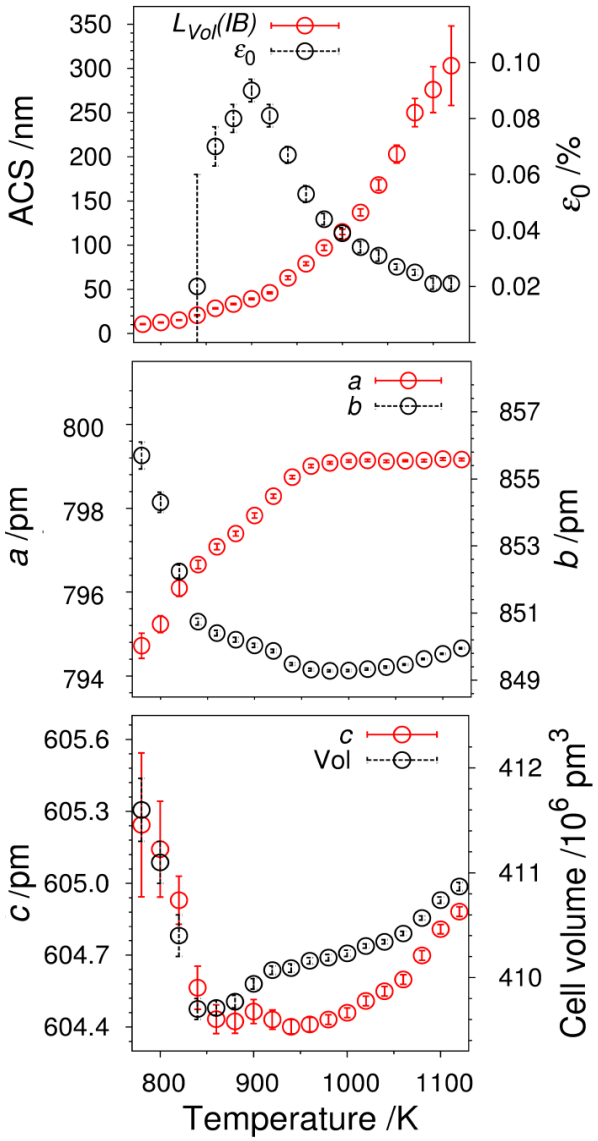

Figure 3. Average crystallite size (ACS) and micro-strain (ε_0) (*upper panel*), and metric parameters (*middle and lower panel*) of $Bi_2Fe_4O_9$ obtained from *in situ* XRD data while heating the sample between 780 K and 1120 K.

Ex-situ XRD

The XRD powder patterns of twelve $Bi_2Fe_4O_9$ samples, obtained by *ex-situ* heating of the precursors at different temperatures between 900 K and 1073 K for 2 h, are shown in Figure S1. Plotting the structural features against the calcination temperature at ambient conditions shows almost similar behaviors as seen in the *in-situ* condition (Figure 3). The ACS increases with higher calcination temperature. This method is limited to produce pure sample below 35.3(4) nm by using a calcination temperature of 900 K.

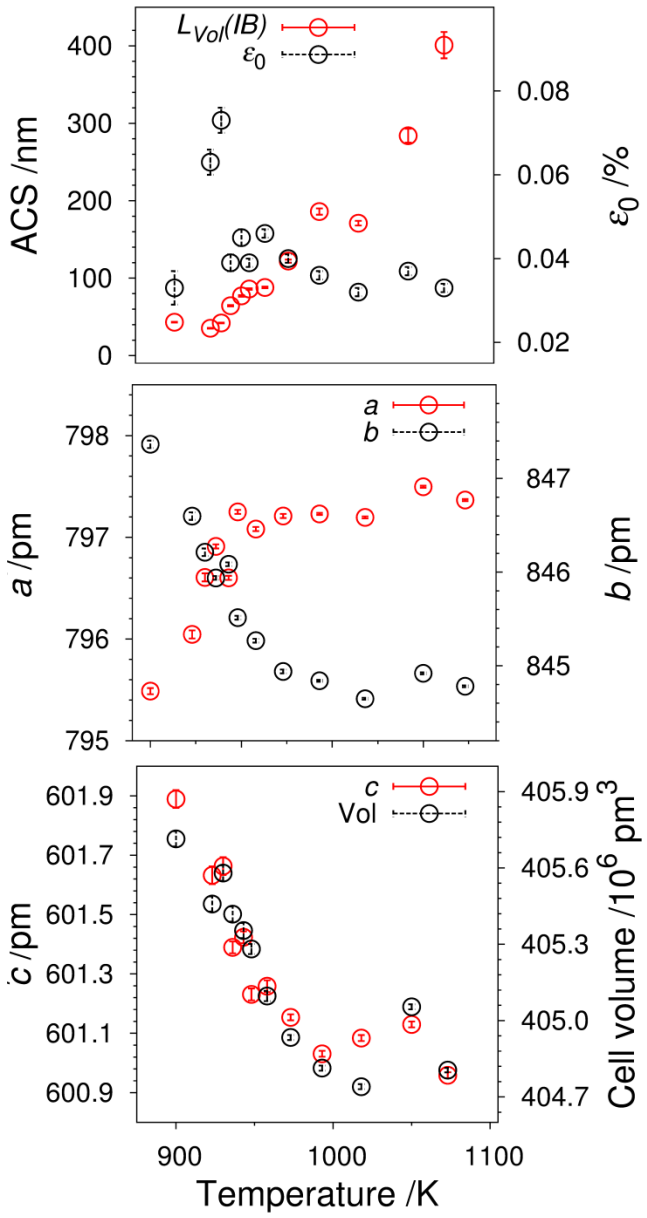

Figure 4. Changes of the average crystallite size (ACS) and microstrain (ε0) (*upper panel*), and metric parameters as function of calcination temperature (*middle and lower panel*). Each sample was calcined at different temperatures from 900 K to 1073 K for 2 h.

Below this critical temperature the perovskite $BiFeO_3$ phase[34] is not fully converted into $Bi_2Fe_4O_9$. The micro-strain first increases and then decreases with increasing the calcination temperature. Within a difference of 120 K, the *a*-, *b*- and *c*-cell parameters change +0.2%, -0.3% and -0.2%, respectively, leading to a cell volume contraction of 0.2%. It is noteworthy to mention that although each sample was found to be X-ray pure Raman as well as ^{57}Fe Mössbauer spectra identified slight X-ray amorphous impurities. Figure 5 shows a comparative view between the *in-situ* and *ex-situ*

parameters regarding the ACS. The deviating between the corresponding parameters can be explained by size-dependent thermal expansion, and the effect is more significant for samples with ACS below ~ 100 nm. Moreover, since samples are synthesized under different conditions (see below), a straightforward comparison may not work.

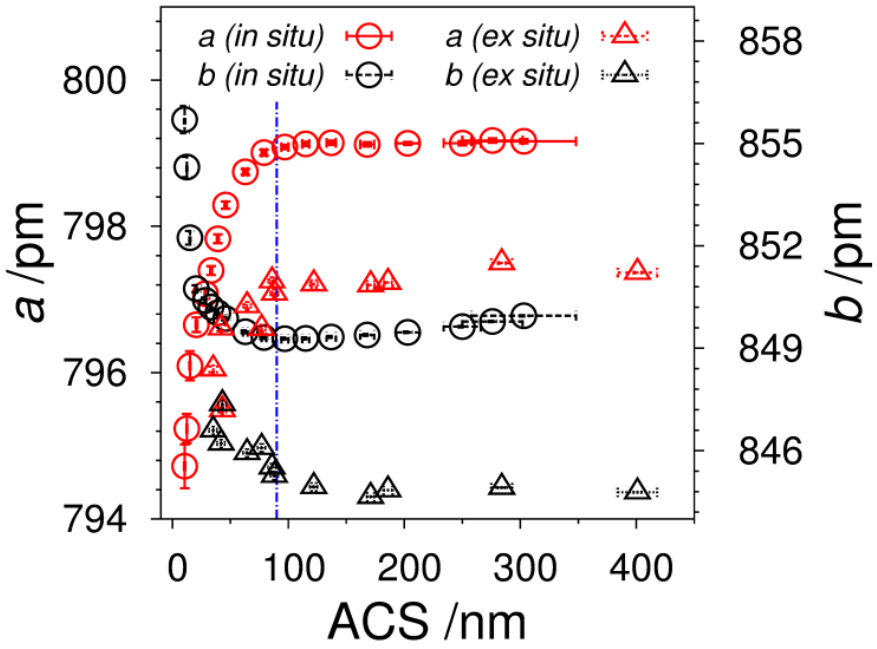

Figure 5. Comparison between selected *in-situ* and *ex-situ* parameters of $Bi_2Fe_4O_9$ obtained from X-ray powder diffraction data Rietveld refinements.

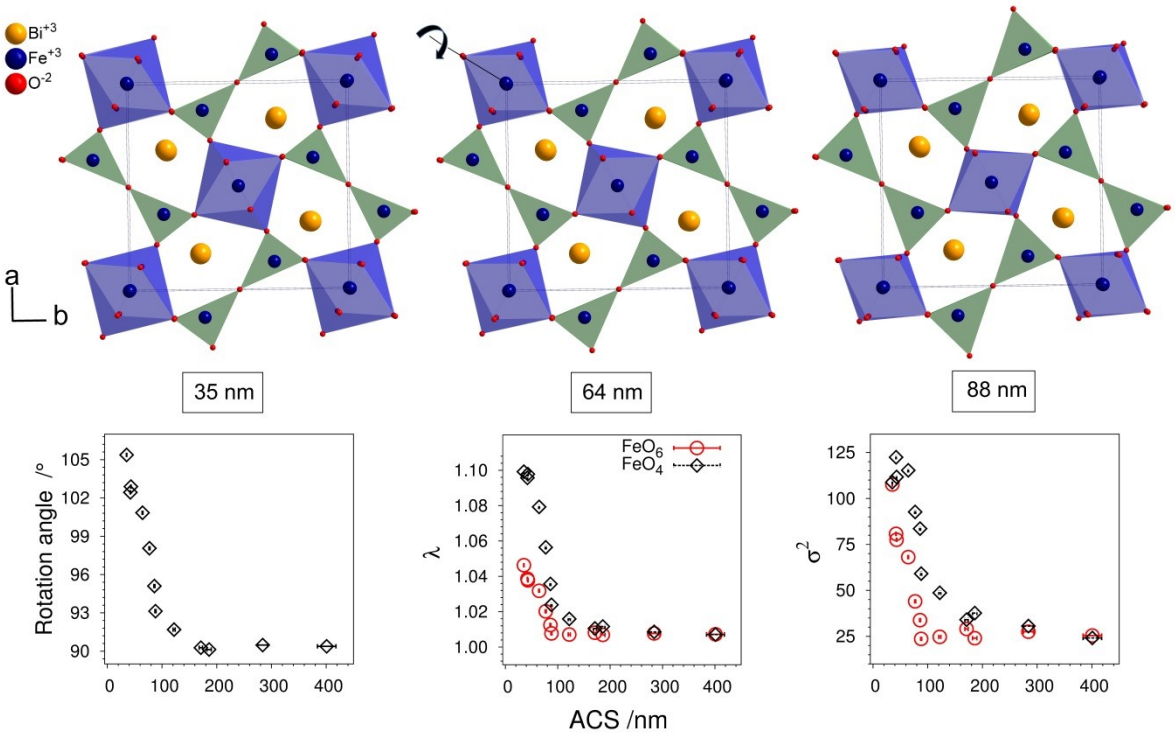

Figure 6. Visualization of polyhedral distortions of $Bi_2Fe_4O_9$ with different average crystallite sizes (ACS). *Left panel*: Development of the octahedral rotation angle. *Middle panel*: Quadratic elongation (λ) of the octahedral (FeO_6) and tetrahedral unit (FeO_4). *Right panel*: Bond angle variance (σ^2) of the FeO_6 and FeO_4 polyhedra.

To get an in-depth picture how the structural features evolve for samples with ACS below ~100 nm Figure 6 gives a visual guideline. Both the FeO_4 and FeO_6 polyhedra possess strong distortion indices such as quadratic elongation (λ) and angle variance (σ^2).[38] The rotation angle of the edge built by O(11) and O(12) (Figure 1) and the (002) crystallographic plane is found to be ~105 ° for the sample with the smallest ACS of 35.3(4) nm, which is 14 ° higher than that of the ACS of 122(2) nm, which lies close to the bulk structure value of ~91 °. At a given ACS < 100 nm both the λ and σ^2 in the FeO_4 tetrahedral units are more pronounced than those in the FeO_6 octahedra. With increasing ACS (due to increased calcination temperature) the strong distortions observed for the smaller ACS samples (Figure 6) steeply decrease till the sample comprises of an ACS of ~100 nm. The strong distortions and their diminution at 122(2) nm (prepared at 973 K) can be correlated to changes of the *a*- and *b*-cell parameters during the formation of the $Bi_2Fe_4O_9$ crystallites (Figure 5). Such ACS-dependent expansion behaviors are also observed for other oxide lattices such as in CeO_{2-x}[39], $BaTiO_3$[40], $PbTiO_3$[41] and TiO_2[42] at smaller (< 10 nm for CeO_{2-x}[39], TiO_2[42]) and larger (< 100 nm for $BaTiO_3$[40], $PbTiO_3$[41]) ACSs.

3.2. Transmission electron microscopy

To crosscheck the ACSs determined by XRD and to get an idea on the shape and distribution of the crystallite domains we characterized three selected samples (35.3(4) nm, 88(1) nm, 401(17) nm) using TEM. From the collected 2D images the corresponding mean diameters are estimated to be 36(8) nm, 85(14) nm and 407(86) nm, respectively, which are surprisingly similar to the corresponding ACSs obtained from the XRD results.[31] The higher uncertainty for larger ACSs can be attributed to statistical samplings (e.g., neglecting the possible tail of the lognormal distribution). The micrographs show the typical appearance of the powder samples as depicted in **Figure 7**. The morphologies of the powders significantly change with calcination temperature. While the samples with the smaller ACSs (35.3(4) nm and 88(1) nm) consist of large agglomerates with smaller sintered spherical nano-crystallites, the sample with 401(17) nm exhibits distinct crystal habits. The histograms of the crystallite size distributions of the samples are also presented (**Figure 7**). In each case, the maximum size difference does not exceed 35% from either side of the mediaen, indicating rather a narrow normal size distribution (Gaussian) of the observed samples.

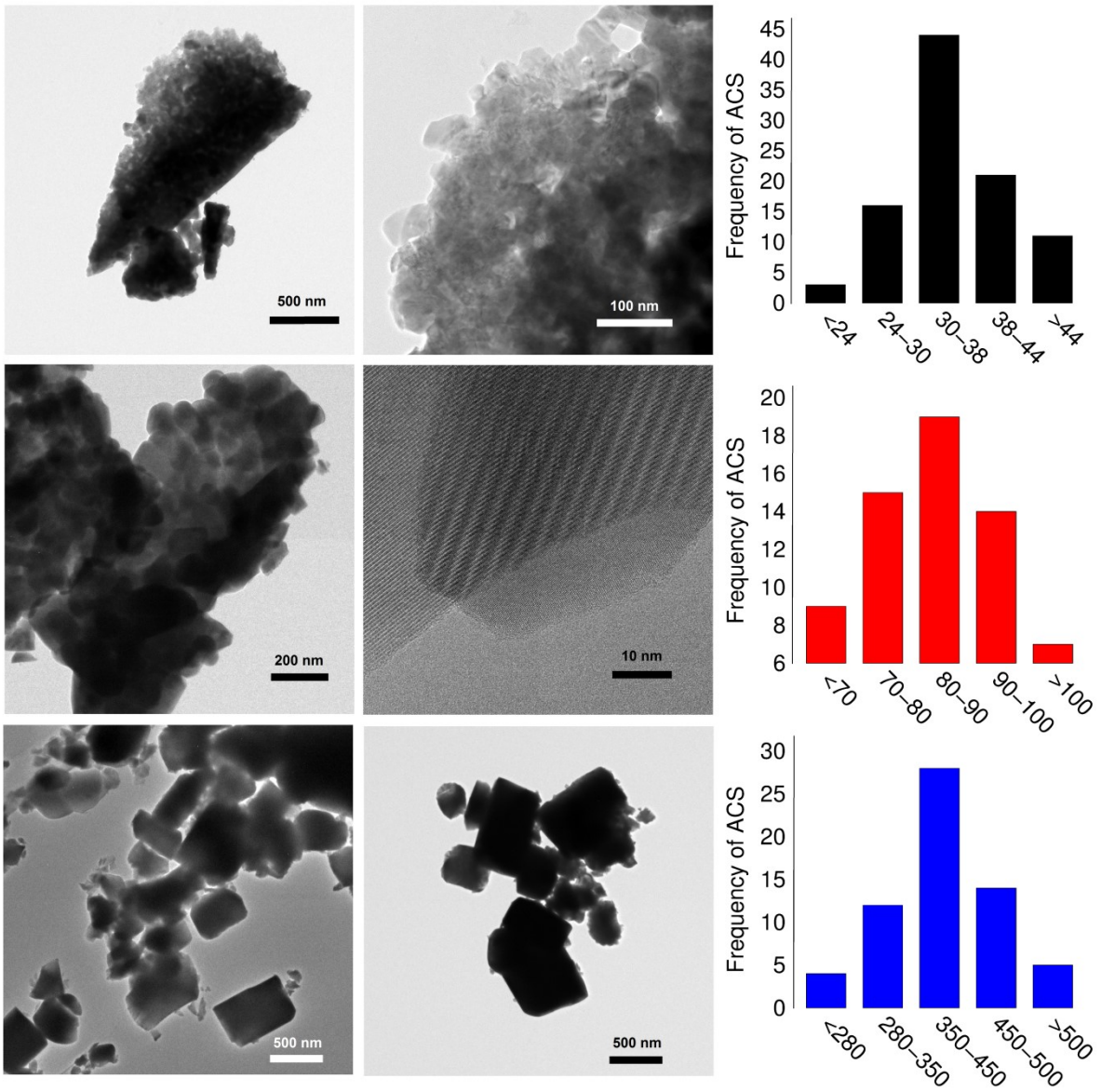

Figure 7. TEM micrographs and corresponding histograms of $Bi_2Fe_4O_9$ samples with average crystallite sizes (ACSs) of 35.3(4) nm (top), 88(1) nm (middle) and 401(17) nm (bottom).

3.3. Spectroscopy

Raman spectroscopy

The Raman spectra recorded at ambient conditions exhibit well-resolved modes for the $Bi_2Fe_4O_9$ phase[24] as shown in Figure S2 (Supplementary Information). In some samples a weak mode at 292 cm^{-1} was assigned to Fe_2O_3[43]. The amount (domain size) is beyond the coherent length of the X-ray radiation, however, enough to be traced by the microfocus vibrational spectroscopy.[34]

Phenomena such as phonon confinement/relaxation, microstrain, ACS size distribution, phonon and oxygen vacancies can contribute to the change of peak positions and full-width at half-maxima (FWHM) of the Raman modes.[44] The frequency and FWHM of all the well-resolved modes show a clear dependence on the ACS. There is as much as 44(1)% changes of the FWHM of the mode at ~552 cm^{-1} for an ACS difference between 35 nm and 400 nm as depicted in Figure 8. The ACS-dependent softening of selected phonon modes can also be seen (Figure S2, Table S1). Notably, the trends observed in the Raman spectra (Figure 8) are in direct accordance with the changes of the metric parameters (Figure 5) as well as the polyhedral distortions (Figure 6) determined by XRD.

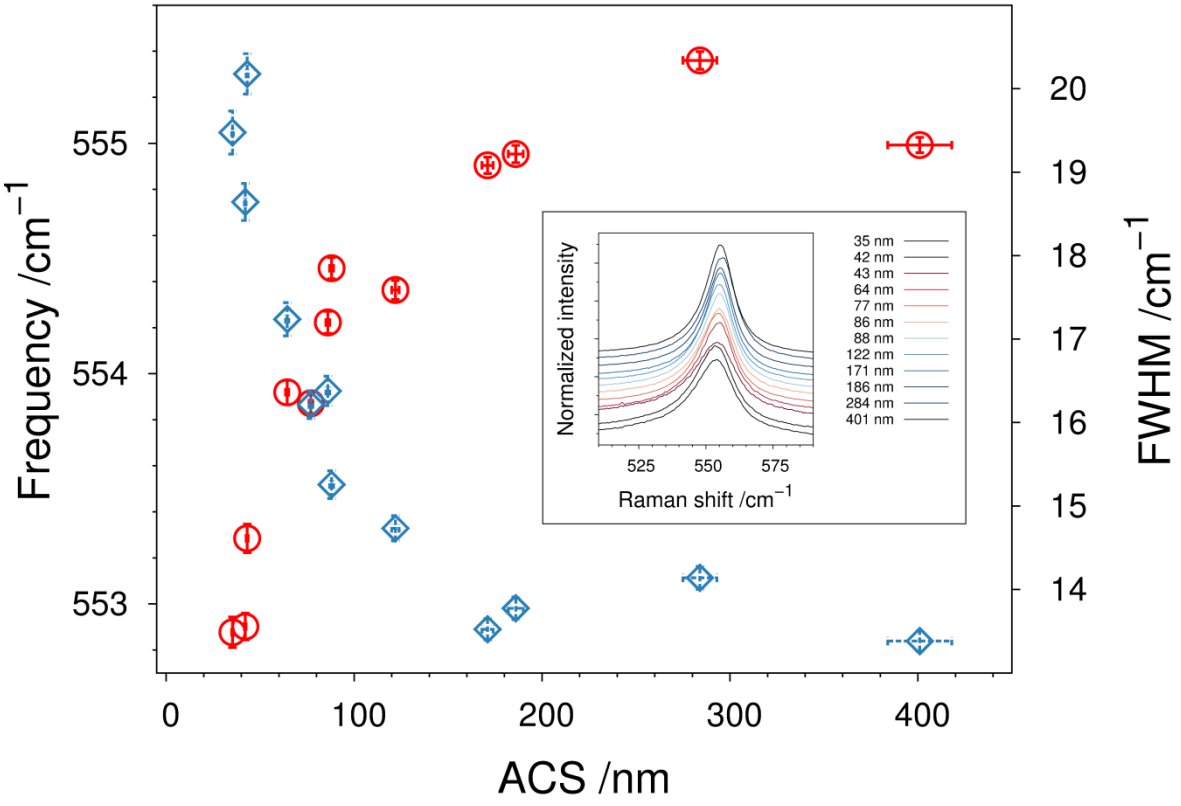

Figure 8. Raman mode of $Bi_2Fe_4O_9$ at 552 cm^{-1} (inset) with the corresponding changes of frequency and FWHM as function of average crystallite size (ACS).

Spanier et al.[44] also observed a concomitant Raman peak shift and change in FWHM for CeO_{2-y}. They attributed the decrease of frequency and concomitant increase of linewidth to the combined effects of strain and phonon confinement based on performed simulations.

Of interesting notes, the mode softening is found to particularly increase when the frequency is increased (see Table S1) in spite the mode at ~110 cm^{-1}. In the high frequency region mainly oxygen motions are involved.[24] In addition, temperature-dependent Raman spectra of three samples with significantly different ACS of 35.3(4) nm, 88(1) nm and 401(17) nm were recorded from 200 to 350 K in 10 K steps. Representative modes of the low, middle and high frequency regime at 110, 283 and 552 cm^{-1} were followed as a function of temperature as can be seen in Figure S3. The three modes followed soften when the sample is heated from 200 K to 350 K of about 1.12% / 1.13% at ~110 cm^{-1}, 0.70% / 0.58% at ~283 cm^{-1} and 0.95% / 0.96% at ~552 cm^{-1} for the sample with an ACS of 35.3(4) nm / 401(17) nm, respectively. In general, the temperature dependences of the modes are quite similar for both samples except of an offset. As in the room-temperature spectra it is evident that the band positions differ substantially showing an increase in energy as the ACS increases. The opposite effect is seen in the FWHM of the modes which sharpen strongly when the ACS is increasing. Of particular notes, the temperature has a much smaller effect on the FWHM's than the ACS. The peaks of the sample with ACS of 401(17) nm at 350 K are not even as broad as the ones at 200 K of the 35.3(4) nm sample.

Mössbauer spectroscopy

Temperature-dependent ^{57}Fe Mössbauer spectra of the samples with ACSs of 35.3(4) and 401(17) nm are shown in Figure 9.

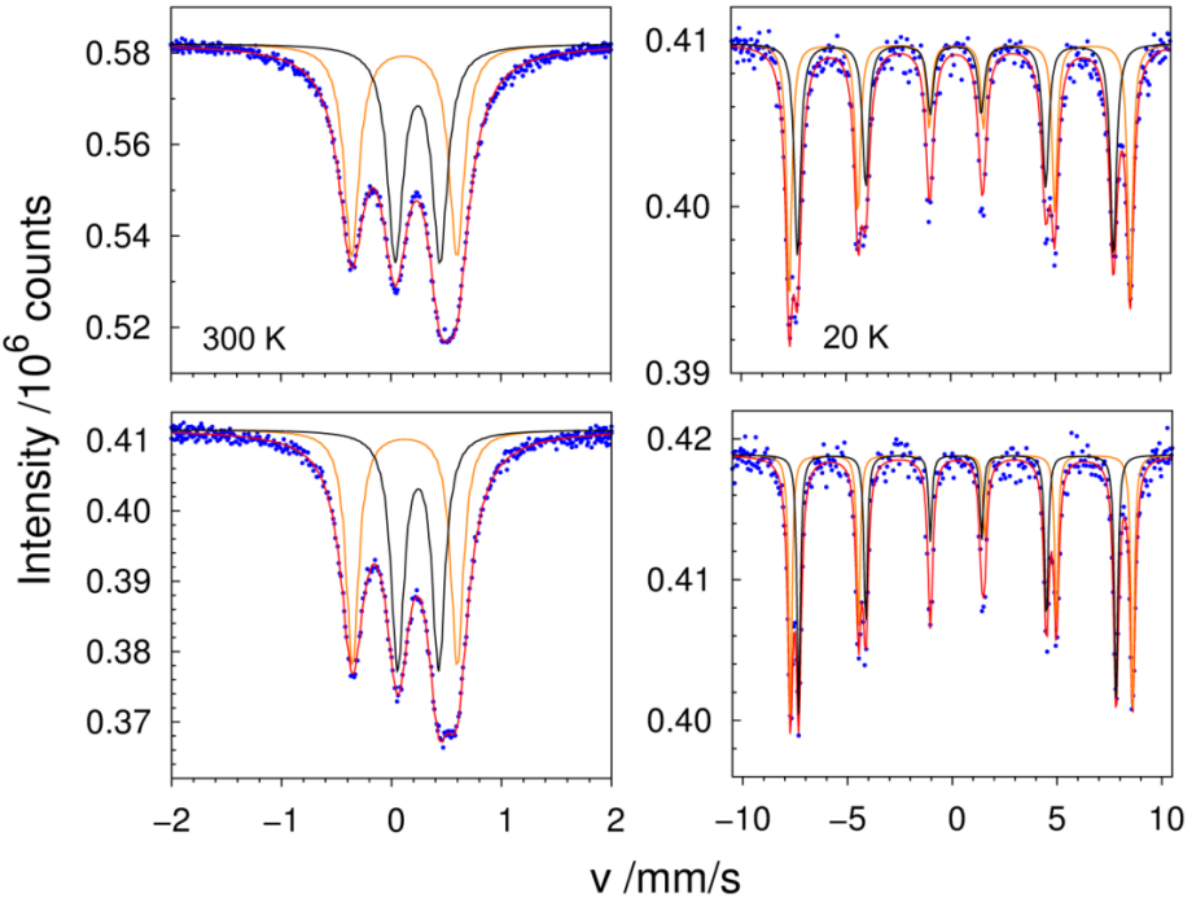

Figure 9. Representative Mössbauer spectra of $Bi_2Fe_4O_9$ with average crystallite sizes (ACS) of 35 nm (*upper panels*) and 401 nm (*lower panels*) at 300 K and 20 K, respectively.

In some samples a small amount (% range) of impurities, as also identified by Raman, can be attributed to γ-Fe_2O_3 from its magnetic hyperfine pattern. The low-temperature spectra were collected below T_N to get a comparative view between the antiferromagnetic and the paramagnetic phases of the size-dependent compounds. The spectra at 300 K show typical equally distributed doublets for the FeO_4 tetrahedral and FeO_6 octahedral units of the paramagnetic $Bi_2Fe_4O_9$. The low-temperature spectra can be deconvoluted with two static magnetic sextets for all the samples. The hyperfine parameters obtained from the fittings of the spectra are given in Table S2 and visualized in Figure 10. The room temperature isomer shifts of

0.231(2) mm/s and 0.352(2) mm/s, respectively, for the tetrahedral (IS_T) and the octahedral (IS_O) units of the 401(17) nm sample agree well with those of the bulk $Bi_2Fe_4O_9$.[45-47] The quadrupolar splitting (QS) values for both the FeO_4 tetrahedra and FeO_6 octahedra steeply increase for samples with ACS < 122(2) nm. Since a QS value of coordinated Fe^{3+} is directly proportional to the degree of distortion[48], this observed trend is supported by the XRD (Figure 5) and the Raman (Figure 8) results. In general, the Mössbauer spectral linewidths (for tetrahedra Γ_T and octahedra Γ_O) increase with the decrease of the ACS. The values of the hyperfine magnetic fields (B_{hf}) obtained from the spectra agree well with those reported by Papaefthymiou et al. (2015)[47]. Again, a significant decrease is observed for ACS < 122(2) nm followed by an asymptotic saturation (Figure 10). For trivalent iron the variations of QS with temperature are weak. However, the $QS_{T,O}$ at 20 K are substantially smaller than those at 300 K. This can be explained by an angle (θ) between B_{hf} and the main component of the electric field gradient (V_{zz}). For determining this angle, we assumed axial symmetry and fixed the values of QS to those determined at 300 K (both assumptions have only minor influence on the qualitative result). The angle significantly changes for both the tetrahedral (~ 6%) and the octahedral (~ 13%) coordinations when the ACS drops below 122(2) nm (Figure 10). In agreement with our other findings, some previous studies reported on an enhanced ferromagnetic nature of $Bi_2Fe_4O_9$[14,49,50], which could be related to the significantly changed local spin orientation in comparison with the bulk counterpart. In our study, such behaviour could be induced by strong polyhedral distortions below this critical size (Figure 6), leading to change the direct- or super-exchange interactions in the $Bi_2Fe_4O_9$ structure.[27] In contrast to the other hyperfine parameters the isomer shifts are apparently insensitive to changes of ACS. Reason is probably the relatively small change in cell volume from which one can expect changes in isomer shift on the order of only 0.01 mm/s that is within the range of error bars.

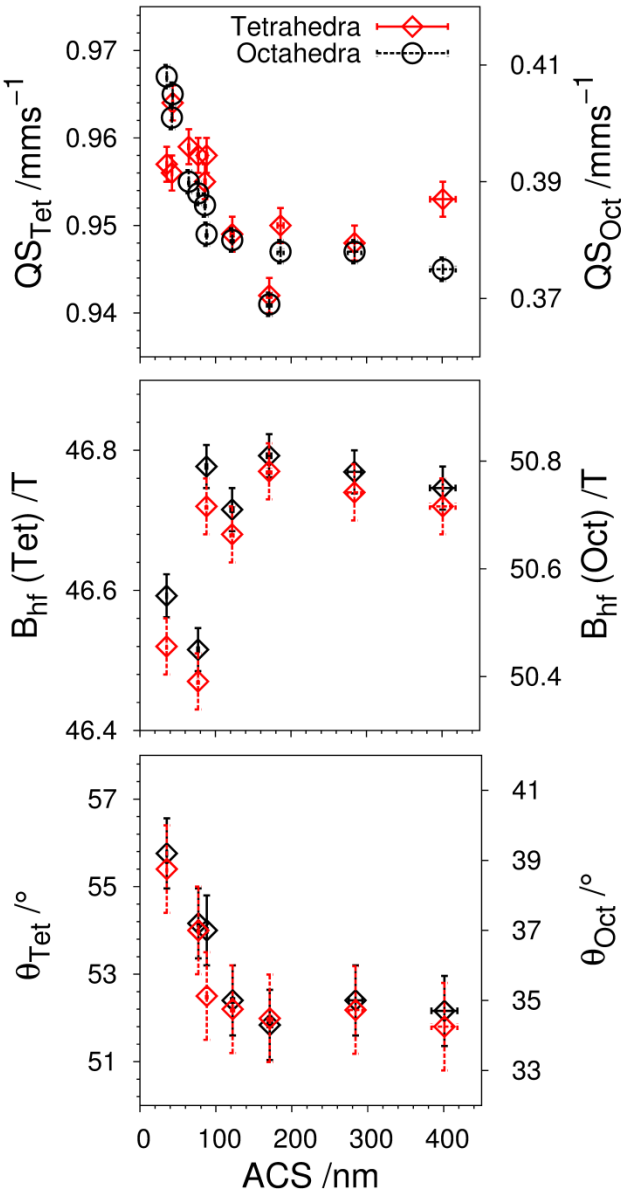

Figure 10. Hyperfine parameters of ^{57}Fe Mössbauer spectra of $Bi_2Fe_4O_9$ powders as function of average crystallite size (ACS). *Upper panel*: Quadrupolar splitting (QS) of the tetrahedral and octahedral units measured at 300 K. *Middle panel*: B_{hf} measured at 20 K. *Right panel*: Angle (θ) between hyperfine magnetic field (B_{hf}) and the main component of the electric field gradient (V_{zz}) measured at 20 K (QS fixed to its value at 300 K).

Diffuse UV/Vis reflectance spectroscopy

The diffuse reflectance UV/Vis spectra of the bulk $Bi_2Fe_4O_9$ samples show two distinct absorption edges –a typical feature of this compound.[14,17,34] Kubelka - Munk transformation and the Tauc relationship[51] (assuming direct transitions)[34] are used to calculate the band gaps of the samples with ACSs from 35.3(4) nm to 401(17) nm.

The determined values between 2.1 eV and 2.3 eV are in close agreement with the reported ones.[13,18,34,49,52] The trend of the band gap as function of ACS as seen in Figure 11 clearly contradicts with the observed[14] one where the ACSs of the nanomaterials are limited to 14 - 78 nm.

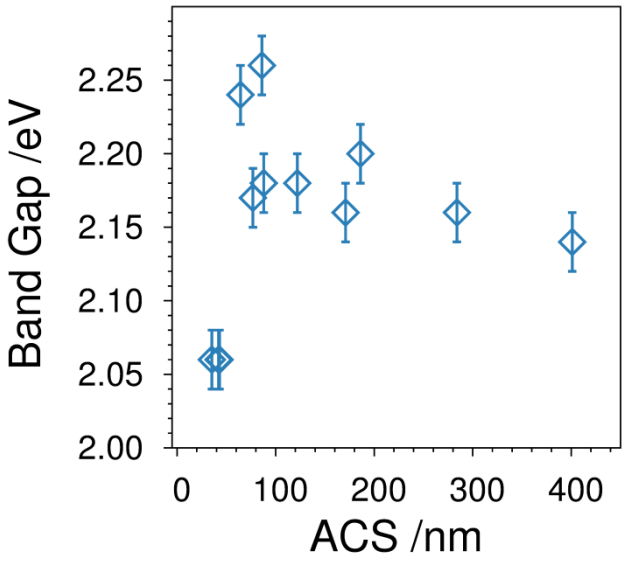

Figure 11. Average crystallite size (ACS)-dependent band gap of $Bi_2Fe_4O_9$ with estimated standard deviations.

While the main absorption edge of the samples differs with ACSs, the 2nd absorption edge remains almost constant at 1.61(1) eV. Taking the normalized intensity of the reflectance spectra, the maximum of this absorption feature follows a red-shift along with increased intensity with increasing ACS as shown in Figure S4 (Supporting Information). The color of the powder samples changes as the calcination temperature changes as seen in Figure 12. Wu et al.[50] observed a darker color with a greater ACS (with no explicit ACS value), suggesting a smaller band gap. We observed a similar trend, however with dark brown - lighter brown back - darker brown (Figure 12).

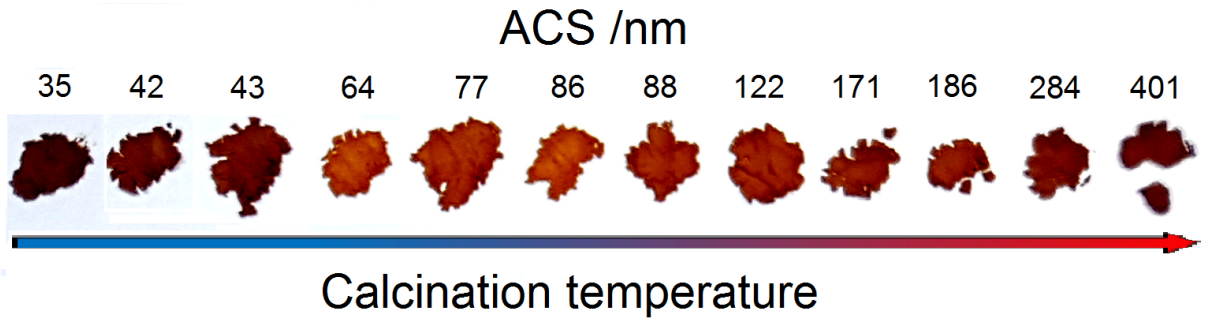

Figure 12. Optical appearance of the samples with different average crystallite sizes (ACS).

Yang et al.[18] who modified the optical properties through the etching time also observed the color changes. In a recent study on mullite-type $Bi_2(Al_{1-x}Fe)_4O_9$[53] the intensity of the 2nd absorption maximum was found to be a function of Al/Fe ratio, which completely disappeared in $Bi_2Al_4O_9$. It is therefore clear that the observed 2nd absorption edge is caused by the *d*-*d*-transitions of the Fe^{3+} cations.[53]

Infrared

The ACS-dependent FTIR spectra are shown in Figure S5. The observed band frequencies at ambient conditions are in excellent agreement with those of the earlier observations.[34,46,54] In the present study, we particularly follow the Fe-O-Fe stretching[54] features of the Fe_2O_7 double-tetrahedra[55,56] observed at ~ 813(1) cm^{-1} with respect to the ACSs. It was already observed that the 2nd absorption edge of the UV/Vis reflectance spectra depends on this mode (see above).[34] Using the normalized spectra (Figure S5) the band frequency at 813(1) cm^{-1} is independent of the ACS. The intensity, however, increases with increasing ACS. A correlation between the intensity of the 2nd absorption edge of the UV/Vis reflectance spectra and the intensity of the FTIR band at 813(1) cm^{-1} is shown in Figure S6.

3.4. DSC

To determine phase-transitions each sample was cooled down to 200 K and heated up to 350 K in three consecutive cycles using difference scanning calorimetry. The temperature dependence of the heat flow for a representative sample with ACS of 284(9) nm is shown in Figure 13.

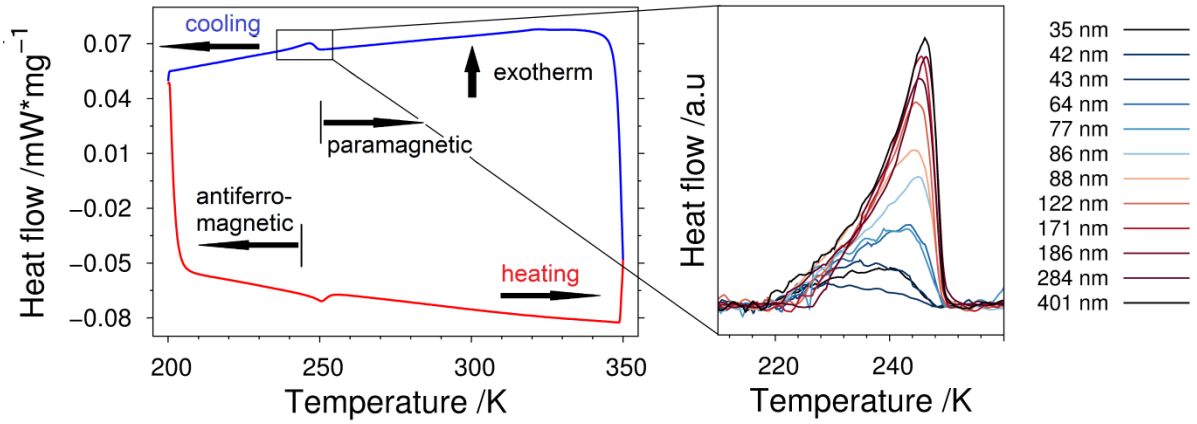

Figure 13. *Left panel*: Differential scanning calorimetry (DSC) curves of the powder sample $Bi_2Fe_4O_9$ with average crystallite size (ACS) of 284(9) nm. *Right panel*: The exothermic peak for samples with ACS from 35.3(4) – 401(17) nm.

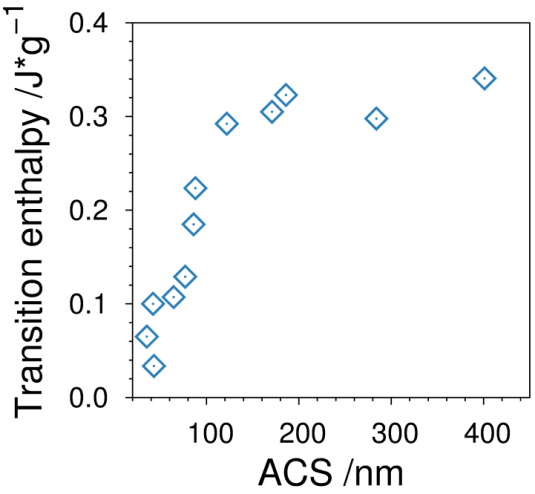

Figure 14. Transition enthalpy as a function of average crystallite size (ACS).

Exothermic and endothermic peaks were observed, respectively, during cooling and heating the samples due to corresponding paramagnetic into antiferromagnetic transition. The Néel-temperature T_N was obtained to be 249.5(2) K for ACS > 43 nm and 247.5(2) K for ACS < 43 nm. A small thermal hysteresis of about 3.5 K – 5 K could be observed for this transition. The T_N is determined using the intersection of the baseline and the tangent line with the largest slope of the DSC peak (Figure 13); the values are in good agreement with reported ones.[19,24-26] The transition enthalpy of the magnetic transition significantly changes as a function of ACS (Figure 14). In other words, the energy released by the system due to antiferromagnetic ordering increases with increasing ACS. Again, significant changes occur for samples with

ACS below 122(2) nm, which is a critical ACS, already established by XRD, Raman and Mössbauer spectra. This leads us to argue that the spin ordering/interactions involved in the system are different for ACS below and above the critical size of 122(2) nm. Indeed, earlier studies of the $Bi_2Fe_4O_9$ structure showed weak ferromagnetic behavior for samples with small ACSs.[12,14,47,49,50,57] Han et al.[57] attributed these findings to be caused by the spin canting of Fe^{3+}, which was supported by temperature-dependent zero-field-cooled (ZFC) and field-cooled (FC) susceptibility measurements showing a remarkable thermomagnetic irreversibility.[57] The steep decrease in intensity below 122(2) nm could be related to some (partial) ferromagnetic domains with no intense feature in DSC. Because the characteristic ferromagnetic peaks in DSC are not as intense as that of antiferromagnetic or ferrimagnetic materials due to the fact that ferromagnetic and antiferromagnetic ordering are of second-order and first-order types Landau phase transitions.[58] In the magnetic structure of the bulk $Bi_2Fe_4O_9$ both ferromagnetic and antiferromagnetic superexchange interactions are already present. Therefore, the strong polyhedral distortions (Figure 6, Figure 10) could cause Fe^{3+} spin canting, leading to increased ferromagnetic domains below the critical size. Moreover, the *a*- and *b*-cell parameters are significantly influenced by the ACS whereas the rigid FeO_6 octahedral chains in the **c**-direction are not so far influenced. In fact, the strongest antiferromagnetic superexchange interaction is restricted to the FeO_4 tetrahedral unit in the ab-plane, whereas the ferromagnetic coupling takes place in the **c**-direction.[28]

4. Conclusion

The nano-properties of mullite-type $Bi_2Fe_4O_9$ significantly differ below and above the critical average crystallite size (ACS) of 110(10) nm evidenced by X-ray diffraction, Raman, infrared, UV/Vis, Mössbauer spectroscopy and differential scanning calorimetry (DSC). Strong distortions of the polyhedral units lead to a substantial changed local spin orientation in the samples below 122(2) nm in comparison with bulk $Bi_2Fe_4O_9$. The intensity of the second absorption edge of the UV/Vis spectrum depends on the size-dependent distortion of the FeO_4 tetrahedral units.

Acknowledgement

We gratefully acknowledge the TEM measurements of Dr. Marco Schowalter and Prof. Dr. Andreas Rosenauer (Institute of Solid State Physics, University of Bremen). AK thanks University of Bremen for financial support.

References

(1) Tachibana, Y.; Vayssieres, L.; Durrant, J. R. Artificial Photosynthesis for Solar Water-Splitting. *Nat. Photonics* **2012**, *6* (8), 511–518.
(2) Žutić, I.; Fabian, J.; Sarma, S. Das. Spintronics: Fundamentals and Applications. *Rev. Mod. Phys.* **2004**, *76* (2), 323–410.
(3) Liu, C.; Li, F.; Ma, L.-P.; Cheng, H.-M. Advanced Materials for Energy Storage. *Adv. Mater.* **2010**, *22* (8), E28–E62.
(4) Lan, X.; Masala, S.; Sargent, E. H. Charge-Extraction Strategies for Colloidal Quantum Dot Photovoltaics. *Nat. Mater.* **2014**, *13* (3), 233–240.
(5) Majdoub, M. S.; Sharma, P.; Cagin, T. Enhanced Size-Dependent Piezoelectricity and Elasticity in Nanostructures due to the Flexoelectric Effect. *Phys. Rev. B* **2008**, *77* (12), 125424-1–9.
(6) Park, T.; Papaefthymiou, G. C.; Viescas, A. J.; Moodenbaugh, A. R.; Wong, S. S. Size-Dependent Magnetic Properties of Single-Crystalline Multiferroic $BiFeO_3$ Nanoparticles. *Nano Lett.* **2007**, *7* (3), 766–772.
(7) Sichert, J. A.; Tong, Y.; Mutz, N.; Vollmer, M.; Fischer, S.; Milowska, K. Z.; García Cortadella, R.; Nickel, B.; Cardenas-Daw, C.; Stolarczyk, J. K.; et al. Quantum Size Effect in Organometal Halide Perovskite Nanoplatelets. *Nano Lett.* **2015**, *15* (10), 6521–6527.
(8) Liu, Y.; Lockman, Z.; Aziz, A.; MacManus-Driscoll, J. Size Dependent Ferromagnetism in Cerium Oxide (CeO_2) Nanostructures Independent of Oxygen Vacancies. *J. Phys. Condens. Matter* **2008**, *20* (16), 165201.
(9) Xuan, S.; Wang, Y.-X. J.; Yu, J. C.; Cham-Fai Leung, K. Tuning the Grain Size and Particle Size of Superparamagnetic Fe_3O_4 Microparticles. *Chem. Mater.* **2009**, *21* (21), 5079–5087.
(10) Venkatesan, M.; Fitzgerald, C. B.; Coey, J. M. D. Unexpected Magnetism in a Dielectric Oxide. *Nature* **2004**, *430* (7000), 630.
(11) Sundaresan, A.; Bhargavi, R.; Rangarajan, N.; Siddesh, U.; Rao, C. N. R. Ferromagnetism as a Universal Feature of Nanoparticles of the Otherwise Nonmagnetic Oxides. *Phys. Rev. B* **2006**, *74* (16), 161306-1–4.
(12) Tian, Z. M.; Yuan, S. L.; Wang, X. L.; Zheng, X. F.; Yin, S. Y.; Wang, C. H.; Liu, L. Size Effect on Magnetic and Ferroelectric Properties in $Bi_2Fe_4O_9$ Multiferroic Ceramics. *J. Appl. Phys.* **2009**, *106* (10), 103912.
(13) Li, Y.; Zhang, Y.; Ye, W.; Yu, J.; Lu, C.; Xia, L. Photo-to-Current Response of $Bi_2Fe_4O_9$ Nanocrystals Synthesized through a Chemical Co-Precipitation Process. *New J. Chem.* **2012**, *36* (6), 1297–1300.
(14) Zhang, Q.; Gong, W.; Wang, J.; Ning, X.; Wang, Z.; Zhao, X.; Ren, W.; Zhang, Z. Size-Dependent Magnetic, Photoabsorbing, and Photocatalytic Properties of Single-Crystalline $Bi_2Fe_4O_9$ Semiconductor Nanocrystals. *J. Phys. Chem. C* **2011**, *115*, 25241–25246.
(15) Zakharchenko, N. I. Catalytic Properties of the System Fe_2O_3 - Bi_2O_3 in Ammonia Oxidation to Nitrogen Oxides. *Kinet. Catal.* **2002**, *43* (3), 95–98.

(16) Poghossian, A. S.; Abovian, H. V.; Avakian, P. B.; Mkrtchian, S. H.; Haroutunian, V. M. Bismuth Ferrites: New Materials for Semiconductor Gas Sensors. *Sensors Actuators B Chem.* **1991**, *4* (3–4), 545–549.
(17) Sun, S.; Wang, W.; Zhang, L.; Shang, M. Visible Light-Induced Photocatalytic Oxidation of Phenol and Aqueous Ammonia in Flowerlike $Bi_2Fe_4O_9$ Suspensions. *J. Phys. Chem. C* **2009**, *113*, 12826–12831.
(18) Yang, H.; Dai, J.; Wang, L.; Lin, Y.; Wang, F.; Kang, P. A Novel Approach to Prepare $Bi_2Fe_4O_9$ Flower-like Spheres with Enhanced Photocatalytic Performance. *Sci. Rep.* **2017**, *7* (1), 768.
(19) Singh, A. K.; Kaushik, S. D.; Kumar, B.; Mishra, P. K.; Venimadhav, A.; Siruguri, V.; Patnaik, S. Substantial Magnetoelectric Coupling near Room Temperature in $Bi_2Fe_4O_9$. *Appl. Phys. Lett.* **2008**, *92* (13), 132910.
(20) Wu, X. H.; Miao, J.; Zhao, Y.; Meng, X. B.; Xu, X. G.; Wang, S. G.; Jiang, Y. Novel Multiferroic $Bi_2Fe_4O_9$ Nanoparticles: The Interesting Optical, Photocatalytic, and Multiferroic Properties. *Optoelectron. Adv. Mater. Rapid Commun.* **2013**, *7* (1–2), 116–120.
(21) Koizumi, H.; Niizeki, N.; Ikeda, T. An X-Ray Study on Bi_2O_3-Fe_2O_3 System. *Jpn. J. Appl. Phys.* **1964**, *3*, 495–496.
(22) Schneider, H.; Fischer, R. X.; Gesing, T. M.; Schreuer, J.; Mühlberg, M. Crystal Chemistry and Properties of Mullite-Type $Bi_2M_4O_9$: An Overview. *Int. J. Mater. Res.* **2012**, *103* (4), 422–429.
(23) Curti, M.; Gesing, T. M.; Murshed, M. M.; Bredow, T.; Mendive, C. B. Liebau Density Vector: A New Approach to Characterize Lone Electron Pairs in Mullite-Type Materials. *Zeitschrift für Krist. - Cryst. Mater.* **2013**, *228* (12), 629–634.
(24) Iliev, M. N.; Litvinchuk, A. P.; Hadjiev, V. G.; Gospodinov, M. M.; Skumryev, V.; Ressouche, E. Phonon and Magnon Scattering of Antiferromagnetic $Bi_2Fe_4O_9$. *Phys. Rev. B* **2010**, *81* (2), 24302.
(25) Papaefthymiou, G. C.; Viescas, A. J.; Le Breton, J.-M.; Chiron, H.; Juraszek, J.; Park, T.-J.; Wong, S. S. Magnetic and Mössbauer Characterization of the Magnetic Properties of Single-Crystalline Sub-Micron Sized $Bi_2Fe_4O_9$ Cubes. *Curr. Appl. Phys.* **2015**, *15* (3), 417–422.
(26) Shamir, N.; Gurewitz, E.; Shaked, H. The Magnetic Structure of $Bi_2Fe_4O_9$ - A Neutron Diffraction Study. **1978**, *7* (c), 66–68.
(27) Ressouche, E.; Simonet, V.; Canals, B.; Gospodinov, M.; Skumryev, V. Magnetic Frustration in an Iron-Based Cairo Pentagonal Lattice. *Phys. Rev. Lett.* **2009**, *103* (26), 267204.
(28) Pchelkina, Z. V.; Streltsov, S. V. Ab Initio Investigation of the Exchange Interactions in $Bi_2Fe_4O_9$: The Cairo Pentagonal Lattice Compound. *Phys. Rev. B* **2013**, *88* (5), 54424.
(29) Balzar, D.; Audebrand, N.; Daymond, M. R.; Fitch, A.; Hewat, A.; Langford, J. I.; Le Bail, A.; Louër, D.; Masson, O.; McCowan, C. N.; et al. Size–strain Line-Broadening Analysis of the Ceria Round-Robin Sample. *J. Appl. Crystallogr.* **2004**, *37* (6), 911–924.
(30) Langford, J. I.; Wilson, A. J. C. Scherrer after Sixty Years: A Survey and Some New Results in the Determination of Crystallite Size. *J. Appl. Crystallogr.* **1978**, *11* (2), 102–113.
(31) Langford, J. I.; Louër, D.; Scardi, P. Effect of a Crystallite Size Distribution on X-Ray Diffraction Line Profiles and Whole-Powder-Pattern Fitting. *Appl. Crystallogr.* **2000**, *33*, 964–974.
(32) Matyi, R. J.; Schwartz, L. H.; Butt, J. B. Particle Size, Particle Size Distribution,

and Related Measurements of Supported Metal Catalysts. *Catal. Rev.* **1987**, *29* (1), 41–99.
(33) Teck, M.; Murshed, M. M.; Schowalter, M.; Lefeld, N.; Grossmann, H. K.; Grieb, T.; Hartmann, T.; Robben, L.; Rosenauer, A.; Mädler, L.; et al. Structural and Spectroscopic Comparison between Polycrystalline, Nanocrystalline and Quantum Dot Visible Light Photo-Catalyst Bi_2WO_6. *J. Solid State Chem.* **2017**, *254*, 82–89.
(34) Kirsch, A.; Murshed, M. M.; Schowalter, M.; Rosenauer, A.; Gesing, T. M. Nanoparticle Precursor into Polycrystalline $Bi_2Fe_4O_9$: An Evolutionary Investigation of Structural, Morphological, Optical, and Vibrational Properties. *J. Phys. Chem. C* **2016**, *120* (33), 18831–18840.
(35) Richard, D.; Ferrand, M.; Kearley, G. Analysis and Visualisation of Neutron-Scattering Data. *J. Neutron Res.* **1996**, *4*, 33–39.
(36) Klencsár, Z. MossWinn 4.0 Manual.
(37) Murshed, M. M.; Nénert, G.; Burianek, M.; Robben, L.; Mühlberg, M.; Schneider, H.; Fischer, R. X.; Gesing, T. M. Temperature-Dependent Structural Studies of Mullite-Type $Bi_2Fe_4O_9$. *J. Solid State Chem.* **2013**, *197*, 370–378.
(38) Robinson, K.; Gibbs, G. V.; Ribbe, P. H. Quadratic Elongation: A Quantitative Measure of Distortion in Coordination Polyhedra. *Science* **1971**, *172*, 567–570.
(39) Tsunekawa, S.; Sivamohan, R.; Ito, S.; Kasuya, A.; Fukuda, T. Structural Study on Monosize CeO_{2-X} Nano-Particles. *Nanostructured Mater.* **1999**, *11* (1), 141–147.
(40) Tsunekawa, S.; Ito, S.; Mori, T.; Ishikawa, K.; Li, Z.-Q.; Kawazoe, Y. Critical Size and Anomalous Lattice Expansion in Nanocrystalline $BaTiO_3$ Particles. *Phys. Rev. B* **2000**, *62* (5), 3065–3070.
(41) Akdogan, E. K.; Rawn, C. J.; Porter, W. D.; Payzant, E. a.; Safari, A. Size Effects in $PbTiO_3$ Nanocrystals: Effect of Particle Size on Spontaneous Polarization and Strains. *J. Appl. Phys.* **2005**, *97* (8), 84305.
(42) Swamy, V.; Menzies, D.; Muddle, B. C.; Kuznetsov, A.; Dubrovinsky, L. S.; Dai, Q.; Dmitriev, V. Nonlinear Size Dependence of Anatase TiO_2 Lattice Parameters. *Appl. Phys. Lett.* **2006**, *88* (24), 243103.
(43) Shim, S.-H.; Duffy, T. S. Raman Spectroscopy of Fe_2O_3 to 62 GPa. *Am. Mineral.* **2001**, *87*, 318–326.
(44) Spanier, J. E.; Robinson, R. D.; Zhang, F.; Chan, S.-W.; Herman, I. P. Size-Dependent Properties of CeO_{2-Y} Nanoparticles as Studied by Raman Scattering. *Phys. Rev. B* **2001**, *64* (24), 245407.
(45) Weber, S.-U.; Gesing, T. M.; Röder, J.; Litterst, F. J.; Fischer, R. X.; Becker, K.-D. Temperature-Dependent ^{57}Fe Mössbauer Spectroscopy and Local Structure of Mullite-Type $Bi_2(Fe_xAl_{1-x})_4O_9$ ($0.1<x<1$) Solid Solutions. *Int. J. Mater. Res.* **2012**, *103*, 430–437.
(46) Kirsch, A.; Murshed, M. M.; Gaczynski, P.; Becker, K.-D.; Gesing, T. M. $Bi_2Fe_4O_9$: Structural Changes from Nano- to Micro-Crystalline State. *Zeitschrift für Naturforsch. B J. Chem. Sci.* **2016**, *71* (5), 447–455.
(47) Papaefthymiou, G. C.; Viescas, A. J.; Le Breton, J. M.; Chiron, H.; Juraszek, J.; Park, T. J.; Wong, S. S. Magnetic and Mössbauer Characterization of the Magnetic Properties of Single-Crystalline Sub-Micron Sized $Bi_2Fe_4O_9$ cubes. *Curr. Appl. Phys.* **2015**, *15* (3), 417–422.
(48) Burns, R. G. Mineral Mössbauer Spectroscopy: Correlations between Chemical Shift and Quadrupole Splitting Parameters. *Hyperfine Interact.* **1994**, *91*, 739–745.
(49) Hu, Z.-T.; Chen, B.; Lim, T.-T. Single-Crystalline $Bi_2Fe_4O_9$ Synthesized by Low-

Temperature Co-Precipitation: Performance as Photo- and Fenton Catalysts. *RSC Adv.* **2014**, *4* (53), 27820–27829.
(50) Wu, T.; Liu, L.; Pi, M.; Zhang, D.; Chen, S. Enhanced Magnetic and Photocatalytic Properties of $Bi_2Fe_4O_9$ Semiconductor with Large Exposed (001) Surface. *Appl. Surf. Sci.* **2016**, *377*, 253–261.
(51) Tauc, J.; Grigorovici, R.; Vancu, A. Optical Properties and Electronic Structure of Amorphous Germanium. *Phys. Status Solidi* **1966**, *15*, 627–637.
(52) Gao, K.; Zhu, J.; Gu, X.; Xie, Q.; Zhang, F.; Wu, X. Synthesis and Properties of $Bi_2Fe_4O_9$ with $FeCl_2 \cdot 6H_2O$ Addition. *J. Am. Ceram. Soc.* **2015**, *98* (4), 1128–1132.
(53) Curti, M.; Kirsch, A.; Granone, L. I.; Tarasi, F.; López Robledo, G.; Bahnemann, D. W.; Murshed, M. M.; Gesing, T. M.; Mendive, C. B. Visible-Light Photocatalysis with Mullite-Type $Bi_2(Al_{1-x}Fe_x)_4O_9$: Striking the Balance between Bandgap Narrowing and Conduction Band Lowering. *ACS Catal.* **2018,** *submitted for publication*.
(54) Voll, D.; Beran, A.; Schneider, H. Variation of Infrared Absorption Spectra in the System $Bi_2Al_{4-x}Fe_xO_9$ (X = 0–4), Structurally Related to Mullite. *Phys. Chem. Miner.* **2006**, *33* (8–9), 623–628.
(55) Gesing, T. M.; Fischer, R. X.; Burianek, M.; Mühlberg, M.; Debnath, T.; Rüscher, C. H.; Ottinger, J.; Buhl, J.-C.; Schneider, H. Synthesis and Properties of Mullite-Type $(Bi_{1-x}Sr_x)_2(M1_{1-y}M2_y)4O_{9-x}$ (M=Al, Ga, Fe). *J. Eur. Ceram. Soc.* **2011**, *31* (16), 3055–3062.
(56) Murshed, M. M.; Mendive, C. B.; Curti, M.; Šehović, M.; Friedrich, A.; Fischer, M.; Gesing, T. M. Thermal Expansion of Mullite-Type $Bi_2Al_4O_9$: A Study by X-Ray Diffraction, Vibrational Spectroscopy and Density Functional Theory. *J. Solid State Chem.* **2015**, *229*, 87–96.
(57) Han, J.-T.; Huang, Y.-H.; Wu, X.-J.; Wu, C.-L.; Wei, W.; Peng, B.; Huang, W.; Goodenough, J. B. Tunable Synthesis of Bismuth Ferrites with Various Morphologies. *Adv. Mater.* **2006**, *18* (16), 2145–2148.
(58) Williams, H. W.; Chamberland, B. L. Determination of Curie, Neel, or Crystallographic Transition Temperatures via Differential Scanning Calorimetry. *Anal. Chem.* **1969**, *41* (14), 2084–2086.

Supporting information

Structural, spectroscopic and thermoanalytic studies on $Bi_2Fe_4O_9$: tunable properties driven by nano- and poly-crystalline states.

Andrea Kirsch[a,b], M. Mangir Murshed[a,b*], F. Jochen Litterst[c], Thorsten M. Gesing[a,b]

[a] University of Bremen, Institute of Inorganic Chemistry and Crystallography, Leobener Straße 7, D-28359 Bremen, Germany

[b] University of Bremen, MAPEX center for materials and processes, Bibliothekstraße 1, D-28359 Bremen Germany

[c] Technische Universität Braunschweig, Institute for Condensed Matter Physics, Mendelssohnstr. 3, D-38106 Braunschweig, Germany

∗Corresponding author Tel.: +49 (0)421 218 63144, fax: +49 421 218 63145; e-mail: murshed@uni-bremen.de

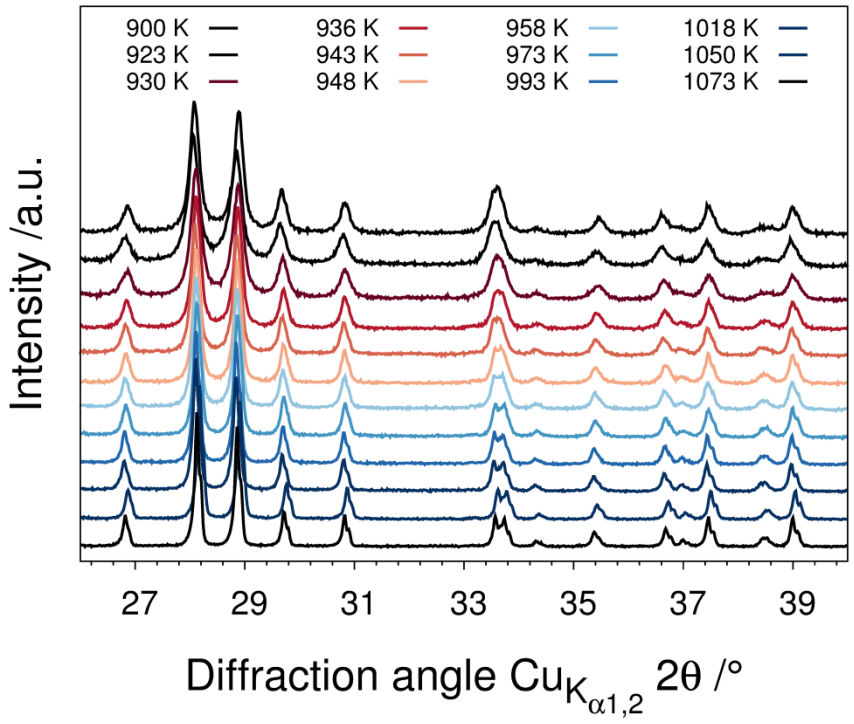

Figure S1. XRD patterns of the $Bi_2Fe_4O_9$ samples with varying average crystallite sizes (ACS) obtained at ambient conditions. Each sample was calcined at the temperatures from 900 – 1073 K for 2 h.

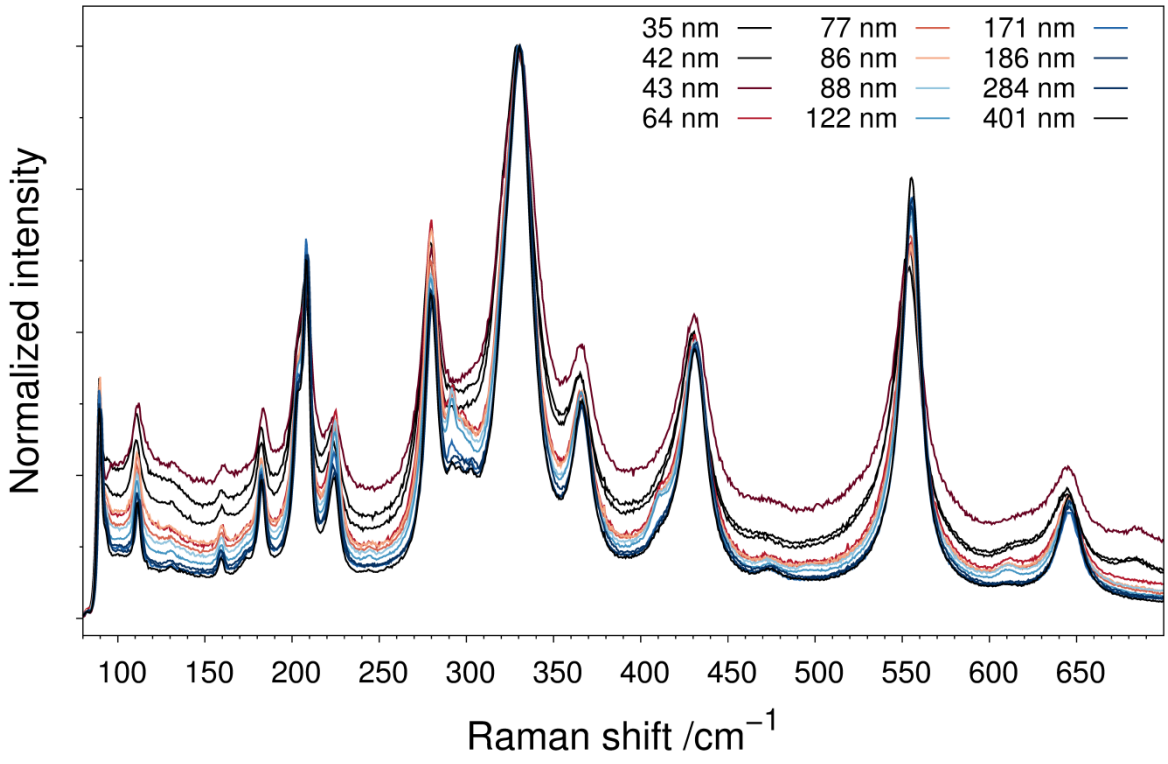

Figure S2. Normalized Raman spectra, recorded at ambient conditions, of $Bi_2Fe_4O_9$ samples with different average crystallite sizes.

Table S1. Raman frequencies (cm^{-1}) and assignment of the phonon modes of $Bi_2Fe_4O_9$ for a single crystal (SC)[21], 400 nm and 35 nm ACSs using the notation of Iliev et al.[21]

Mode	Atomic motions[21]	Calc[21]	Exp[21](SC)	400 nm	35 nm	$\Delta\omega/\omega^*$ /%
B_{1g}	Bi (y)	121	110	111.2(1)	110.8(1)	0.37
B_{3g}	O4 (z) + Fe2 (xy)	122	182	182.3(1)	182.2(1)	0.09
B_{1g}	Fe1 (xy) + O2 (xy)	237	202	203.0(1)	203.2(1)	-0.07
A_g	Fe1 (xy plane)	252	207	208.3(1)	208.1(1)	0.09
A_g	O2 (xy) + O3 (y)	297	222	223.9(2)	224.0(1)	0.01
B_{1g}	O3 (y)	326	283	279.6(2)	279.0(1)	0.23
A_g	O3 (xy)	395	331	329.66(4)	329.00(5)	0.20
A_g	O4 (z) + O3 (xy)	430	365	366.40(2)	365.64(5)	0.21
A_g	O3 (xy) + Fe2 (xy)	497	430	430.90(5)	429.53(7)	0.32
A_g	-	517	552	554.99(3)	552.88(7)	0.34
A_g	O4 (xy)	595	647	645.81(2)	643.89(7)	0.30

*The mode softening is quantified in the nanosized sample (35 nm) compared to the bulk material (400 nm) as $\Delta\omega/\omega = (\omega_{400nm} - \omega_{35nm})/\omega_{400nm}$ as described by Chen et al.[36] Calculated and experimental data from Iliev et al.[21] are also shown for comparison. Standard deviations are given in the parentheses.

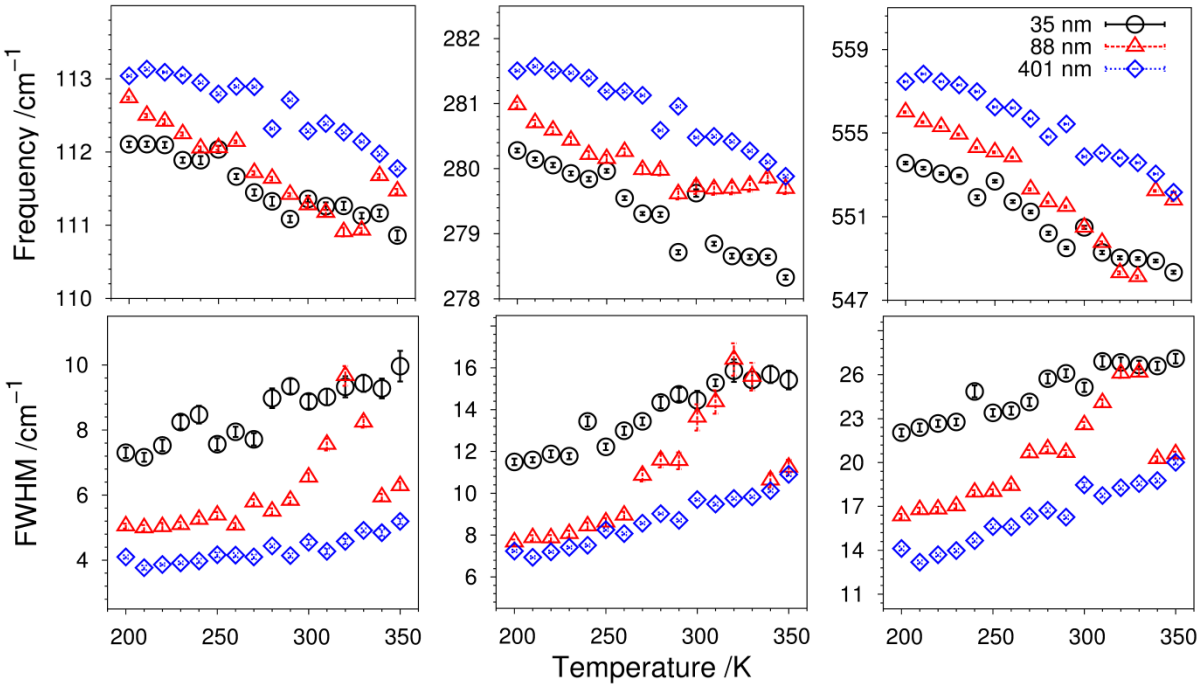

Figure S3. Temperature-dependent band positions and corresponding FWHM of a lower (110 cm^{-1}), middle (280 cm^{-1}) and high frequency (552 cm^{-1}) of the samples with average crystallite sizes of 35.3(4) nm, 88(1) nm and 401(17) nm.

Table S2. Hyperfine fitting parameters of the ^{57}Fe Mössbauer spectra of $Bi_2Fe_4O_9$ with average crystallite sizes (ACS) between 35.3(4) nm and 401(17) nm. IS: isomer shifts vs. α-Fe at 300 K. QS: quadrupole splitting. A: relative spectral area. Γ: absorber linewidth. B_{hf}: magnetic hyperfine field. Indices Tet and Oct stand for tetrahedral and octahedral.

300 K										
ACS /nm	IS_T /mm s^{-1}	QS_T /mm s^{-1}	A_T /%	Γ_T /mm s^{-1}	B_{hf} (Tet)	IS_O /mm s^{-1}	QS_O [#] /mm s^{-1}	A_O /%	Γ_O /mm s^{-1}	B_{hf} (Oct)
35.3(4)	0.231(2)	0.957(2)	50(1)	0.168(2)	-	0.353(2)	0.408(2)	50(1)	0.170(2)	-
42.1(4)	0.233(2)	0.956(2)	50(1)	0.170(2)	-	0.354(2)	0.401(2)	50(1)	0.170(2)	-
43.1(5)	0.235(2)	0.964(2)	51(1)	0.178(2)	-	0.355(2)	0.405(2)	49(1)	0.159(2)	-
64.4(8)	0.235(2)	0.959(2)	45(1)	0.170(2)	-	0.354(2)	0.390(2)	46(1)	0.172(2)	-
77(1)	0.231(2)	0.958(2)	51(1)	0.173(2)	-	0.352(2)	0.388(2)	49(1)	0.171(2)	-
86(1)	0.233(2)	0.955(2)	50(1)	0.161(2)	-	0.355(2)	0.386(2)	50(1)	0.162(2)	-
88(1)	0.233(2)	0.958(2)	49(1)	0.159(2)	-	0.356(2)	0.381(2)	51(1)	0.164(2)	-
122(2)	0.230(2)	0.949(2)	50(1)	0.154(2)	-	0.355(2)	0.380(2)	50(1)	0.155(2)	-
171(3)	0.232(2)	0.942(2)	51(1)	0.142(2)	-	0.352(2)	0.369(2)	49(1)	0.139(2)	-
186(4)	0.232(2)	0.950(2)	50(1)	0.150(2)	-	0.355(2)	0.378(2)	50(1)	0.150(2)	-
284(9)	0.231(2)	0.948(2)	50(1)	0.134(2)	-	0.356(2)	0.378(2)	50(1)	0.136(2)	-
401(17)	0.231(2)	0.953(2)	50(1)	0.140(2)	-	0.352(2)	0.375(2)	50(1)	0.143(2)	-
20 K										
ACS /nm	IS_T /mm s^{-1}	θ_T [#] /°	A_T /%	Γ_T /mm s^{-1}	B_{hf} (Tet)	IS_O /mm s^{-1}	θ_O [#] /°	A_O /%	Γ_O /mm s^{-1}	B_{hf} (Oct)
35.3(4)	0.340(2)	55(1)	51(1)	0.299(2)	46.52(4)	0.456(2)	39(1)	49(1)	0.358(2)	50.55(4)
77(1)	0.325(2)	54(1)	50(1)	0.254(2)	46.47(4)	0.453(2)	37(1)	50(1)	0.293(2)	50.45(4)
88(1)	0.320(2)	53(1)	50(1)	0.252(2)	46.72(4)	0.461(2)	37(1)	50(1)	0.270(2)	50.79(4)
122(2)	0.320(2)	52(1)	49(1)	0.230(2)	46.68(4)	0.446(2)	35(1)	51(1)	0.214	50.71(4)
171(3)	0.322(2)	52(1)	50(1)	0.197(2)	46.77(4)	0.453(2)	34(1)	50(1)	0.185(2)	50.81(4)
284(9)	0.310(2)	52(1)	49(1)	0.228(2)	46.74(4)	0.448(2)	35(1)	51(1)	0.224(2)	50.78(4)
401(17)	0.323(2)	52(1)	50(1)	0.188(2)	46.72(4)	0.452(2)	35(1)	50(1)	0.189(2)	50.75(4)

[#]Angle between hyperfine magnetic field (Bhf) and the main component of the electric field gradient (Vzz) with fixed QS at 300 K. Estimated standard deviations are given in the parentheses.

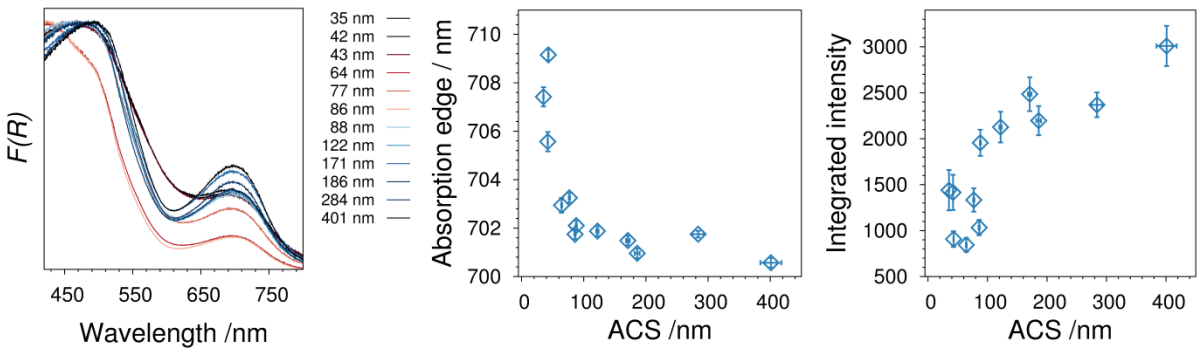

Figure S4. *Left panel*: Kubelka - Munk transformed diffuse UV/vis spectra of $Bi_2Fe_4O_9$ with average crystallite sizes (ACSs) from 35.3(4) - 401(17) nm. *Middle panel*: ACS-dependent maxima of the 2nd absorption feature. *Right panel*: ACS-dependent intensity of the 2nd absorption feature.

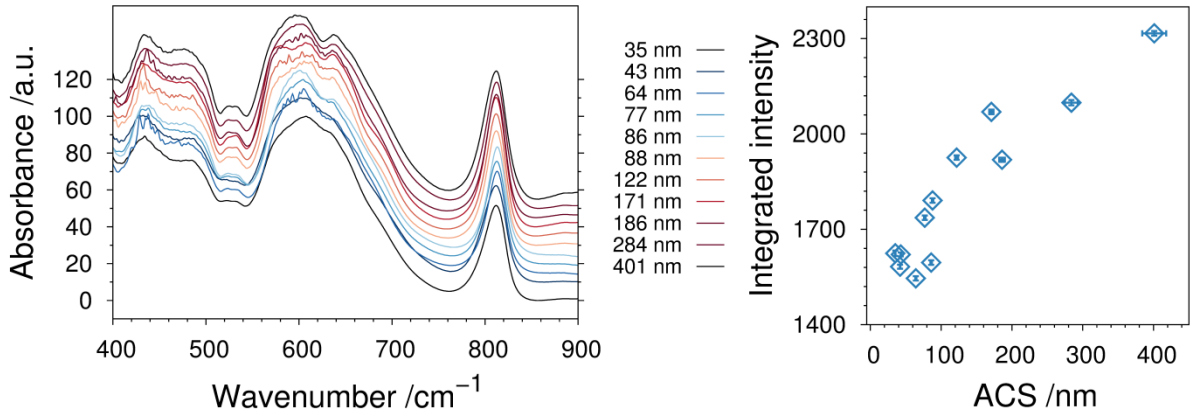

Figure S5. Fourier transform infrared spectra of the $Bi_2Fe_4O_9$ samples with average crystallite sizes (ACSs) from 35.3(4) – 401(17) nm.

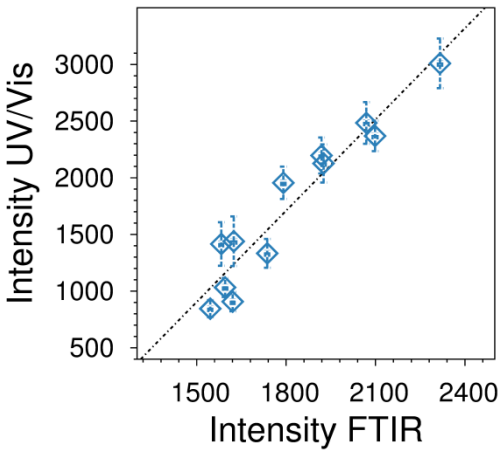

Figure S6. Correlation between the intensity of the 2nd absorption hump in the UV-Vis spectra and the intensity of the Fe-O stretching vibration of the FeO_4 tetrahedra at ~812 cm^{-1} in the FTIR spectra of $Bi_2Fe_4O_9$.

Concluding discussion

Within the scope of this dissertation the $Bi_2O_3 – Fe_2O_3$ phase system has been extensively studied. Two very promising compounds, the perovskite-type $(Bi_{1-x}Fe_x)FeO_3$ and the mullite-type $Bi_2Fe_4O_9$, are crystallizing in this system with prominent physical properties such as multiferroic[1], superparamagnetic[2], magnetic[3] and electrical properties[4]. In this thesis, a special focus was placed on the structural transformation of a precursor material into the $Bi_2Fe_4O_9$ structure and the synthesis parameters that influence this complex and in this regard sensitive system. An overview of the tunability of the synthesis conditions and the resulting materials is given in chapter 2.[5] It could be shown that both methods, the polyol process and sol-gel procedure using PVAs, provide a huge opportunity to control the resulting phase composition and their kinetics, structures and corresponding properties of the samples produced. The $Bi_2Fe_4O_9$ precursor's particle size, morphology, structural composition and crystallinity could be varied in many ways by conducting small changes during the synthesis procedure. The type of complexing agent, for instance, has a huge influence on the structural composition of the precursors and therefore on the crystallization kinetics and pathways during their transformation into the $Bi_2Fe_4O_9$ structure. Using sorbitol as a complexing agent the pH value of the synthesis solution has a huge influence even on the phase ratio of perovskite-type $BiFeO_3$ to mullite-type $Bi_2Fe_4O_9$ in calcined samples. Furthermore, it was found that $Bi_2Fe_4O_9$ preferentially crystallizes in an acidic medium, whereas the perovskite-type clearly prefers an alkaline medium.

During the studies of the synthesis and calcination conditions it was found that the perovskite-type and mullite-type structure always crystallize side by side in a given temperature range of about ~680 - 920 K (chapter 2, 3 ,5 and 6).[6-8] In order to get a deeper insight into the involved phase transformations a precursor material of $Bi_2Fe_4O_9$ composition was synthesized by a polyol method (chapter 3).[6] It was studied by SEM, XRD, ^{57}Fe Mössbauer and FTIR spectroscopy. In addition, the precursor material was heated and fully converted into the mullite-type $Bi_2Fe_4O_9$ structure. During the heating experiments, the structural changes and phase transformations were monitored by *in-situ* heating XRD and ^{57}Fe Mössbauer spectroscopy, respectively. The results lead to the conclusion that the precursor material possessed a disordered $(Bi_{1-x}Fe_x)FeO_3$ perovskite structure that gradually approached the features of the $Bi_2Fe_4O_9$ mullite-type.[6] Furthermore, the Fe^{3+} content

on the A-site of the perovskite-type structure was found to depend on the heating temperature.[6] This study unambiguously showed that the structure of nano-materials is not necessarily identical to the respective micro-crystalline ones although exhibiting the same chemical composition.[6] Since the Fe^{3+} content on the A-site of the perovskite-type structure (ABO_3) was found to change during the gradual transformation into the $Bi_2Fe_4O_9$ structure, it was possible to synthesize two new compounds - namely $(Bi_{0.75}Fe_{0.25})FeO_3$ and $(Bi_{0.85}Fe_{0.15})FeO_3$ (chapter 4).[2] They were produced by calcination of a precursor material at 873 K for 10 and 30 minutes, respectively, and characterized by several techniques such as *in-house* and synchrotron XRD, temperature-dependent time-of-flight neutron powder diffraction, SQUID measurements, ^{57}Fe Mössbauer and Raman spectroscopy.[2] The SQUID analysis as well as the ^{57}Fe Mössbauer spectra revealed that both, $(Bi_{0.75}Fe_{0.25})FeO_3$ and $(Bi_{0.85}Fe_{0.15})FeO_3$, possess superparamagnetic behaviour in contrast to unsubstituted $BiFeO_3$ showing antiferromagnetic behaviour.[2] By considering all the results it can be stated that the partial replacement of the Bi-site by Fe^{3+} significantly changes the crystal-physico-chemical properties such as the thermal expansion, polyhedral distortion, Debye temperature, vibrational and magnetic properties.[2] Besides the chemical modification of crystal structures it can also be interesting to conduct composition development of bulk multi-phase materials since such a materials performance can show enhanced physical properties[9,10] compared to the individual single phases. Thus, by heating a precursor material for two hours at different temperatures from 573 K to 1023 K it was possible to produce nanocomposites of the $BiFeO_3 - Bi_2Fe_4O_9$ binary system (chapter 5).[7] The composition-structure-property relationships were studied and correlations between structural parameters, such as the degree of crystallinity and phase ratio of $BiFeO_3$: $Bi_2Fe_4O_9$ and physical properties, such as the materials morphology, band gap and vibrational properties were observed and discussed.[7] The nature of optical transitions in the $Bi_2Fe_4O_9$ phase were found to be of direct nature, what was an on-going topic of debates in prior studies.[7] Furthermore, the study suggested that the combination of the recently proposed derivative absorption spectrum fitting (DASF) method[11] and the frequently used Tauc's method is a suitable tool to concomitantly determine the band gap and the nature of transition (direct and indirect) of a semiconducting material.[7] A further approach to tune a materials performance is to decrease the system into the nano-size regime as nanostructures can be

fundamentally different from their corresponding microstructures. This phenomenon is attributed to a greater surface-to-volume ratio and confinement effects caused by the finite size of the given system. Within this dissertation, it was demonstrated that it is possible to prepare mullite-type $Bi_2Fe_4O_9$ structures with discrete average crystallite sizes ($L_{Vol}(IB)$) from 35.3(4) nm to 401(17) nm by heating a precursor material for two hours at different temperatures (chapter 6).[8] Systematic investigations were performed in order to map the correlation of the size and other structural features such as the metric parameters of the unit cell and the distortion of local coordinations and physical properties such as the color, band gaps, morphology, vibrational and magnetic properties.[8] Nanoscale materials often show a critical size from what on they change their physical properties showing a clear size-dependence. For mullite-type $Bi_2Fe_4O_9$ this critical size was found to be ~122(2) nm.[8] In conclusion, nano-materials can not merely be regarded as miniaturized versions of their corresponding bulk materials since they can possess unusual forms of structural disorder[12] and even show different structures[6] and size-dependent properties[8] although they have a similar chemical composition. It is clear that multiferroic materials -such as $(Bi_{1-x}Fe_x)FeO_3$ and $Bi_2Fe_4O_9$- and their composites are of fundamental interest and possess auspicious crystal, chemical and physical properties. Due to their multifunctionality in external electric and magnetic fields magnetic semiconductors are promising for the development of a broad range of a completely new generation of advanced materials such as spin-based electronics and spin valves.[13] There is a clear opportunity to tune a systems performance by changing its chemical and/or phase composition and/or dimensionality. However, the concomitant control of a materials crystal structure, surface chemistry, degree of crystallinity, monodispersity, size, shape as well as chemical and phase composition is not trivial and seems to remain a challenging issue of nanostructure synthesis.

References

(1) Zhao, T.; Scholl, A.; Zavaliche, F.; Lee, K.; Barry, M.; Doran, A.; Cruz, M. P.; Chu, Y. H.; Ederer, C.; Spaldin, N. A.; et al. Electrical Control of Antiferromagnetic Domains in Multiferroic $BiFeO_3$ Films at Room Temperature. *Nat. Mater.* **2006**, *5* (10), 823–829.

(2) Kirsch, A.; Murshed, M. M.; Kirkham, M. J.; Huq, A.; Litterst, F. J.; Gesing, T. M. Temperature-Dependent Structural and Spectroscopic Studies of $(Bi_{1-x}Fe_x)FeO_3$. *J. Phys. Chem. C* **2018**, *submitted for publication*.

(3) Zhang, Q.; Gong, W.; Wang, J.; Ning, X.; Wang, Z.; Zhao, X.; Ren, W.; Zhang, Z. Size-Dependent Magnetic, Photoabsorbing, and Photocatalytic Properties of Single-Crystalline $Bi_2Fe_4O_9$ Semiconductor Nanocrystals. *J. Phys. Chem. C* **2011**, *115*, 25241–25246.
(4) Li, Y.; Zhang, Y.; Ye, W.; Yu, J.; Lu, C.; Xia, L. Photo-to-Current Response of $Bi_2Fe_4O_9$ Nanocrystals Synthesized through a Chemical Co-Precipitation Process. *New J. Chem.* **2012**, *36* (6), 1297–1300.
(5) Kirsch, A.; Murshed, M. M.; Gesing, T. M. Facile Sol-Gel Synthesis of $Bi_2Fe_4O_9$ and Nanocomposites of the (1-x) $BiFeO_3$ · (x) $Bi_2Fe_4O_9$ system, *manuscript in preparation*.
(6) Kirsch, A.; Murshed, M. M.; Gaczynski, P.; Becker, K.-D.; Gesing, T. M. $Bi_2Fe_4O_9$: Structural Changes from Nano- to Micro-Crystalline State. *Zeitschrift für Naturforsch. B J. Chem. Sci.* **2016**, *71* (5), 447–455.
(7) Kirsch, A.; Murshed, M. M.; Schowalter, M.; Rosenauer, A.; Gesing, T. M. Nanoparticle Precursor into Polycrystalline $Bi_2Fe_4O_9$: An Evolutionary Investigation of Structural, Morphological, Optical, and Vibrational Properties. *J. Phys. Chem. C* **2016**, *120* (33), 18831–18840.
(8) Kirsch, A.; Murshed, M. M.; Litterst, F. J.; Gesing, T. M. Structural, spectroscopic and thermoanalytic studies on $Bi_2Fe_4O_9$: tunable properties driven by nano- and poly-crystalline states *J. Phys. Chem. C* **2018***, submitted for publication.*
(9) Bakardjieva, S.; Šubrt, J.; Štengl, V.; Dianez, M. J.; Sayagues, M. J. Photoactivity of Anatase–rutile TiO_2 Nanocrystalline Mixtures Obtained by Heat Treatment of Homogeneously Precipitated Anatase. *Appl. Catal. B Environ.* **2005**, *58* (3–4), 193–202.
(10) Maity, T.; Goswami, S.; Bhattacharya, D.; Roy, S. Superspin Glass Mediated Giant Spontaneous Exchange Bias in a Nanocomposite of $BiFeO_3$-$Bi_2Fe_4O_9$. *Phys. Rev. Lett.* **2013**, *110* (10), 107201.
(11) Souri, D.; Tahan, Z. E. A New Method for the Determination of Optical Band Gap and the Nature of Optical Transitions in Semiconductors. *Appl. Phys. B* **2015**, *119* (2), 273–279.
(12) Gilbert, B.; Huang, F.; Zhang, H.; Waychunas, G. A.; Banfield, J. F. Nanoparticles: Strained and Stiff. *Science* **2004**, *305* (5684), 651–654.
(13) Matsukura, F.; Ohno, H. III–V-Based Ferromagnetic Semiconductors. In *Nanomagnetism and Spintronics*; Elsevier, 2014; pp 277–315.

Recommendations for future study

It is empirically known that many factors play an important role in the synthesis of nanostructured materials, however systematic studies on the correlations of individual synthesis variables influencing the overall crystallization behaviour are rare. Especially such systems like $BiFeO_3$ - $Bi_2Fe_4O_9$, in which complex magnetic spin arrangements (spiral ordering and geometric frustration) compete with several other order parameters, provide an excellent opportunity to finetune the materials properties to a high degree by small changes in the synthesis procedure. In this regard, especially thermodynamically metastable materials and nanocomposites can be of huge interest for the design of a new generation of technological devices as highlighted recently by Sun et al. (2016).[1] A further degree of freedom to control the properties of the materials is the introducing of new elements, such as Al, Mn or rare earth elements. The huge divergence of physical properties, for instance the phase composition, optical properties and photocatalytic activity, in the system $Bi_2(Al_{1-x}Fe_x)_4O_9$ using similar synthesis and calcination conditions could be shown in a recent study.[2] Furthermore, it would be very interesting to conduct studies on the multiferroic properties of the solid solution $(Bi_{1-x}Fe_x)FeO_3$ and the (1-x) $BiFeO_3$ (x) $Bi_2Fe_4O_9$ nanocomposites. On the one hand, $(Bi_{1-x}Fe_x)FeO_3$ could show an interesting coupling between the superparamagnetic and ferroelectric properties. On the other hand, earlier studies already showed that a nanocomposite of 94% $BiFeO_3$ – 6% $Bi_2Fe_4O_9$ composition possessed an enormous spontaneous exchange bias between the ferromagnetic core of $Bi_2Fe_4O_9$ and the canted antiferromagnetic structure of $BiFeO_3$.[3] In this regard, also the incorporation of other ions could be interesting.

In conclusion, the study of metastable materials and nanocomposites is very attractive and could pave the way for new advanced applications and new areas in nanoscience research.[1] Future works in this direction should be carried out on an interdisciplinary basis by teams of physicists, chemists, material scientists and engineers in order to develop new perspectives and approaches dealing with such a complex field of research.

References

(1) Sun, W.; Dacek, S. T.; Ong, S. P.; Hautier, G.; Jain, A.; Richards, W. D.; Gamst, A. C.; Persson, K. A.; Ceder, G. The Thermodynamic Scale of Inorganic Crystalline Metastability. *Sci. Adv.* **2016**, *2* (11), e1600225-1–8.

(2) Curti, M.; Kirsch, A.; Granone, L. I.; Tarasi, F.; López Robledo, G.; Bahnemann, D. W.; Murshed, M. M.; Gesing, T. M.; Mendive, C. B. Visible-Light Photocatalysis with Mullite-Type $Bi_2(Al_{1-x}Fe_x)_4O_9$: Striking the Balance between Bandgap Narrowing and Conduction Band Lowering. *ACS Catal.* **2018***, 8,* 8844−8855.

(3) Maity, T.; Goswami, S.; Bhattacharya, D.; Roy, S. Superspin Glass Mediated Giant Spontaneous Exchange Bias in a Nanocomposite of $BiFeO_3$-$Bi_2Fe_4O_9$. *Phys. Rev. Lett.* **2013**, *110* (10), 107201.